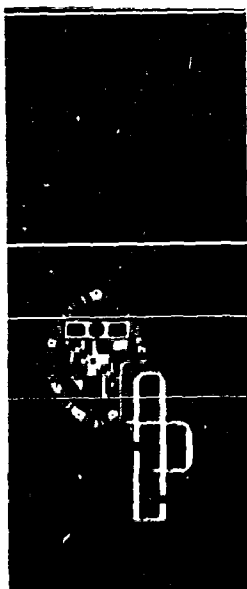


TG-882

MARCH 1967

Copy No.

AD 656888



Technical Memorandum

PHASED ARRAY ANTENNA DEVELOPMENT

by J. FRANK

DDC
RECEIVED
AUG 28 1967
C

THE JOHNS HOPKINS UNIVERSITY • APPLIED PHYSICS LABORATORY

Distribution of this document is unlimited.

Reproduced by the
CLEARINGHOUSE
for Federal Scientific & Technical
Information Springfield Va. 22151

TG-882

MARCH 1967

Technical Memorandum

PHASED ARRAY ANTENNA DEVELOPMENT

by J. FRANK

THE JOHNS HOPKINS UNIVERSITY • APPLIED PHYSICS LABORATORY
8621 Georgia Avenue, Silver Spring, Maryland 20910
Operating under Contract NOw 68-0604-c with the Department of the Navy

Distribution of this document is unlimited

**BLANK PAGES
IN THIS
DOCUMENT
WERE NOT
FILMED**

ABSTRACT

The ability to rapidly scan a highly directive antenna beam has been made possible by recent advances in the art of microwave phase shifting. This report describes an experimental C-band phased array antenna developed at the Applied Physics Laboratory. The antenna is composed of eight subarrays which may be arranged in several configurations to investigate the effects of a full array. Each subarray contains a reactive power divider, 48 ferrite phase shifters and their electronic drivers, and a radiating structure. The radiating structure has been designed to provide some compensation for impedance variation with scanning. The design and fabrication of the components are discussed in detail, and test results of the array are presented and analyzed.

FOREWORD

The phased array antenna program discussed in this report was sponsored by project DEFENDER, Advanced Research Projects Agency, Department of Defense. The work was an outgrowth of phased array studies and developments for the Navy under contract NOW 62-0604-c by the Antenna Development Project at APL under T. C. Cheston. Both the original development and the program reported here were carried out primarily by H. M. Grady, J. H. Kuck, and C. A. Shipley, as well as the author. Several sections of this report were prepared by the engineers directly responsible. In these cases, the author's name appears in the appropriate section. Helpful suggestions from the Array Radars Group of Lincoln Laboratories are gratefully acknowledged.

The report is divided into four sections: Section 1 provides a short introduction to the type of phased array developed and defines the objectives of the program. Section 2 details the design and fabrication of the eight subarrays and all of their components. Section 3 presents the results of measurements performed on three arrays, each of which was assembled from the eight subarrays. Finally, Section 4 summarizes the program and suggests future studies.

TABLE OF CONTENTS

List of Illustrations	ix
Section 1. INTRODUCTION	1
1.1 Description of Phased Array of Subarrays	1
1.2 Objectives	6
Section 2. PHASE I--DESIGN, CONSTRUCTION, AND MEASUREMENTS OF EIGHT SUBARRAYS	7
2.1 Summary of Phase I	7
2.2 Subarray	11
2.3 Power Divider	37
2.4 Phase Shifter	58
2.5 Driver Circuit	72
2.6 Wiring	82
Section 3. PHASE II--ARRAY PERFORMANCE	88
3.1 Summary of Phase II	88
3.2 Gain and Efficiency	92
3.3 VSWR	100
3.4 Beam Steering Accuracy	109
3.5 Patterns and Quantization Lobes	118

THE JOHNS HOPKINS UNIVERSITY
APPLIED PHYSICS LABORATORY
Silver Spring, Maryland

TABLE OF CONTENTS
(cont'd)

Section 4. CONCLUSIONS AND RECOMMENDATIONS	.	.	145
Appendix A. Subarray Bandwidth Considerations	.	.	147
Appendix B. Quantization Lobe Analysis	.	.	153
References	.	.	163

LIST OF ILLUSTRATIONS

<u>Figure</u>		<u>Page</u>
1-1	Phased Array Antenna	2
1-2	Prototype Subarray	3
1-3	1:48 Power Divider	4
1-4	1:12 Power Divider to Two Adjacent Columns of Elements	4
2-1	Assembly and Test Facility	7
2-2	Scanned Beams, E and H Planes	9
2-3	Completed 48-Element Subarray	11
2-4	Measured Gain for Eight Subarrays	14
2-5	Subarray Gain vs. Scan Angle	16
2-6	Correction Curve for Subarray VSWR Measure- ments	17
2-7	VSWR vs. Frequency for H Plane Scan	18
2-8	VSWR vs. Frequency for E Plane Scan	18
2-9	48-Element Subarray Boresight Pattern, H Plane	19
2-10	48-Element Subarray 60° Scan Pattern, H Plane	19
2-11	48-Element Subarray Boresight Pattern, E Plane	20
2-12	48-Element Subarray 60° Scan Pattern, E Plane	20
2-13	Plane Waves Propagating in Rectangular Waveguide	22

LIST OF ILLUSTRATIONS
(cont'd)

<u>Figure</u>		<u>Page</u>
2-14	Simulation of a Triangular Spaced Array	23
2-15	Array Simulator	24
2-16	VSWR Variation with Frequency, Boresight and 30° H Plane Scan	24
2-17	Subarray VSWR Variation with Scan	25
2-18	Element Symmetry around the Subarray Center	27
2-19	Diametric Opposite Phase Shifter Wiring	27
2-20	Anti-Symmetrically Phased Array	28
2-21	Phase Quantization with Bit Size of $22\frac{1}{2}^\circ$	31
2-22	Phase Quantization with Bit Size of $25\frac{1}{2}^\circ$	32
2-23	Phase Split Across Aperture at Boresight	34
2-24	E Plane Horn with Mounting Plate	34
2-25	Phase Shifter Wired in Place	36
2-26	Face Plate	36
2-27	1:4 H Plane Splitter and 1:12 E Plane Horn	38
2-28	Power Divider for Two Adjacent Columns of Elements	40
2-29	Instrumentation used for Testing 1:4 Power Splitters and 1:12 Horns	42
2-30	VSWR Variation with Frequency, 1:4 H Plane Power Divider	43
2-31	Amplitude Variation with Frequency, 1:4 H Plane Power Divider	43
2-32	VSWR of Lens Corrected Horn	44
2-33	Amplitude Variation across Lens Corrected E Plane Horn	45

LIST OF ILLUSTRATIONS
(cont'd)

<u>Figure</u>		<u>Page</u>
2-34	Amplitude Variation with Frequency, E Plane Horn and Lens	46
2-35	Phase Variation across Lens Corrected E Plane Horn	47
2-36	1:4 Power Splitter	48
2-37	1:12 E Plane Horn	49
2-38	Lens Curvature Design	51
2-39	Lens Matching	52
2-40	Waveguide Technique for Lens Matching	53
2-41	Mounting Plate	54
2-42	Test Fixture for Aperture Phase and Amplitude Measurements	56
2-43	Sliding Load	57
2-44	Ferrite Phase Shifter	59
2-45	Phase Shifter Construction Details	63
2-46	VSWR of Power Divider End of Phase Shifter	65
2-47	VSWR of Radiating End of Phase Shifter in Array Simulator	67
2-48	Differential Phase Variation with Temperature	69
2-49	Peak Power Handling Capacity of the Phase Shifter	69
2-50	Differential Phase Variation with Current	70
2-51	Phase Shifter Test Setup, Block Diagram	70
2-52	Driver Board Containing Four Drivers	73
2-53	Driver Box Housing Eight Driver Cards	73
2-54	Driver Circuit	76

LIST OF ILLUSTRATIONS
(cont'd)

<u>Figure</u>		<u>Page</u>
2-55	Current Waveform of Driver Pulses . . .	78
2-56	Internal Subarray Wiring . . .	84
2-57	External Subarray Wiring . . .	85
3-1	Antenna Measurements Facility . . .	88
3-2	Array Configurations . . .	90
3-3	Boresight Pattern Compared with Theoretical $(\frac{\sin x}{x})$ Envelope . . .	91
3-4	H Plane Gain Variation vs. Scan Angle . . .	97
3-5	E Plane Gain Variation vs. Scan Angle . . .	98
3-6	Gain Variation vs. Scan Angle, Tapered Amplitude Distribution . . .	98
3-7	Swept VSWR Comparison of Isolated and Immersed Subarray, Subarrays Aligned in H Plane . . .	103
3-8	Swept VSWR Comparison of Isolated and Immersed Subarray, Subarrays Aligned in E Plane . . .	103
3-9	Scanned VSWR Comparison of Immersed and Isolated Subarray, H Plane . . .	104
3-10	Scanned VSWR Comparison of Immersed and Isolated Subarray, E Plane . . .	105
3-11	Scanned VSWR Comparison of Immersed and Isolated Subarray, Circular Aperture . . .	106
3-12	VSWR Comparison of Tapered and Uniformly Illuminated Array . . .	108
3-13	Fine Steering and Array of Subarrays . . .	109
3-14	Subarray Pattern, Array Factor and Antenna Pattern . . .	110
3-15	Fine Steering within Subarray Pattern . . .	111
3-16	Quantized Approximation to $\sin \frac{2\pi x}{a}$. . .	114

LIST OF ILLUSTRATIONS
(cont'd)

<u>Figure</u>		<u>Page</u>
3-17	Absolute Beam Pointing Accuracy vs. Beam Scan Angle, H Plane	115
3-18	Absolute Beam Pointing Accuracy vs. Beam Scan Angle, E Plane	115
3-19	Frequency Steering of Array	116
3-20	Beam Pointing Error vs. Frequency H Plane	117
3-21	Boresight Pointing Error vs. Frequency, H Plane	117
3-22	Subarray Pattern and Array Factor	118
3-23	Quantization Lobe Caused by Displacement of Array Factor from Subarray Pattern	121
3-24	Peak Quantization Lobe, H Plane Scan	124
3-25	Peak Quantization Lobe, E Plane Scan	125
3-26	A Comparison of Two Roundoff Rules; 0° Beam, E Plane Pattern 5.65 Gc	127
3-27	A Comparison of Two Roundoff Rules; 60° Beam, E Plane Pattern, 5.65 Gc	128
3-28	Peak Quantization Lobe for Constant and Tapered Amplitude Distribution, H Plane Scan	130
3-29	Peak Quantization Lobe for Constant and Tapered Amplitude Distribution, E Plane Scan	130
3-30	1st Sidelobe Height vs. Scan Angle for Constant and Tapered Amplitude Distribution, H Plane	131
3-31	1st Sidelobe Height vs. Scan Angle for Constant and Tapered Amplitude Distribution, E Plane	131
3-32	0° Beam H Plane Patterns at 5.65 Gc	135
3-33	30° Beam H Plane Patterns at 5.65 Gc	136

LIST OF ILLUSTRATIONS
(cont'd)

<u>Figure</u>		<u>Page</u>
3-34	60° Beam H Plane Patterns at 5.65 Gc . . .	137
3-35	0° Beam E Plane Patterns at 5.65 Gc . . .	138
3-36	30° Beam E Plane Patterns at 5.65 Gc . . .	139
3-37	60° Beam E Plane Patterns at 5.65 Gc . . .	140
3-38	0°, 30°, and 60° Beam H Plane Patterns at 5.40 Gc	141
3-39	0°, 30°, and 60° Beam H Plane Patterns at 5.90 Gc	142
3-40	0°, 30°, and 60° Beam E Plane Patterns at 5.40 Gc	143
3-41	0°, 30°, and 60° Beam E Plane Patterns at 5.90 Gc	144

Section 1 INTRODUCTION

1.1 Description of Phased Array of Subarrays

During the past few years, advances in the art of microwave phase shifting have made phase steered antennas a practical method for rapidly scanning highly directive beams. Such antennas are suitable for modern multipurpose radars which may be required to search, track, and illuminate a multiplicity of targets.

One method of building a phase steered array is to use an array of subarrays. A standard subarray is first developed containing a multiplicity of radiating elements and by stacking subarrays, any size and shape of array may be approximated (Fig. 1-1). This technique may be used to advantage by employing the subarray as a plug-in unit. Advantage may also be taken of the wide instantaneous bandwidth properties of the subarray (typically 10%, dependent upon the size of the subarray as discussed in Appendix A) by using time delay networks to steer the individual subarrays. In addition, the ability to independently control the amplitude and phase of each subarray provides for independent shaping of the sum and difference patterns in both planes.

The essential ingredients of a phase steered array of subarrays are shown in Fig. 1-1. An RF signal provided at the Tx input is distributed to each subarray by the combining network. Each subarray may have a time delay network, providing a wide instantaneous bandwidth for fine steering of the array. After propagating through the time delay network, the signal is amplified to high power and fed to the individual phase shifters by the power dividing network. The final stages of power

dividing, phase shifting, and radiating are critical to the performance, cost, and weight of a phased array antenna system. These final stages are contained in the subarray, and the efforts of APL have been directed toward perfecting a subarray for use at C-band. These efforts were supported under Navy contract NOw 62-0604-c.

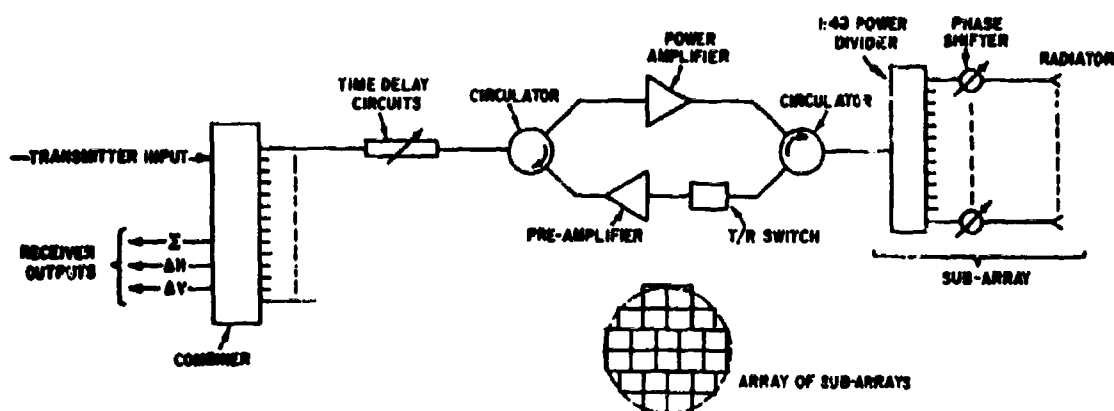


Fig. 1-1 Phased Array Antenna

A 48-element subarray had been developed at APL (Ref. 1) as a prototype and as such demonstrated the high efficiency and near theoretical performance expected. For its use as a practical light-weight antenna element capable of being repeatedly reproduced, modifications were necessary. Further, the performance of a subarray in the midst of an array of subarrays could not be determined by experiments on a single subarray. The program of building eight subarrays was conceived as a way of testing an array of subarrays in various configurations while obtaining a wealth of data on the cost, weight, and

repeatability of the various components produced on a small scale production basis. The program also afforded an opportunity to improve and simplify each of the individual components.

Such an array, designed to be used in several configurations, would prove to be a unique tool in the investigation of mutual coupling effects within a scanning array. With these considerations in mind, Project DEFENDER of ARPA requested APL to design, construct and test an array of eight subarrays using the APL subarray as a prototype. During the course of the design and construction phase of the program, all of the desired modifications were implemented.

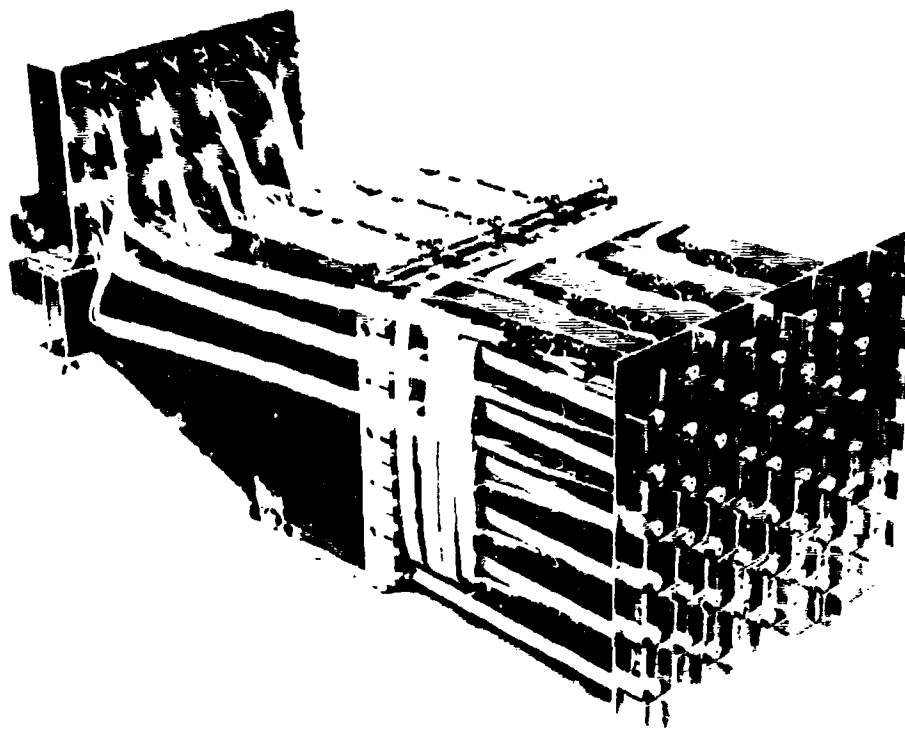


Fig. 1-2 Prototype Subarray

A prototype subarray which had originally been developed is shown in Fig. 1-2 and the power divider portion is shown in Fig. 1-3. Power is split four ways in the H plane to four E plane sectoral horns. This arrangement provides for an approximately constant power distribution across the aperture of a subarray. Each of the four sectoral horns is matched to 12 waveguide outputs arranged as shown in Fig. 1-4, to be aligned at the mouth of the horn and interlaced at the radiating aperture. The waveguides are 1.00 inch x 0.40 inch o.d. in size and each contains a four-bit latching ferrite phase shifter. The output end of the waveguide is designed to radiate into space in the presence of an array of radiators. The redesigned subarray utilizes the same principles.

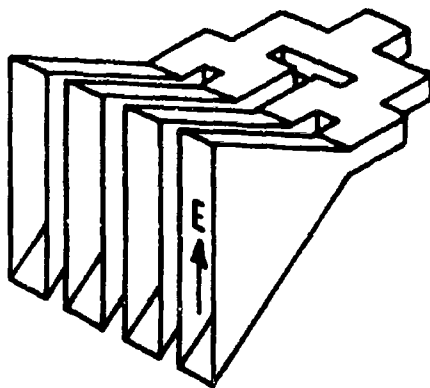


Fig. 1-3 1:48 Power Divider

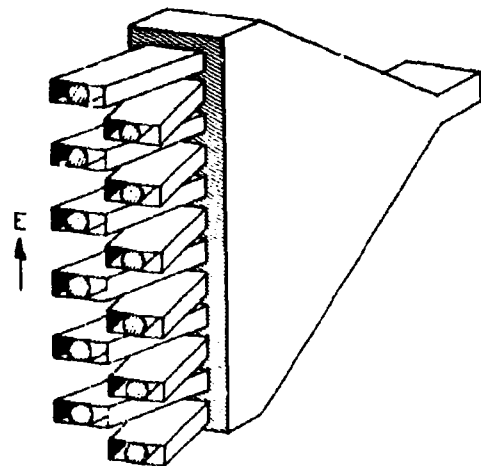


Fig. 1-4 1:12 Power Divider
to Two Adjacent Columns
of Elements

The prototype had been matched at 30° scan angle with the aid of waveguide simulators. However, there remained the problem of impedance variation with scan angle and the resultant mismatch. During the course of the program, some compensation for this variation was obtained by the use of a thin dielectric sheet placed a short distance in front of each of the radiating apertures.

1.2 Objectives

The primary objective of the program was to develop and evaluate an array of eight subarrays and, in so doing, determine the practical feasibility of a full sized array of subarrays as described in the introduction.

The program was divided into two phases:

Phase I Objectives

1. Develop, construct, and test eight subarrays and all of their associated components (e.g. power dividers, phase shifters, drivers, wiring, etc.).
2. Determine the reliability and repeatability of the various components when produced on a small scale production basis.
3. Provide insight to the cost and assembly time for a large array.
4. Evaluate the thin dielectric sheet as a means of reducing the mismatch of a scanning subarray.

Phase II Objectives

1. Evaluate the performance of an array of subarrays in various configurations and modes of operation.
2. Investigate the variation in mismatch with scanning for an immersed subarray (between other subarrays) as contrasted with an isolated subarray.
3. Determine the usefulness of a thin dielectric sheet in reducing reflections on scanning and determine whether the thin dielectric sheet produced any problems (e.g. lost beams caused by surface wave phenomenon).

Section 2

PHASE I--DESIGN, CONSTRUCTION, AND MEASUREMENTS OF EIGHT SUBARRAYS

2.1 Summary of Phase I

The program of designing and building eight phased array subarrays began on January 1, 1966, at which time orders for the major components were placed.

As previously mentioned, a considerable amount of redesign was required to improve the match, develop simple small-scale production techniques, and solve some of the problems of assembling an array of subarrays. In preparation for the fabrication and test of the components, several fixtures were designed and fabricated. An assembly room was prepared at the laboratory and several contract personnel were hired and trained for the type of work to be performed. A photograph of the assembly and testing facility is shown in Fig. 2-1.



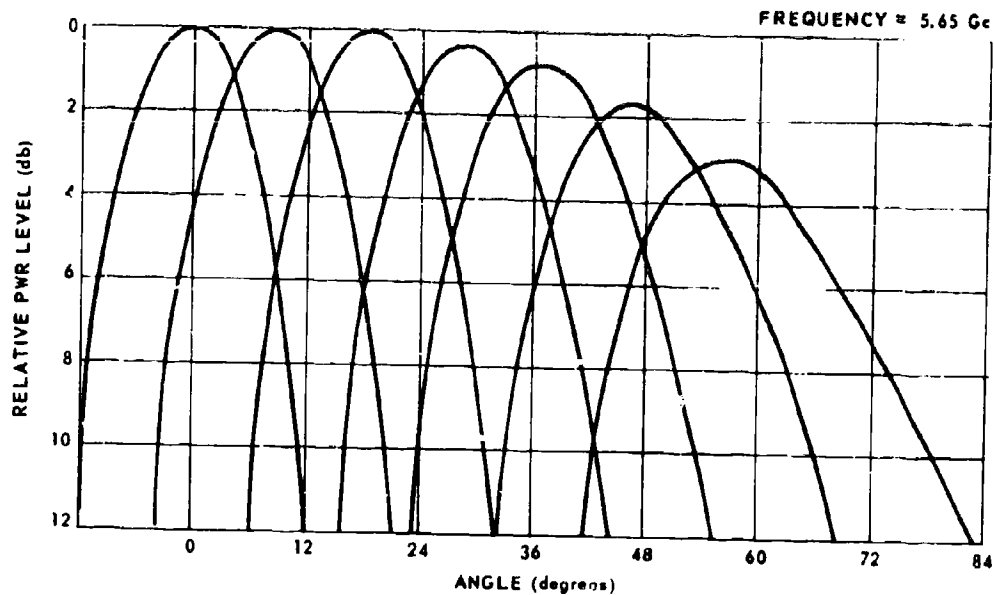
Fig. 2-1 Assembly and Test Facility

During the month of March, the required parts began to arrive and the personnel was increased to a maximum of nine. The construction and testing phase continued on schedule with very few difficulties being encountered. The first subarray was completed in mid-April and tested extensively. It was found to function properly and construction continued at the rate of approximately one subarray per week. By mid-June, all eight subarrays had been completed and tested. A ninth subarray was constructed from the spare parts.

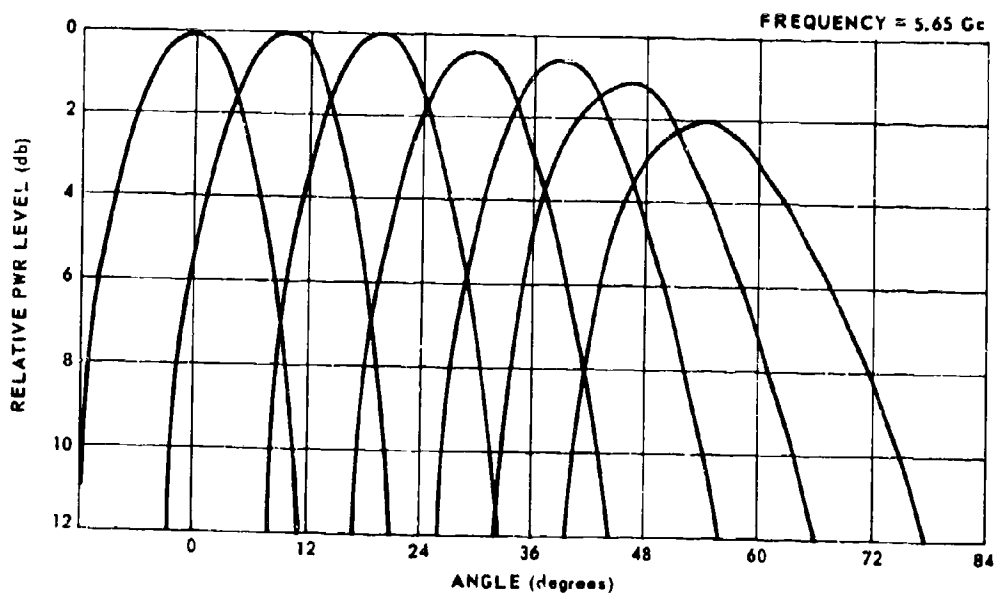
The total cost for the parts, assembly, and testing was \$140 per element. This figure includes the cost for the power dividers, phase shifters, drivers, wiring, and interconnecting cables. Not included are the costs of engineering development, supervision, and overhead. The weight per element was 3/4 lb, including the power divider, phase shifters, drivers, wiring, and connectors.

Tests were performed on each of the components and on the subarrays. The results of these tests are reported in detail in the following sections. A few of the more interesting results are summarized here:

1. The subarray gain was measured across the frequency band. When compared with $\frac{4\pi A}{\lambda^2}$, the gain measurements indicate an efficiency of better than 70% including the loss due to the phase shifters and the power divider.
2. Some compensation for the impedance variation when scanning was achieved by the use of a dielectric sheet in front of the aperture. The matching structure was determined experimentally with the aid of a waveguide simulator.
3. Scanned patterns demonstrated almost theoretical performance as seen in Fig. 2-2. The asymmetry of the patterns at large scan angles is a natural consequence of the $\cos \theta$ variation of the projected aperture.



(a) E PLANE SCAN, 0-60° IN 10° STEPS



(b) H PLANE SCAN, 0-60° IN 10° STEPS

Fig. 2-2 Scanned Beams, E and H Planes

4. The 10% band of optimum performance had been designed for 5.4 to 5.9 Gc. Best performance was actually achieved over the band from 5.45 to 5.95 Gc. The cause of this error has been traced to the E plane Horn, and may be corrected by increasing the width of the horn by 0.020 inch.
5. The maximum VSWR of a subarray at boresight, including the mismatch due to power divider, lens, phase shifters, and radiators, was less than 1.2 over a 10% band of frequencies. Best match was achieved at 30° scan in the H plane, corresponding to the scan angle at which the aperture had been matched using a waveguide simulator.
6. More than 400 phase shifters were assembled and tested, the results showing good, repeatable performance in all characteristics (e.g., VSWR, insertion loss, differential phase, intersection phase). Fewer than 6% of the phase shifters were rejected for reasons of high insertion loss or high VSWR.

2.2 Subarray

2.2.1 Introduction

The subarray is designed to be a wide band building block for a phased array antenna system, providing 1:48 power division (with approximately equal power and phase), 48 phase shifters, solid state drivers for the phase shifters, and a radiating aperture. A photograph of a completed subarray is shown in Fig. 2-3. As a unit, it may be easily replaced in a large array. The units were designed so that, electrically, no gaps would appear in the array, resulting in a continuous aperture of radiators. This is important since any periodicity across the array will tend to produce unwanted grating lobes. These grating lobes have been reduced to a minimum by using equal power distribution within a subarray and arranging the array of

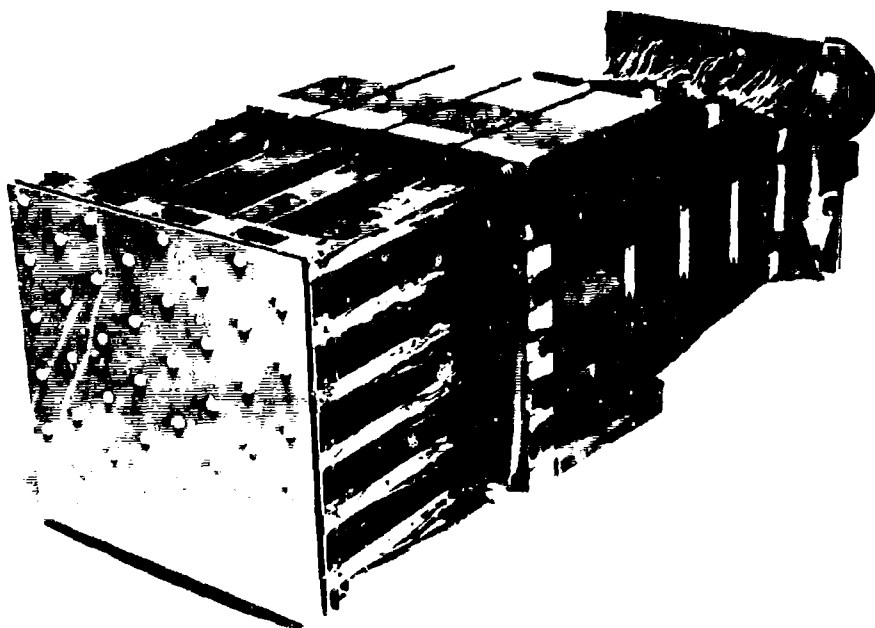


Fig. 2-3 Completed 48-Element Subarray

subarrays to appear as a continuous aperture of radiators (i.e., by observing the face of an array, it is not possible to determine where one subarray ends and another begins). For this program, an additional requirement was the capability to rearrange the subarrays in various configurations so that different planes of scan and operating conditions could be investigated.

As previously mentioned, one objective of the program was to attempt some compensation for the variation of mismatch on scanning. It should be noted that the subarray provides a ready means for the evaluation of this mismatch since all of the reflected power appears in phase at the input port. This is so because the round trip distance through the phase shifter is constant regardless of phase setting (a consequence of the nonreciprocal phase shift property). In addition the path length from the input to each of the phase shifters is the same. Consequently, all reflections stemming from aperture mismatch with scan are observed at the input port and are not misphased nor are they reradiated.

Since the subarray response determines the performance of the array, each subarray was tested extensively. The tests included gain and VSWR at boresight (swept measurements over the 10% band of interest) and swept VSWR measurements at 40° and 60° scan in both E and H planes. These 48 swept measurements showed consistent predictable results indicating that the subarrays were operating properly. After VSWR and gain measurements, more than 80 patterns were taken on the first two subarrays and 12 patterns on the remaining subarrays. Finally, VSWR was measured in the 45° plane of scan. The characteristics of a subarray are summarized in Table 2-1.

Table 2-1
Subarray Characteristics

Cost (materials and assembly)	\$6750
Weight	-35 lb
Dimensions:	
Cross section	7.5 in. x 8.0 in.
Length (without drivers)	24 5/8 in.
Length (with drivers)	35 5/8 in.
Measured Gain @ 5.65 Gc	21.4 db
Calculated Gain @ 5.65 Gc	22.4 db
Gain Variation (subarray to subarray)	± 0.2 db

VSWR

	Peak		Average of Peaks		Average	
	Measured	Corrected	Measured	Corrected	Measured	Corrected
Boresight	1.5	1.67	1.37	1.49	1.12	1.16
40° E Plane	1.58	1.78	1.51	1.68	1.28	1.36
40° H Plane	1.60	1.82	1.56	1.75	1.33	1.43
60° E Plane	1.8	2.1	1.76	2.06	1.36	1.47
60° H Plane	2.5	3.34	2.33	3.02	1.97	2.4

2.2.2 Subarray Results

Gain -- The measured boresight gain at f_0 (5.65 Gc) averaged over the eight subarrays is 21.4 db. This compared with a calculated value for $4\pi A/\lambda^2$ of 22.4 db. The 1 db of loss is attributed to 3/4 db in the phase shifter and 1/4 db in the power divider and aperture.

The maximum gain variation from subarray to subarray at f_0 is within ± 0.2 db. This order of gain variation from subarray to subarray is consistent over the frequency band as may be seen from Fig. 2-4, which shows the variation of gain with frequency.

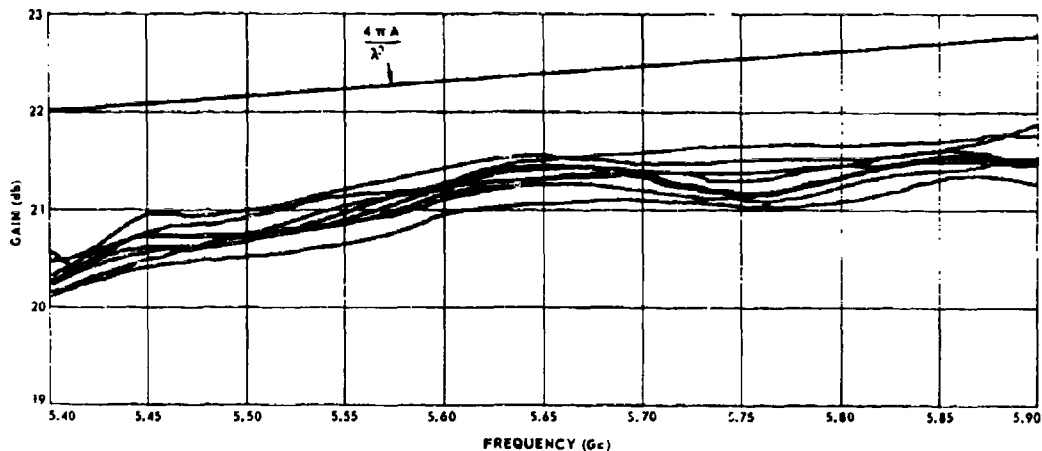


Fig. 2-4 Measured Gain for Eight Subarrays

The variation of gain with scan angle was measured in both the E and H planes. In presenting these data, the loss due to mismatch (VSWR) has been added to the measured gain, thereby simplifying the comparison between gain and projected area. The true gain may be determined by subtracting the loss due to mismatch. The data for E

and H plane scan are plotted in Fig. 2-5 where they are compared with $\cos \theta$ (projected aperture). It may be noted that in the H plane, the gain has not fallen off as rapidly as might be expected.

VSWR--Swept VSWR measurements were taken on all subarrays in both planes and at several scan angles. The results are tabulated in Table 2-1. It should be noted that the VSWR is measured through the loss of the power divider and the phase shifter. Therefore, a corrected VSWR has been computed and tabulated assuming that the VSWR is seen through a 1 db attenuator (i. e., the reflection coefficient is assumed to be 2 db higher than measured). Figure 2-6 presents the curve for converting the measured VSWR to corrected VSWR.

Referring to Table 2-1 again, the VSWR data are assembled to present three pertinent measures of VSWR. Peak VSWR is the largest VSWR measured considering all subarrays and all frequencies. "Average of peaks" VSWR is obtained by selecting the largest VSWR measured within the band for each of the eight subarrays and averaging over these eight values. Average VSWR is the average over the frequency band on one typical subarray.

Examination of the measured VSWR's of the eight subarrays reveals that the VSWR versus frequency characteristics of the eight subarrays are quite similar. Typical swept VSWR measurements for boresight and for scanned beams in both planes may be seen in Figs. 2-7 and 2-8.

Patterns--Numerous patterns were taken in both the E and H planes. These patterns indicated repeatable predictable subarray performance. An evaluation of the patterns may be obtained by comparing the calculated and measured patterns for boresight and 60° scan in both E and H planes. The calculations assumed a $\sqrt{\cos \theta}$ element

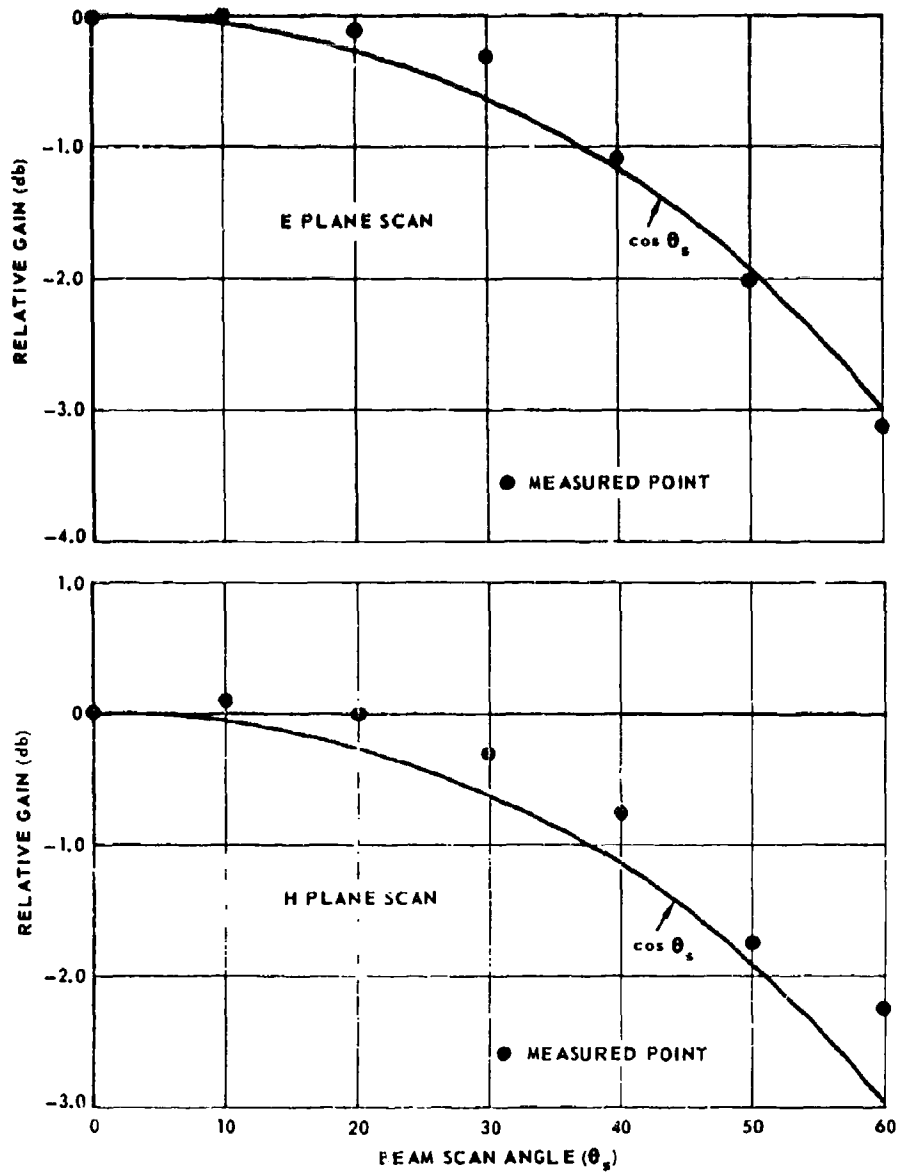


Fig. 2-5 Subarray Gain vs. Scan Angle

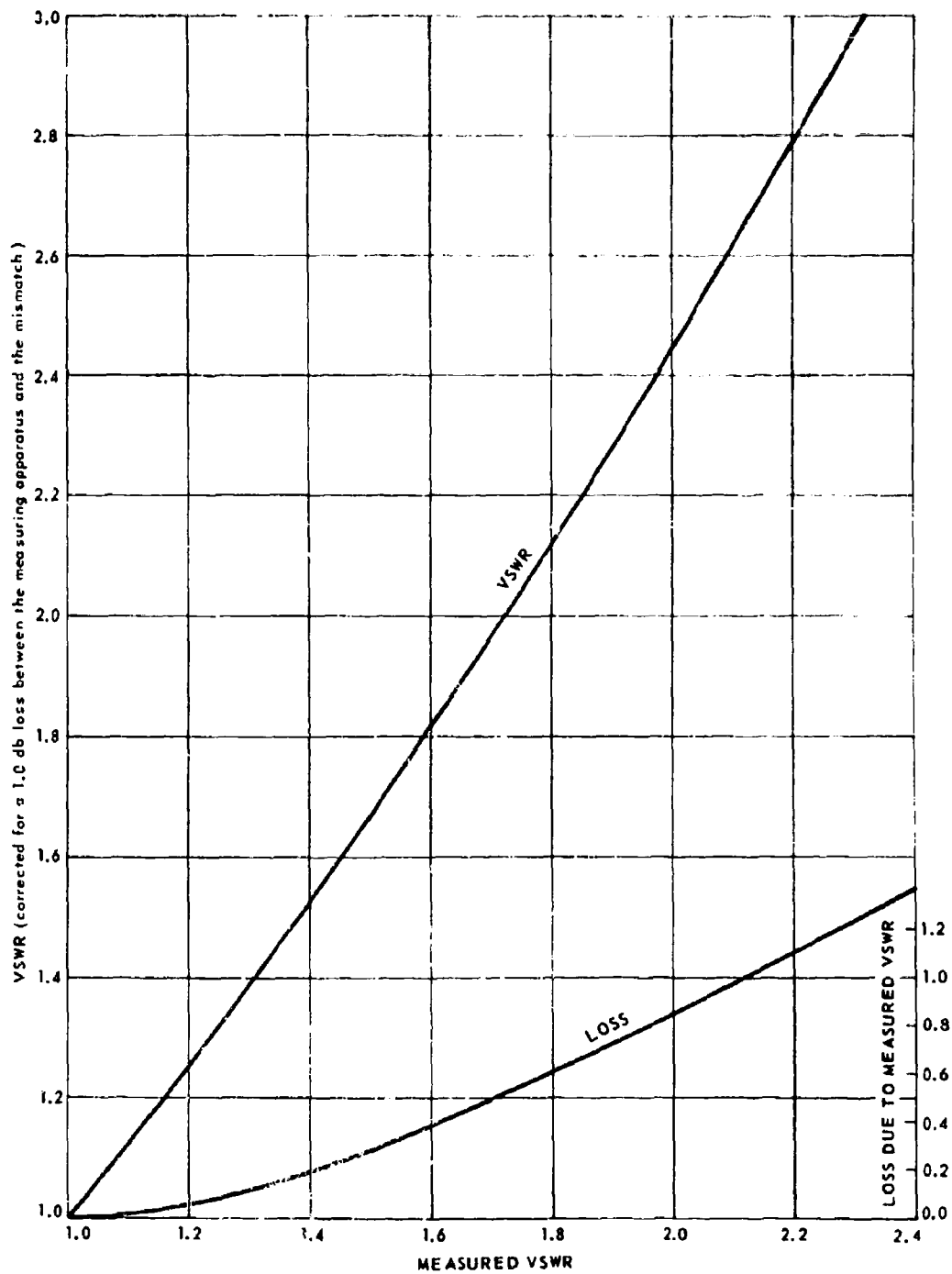


Fig. 2-6 Correction Curve for Subarray VSWR Measurements

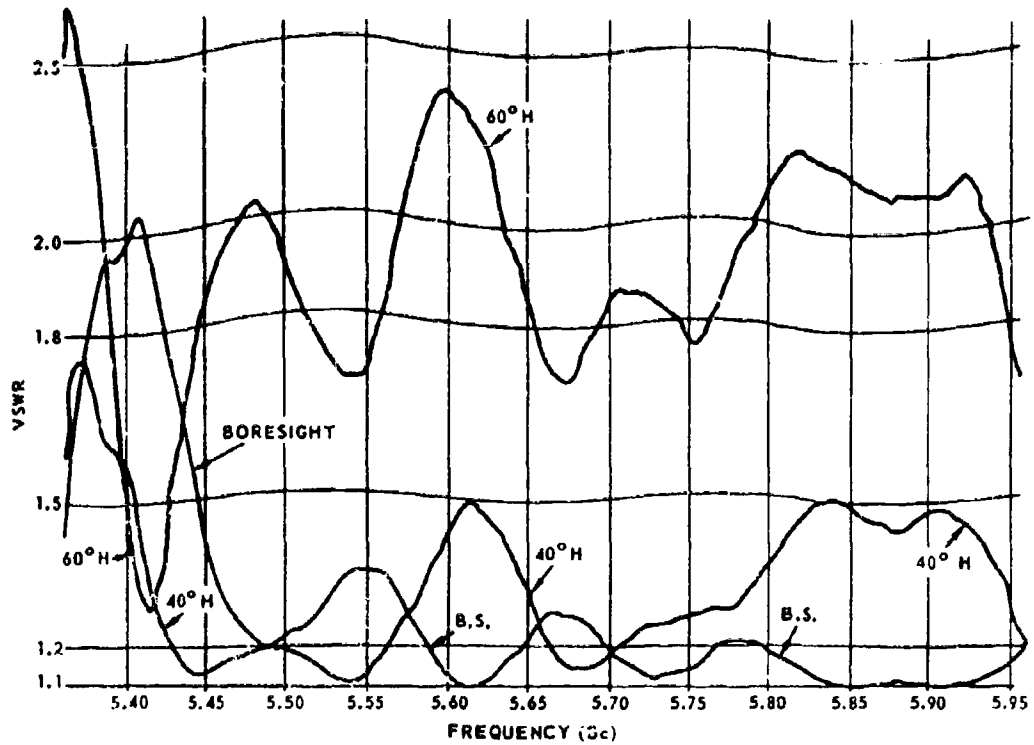


Fig. 2-7 VSWR vs. Frequency for H Plane Scan

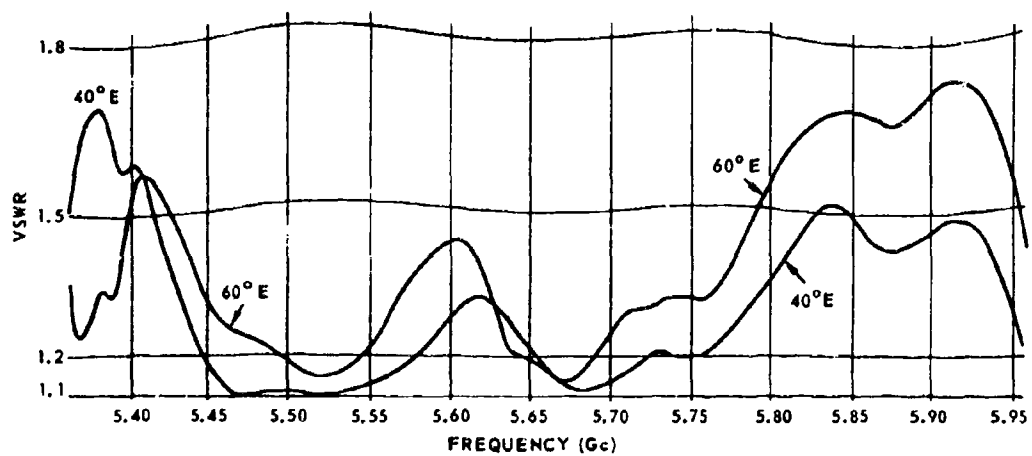


Fig. 2-8 VSWR vs. Frequency for E Plane Scan

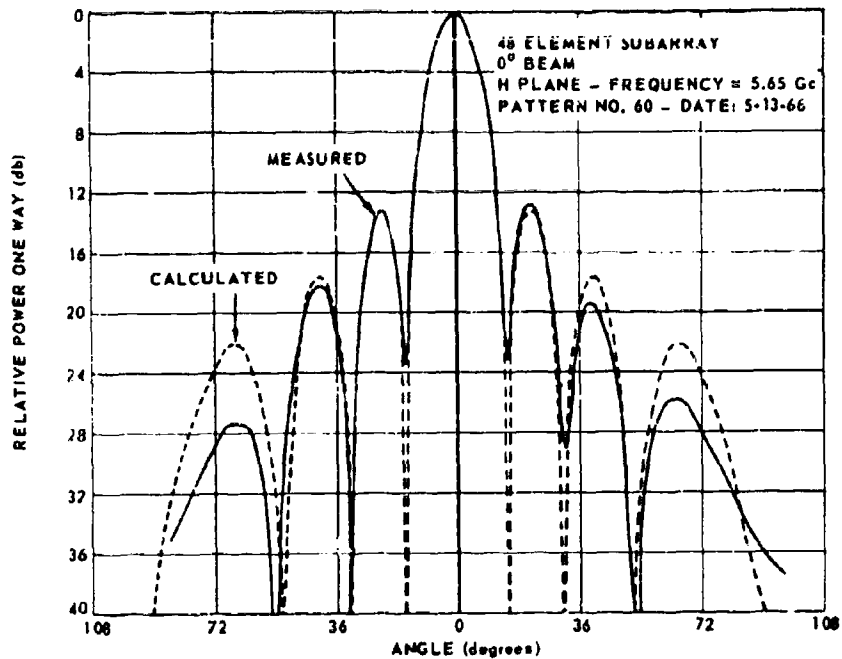


Fig. 2-9 48-Element Subarray Boresight Pattern, H Plane

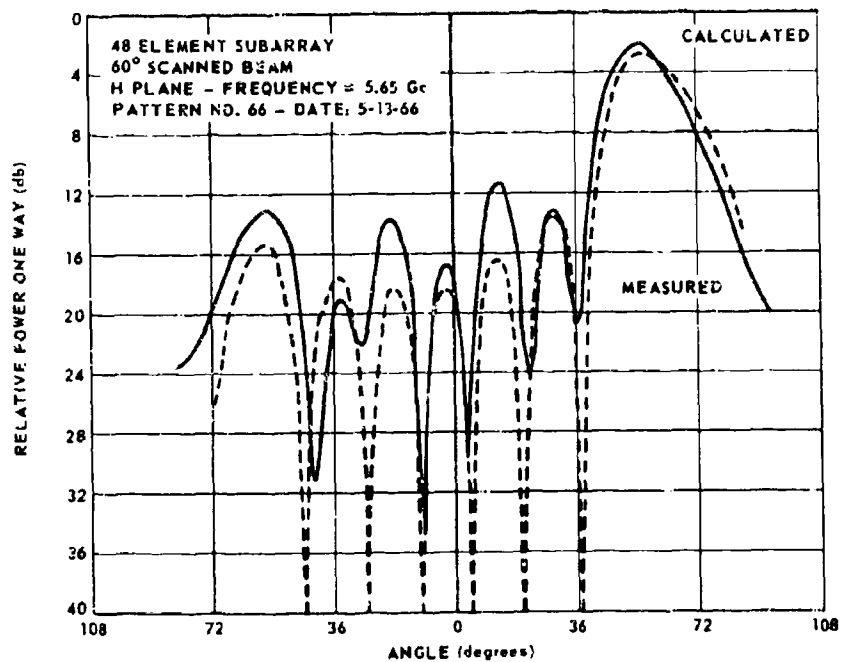


Fig. 2-10 48-Element Subarray 60° Scan Pattern, H Plane

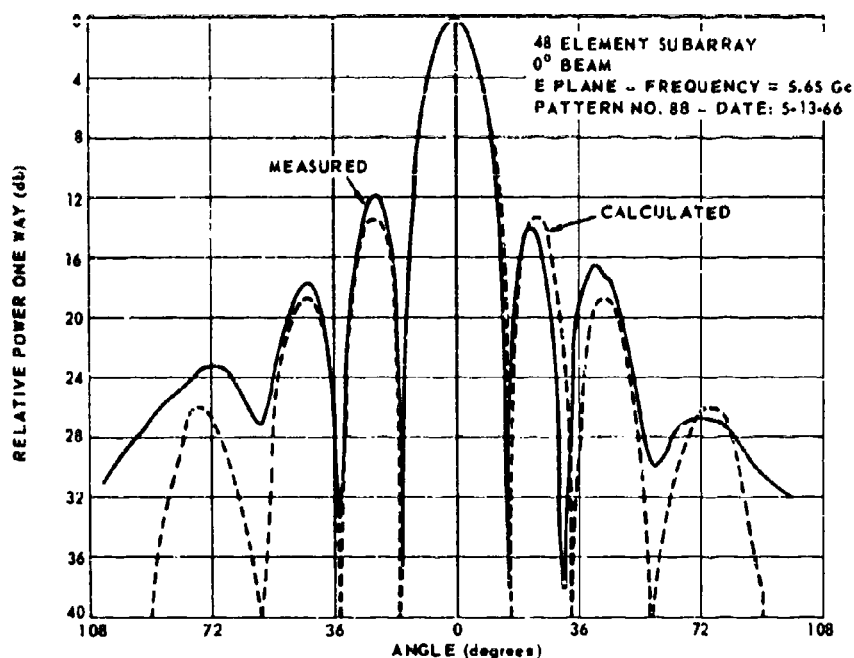


Fig. 2-11 48-Element Subarray Boresight Pattern, E Plane

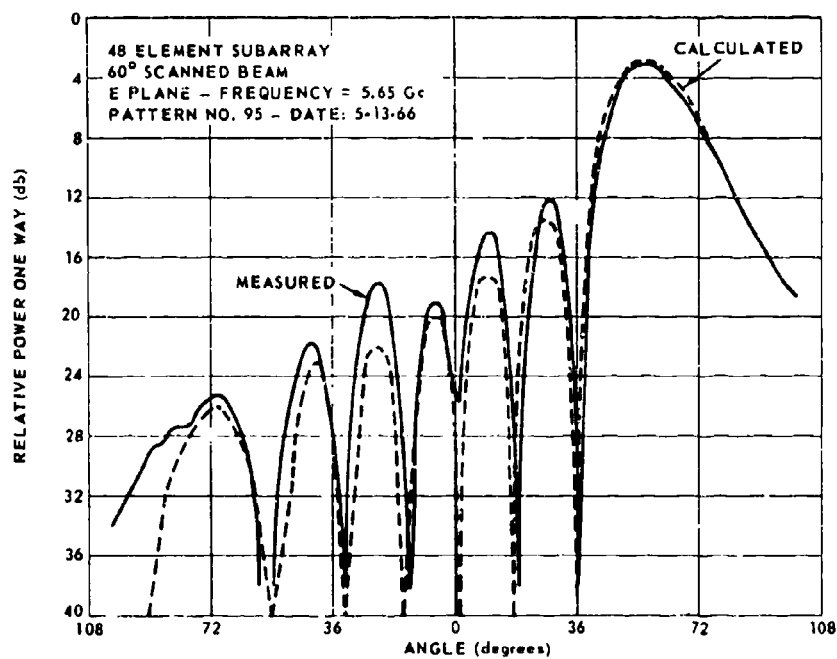


Fig. 2-12 48-Element Subarray 60° Scan Pattern, E Plane

radiation pattern. These patterns are plotted in Figs. 2-9 through 2-12. The agreement between the calculated and measured patterns are a measure of the overall tolerances.

Surface Wave Phenomenon--Some speculation had arisen over the use of dielectric matching plates, in that slow surface waves might propagate (Ref. 2), resulting in a lost beam for some combination of scan angle and frequency. It should be noted that this phenomenon was never observed during the swept VSWR and swept gain measurements performed at various scan angles in both planes of scan.

2.2.3 Aperture Matching

During the past few years, a good deal of effort has gone into matching a radiator in the presence of an array of radiators. The use of waveguide simulators as first proposed by Wheeler Labs (Ref. 3) has been a useful aid in empirically determining the matching structure. Summarizing, a waveguide operating in a TE_{10} mode may be considered to contain two inclined plane waves propagating down the waveguide. The angle which each of the plane waves makes with longitudinal direction (Fig. 2-13) is determined by the H dimension of the waveguide and simulates the angle of scan of an infinite array:

$$\sin \theta = \frac{\lambda}{\lambda_c}$$

θ = scan angle

λ = free space wavelength

λ_c = cutoff wavelength of the guide.

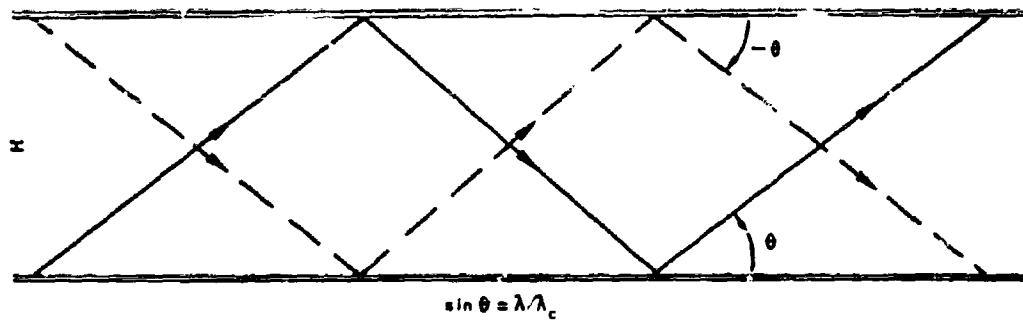


Fig. 2-13 Plane Waves Propagating in Rectangular Waveguide

Additional scan angles may be simulated by exciting other modes. The waveguide dimensions are chosen so that a radiating element placed in the waveguide sees mirror images in the walls of the waveguide that appear to be at the same spacing as the array to be simulated. Naturally, the waveguide simulates an infinite array, while the actual array is finite. However, the approximation is good for arrays of several wavelengths in each dimension.

For this program a waveguide simulator was designed at APL to simulate the triangular spacing being used. A diagram of the grid spacing with the simulator superimposed is shown in Fig. 2-14. Note that the corners of four elements are cut by the simulator. In practice, these elements have been omitted in the simulation since they represent cutoff elements. A photograph of the simulator is shown in Fig. 2-15.

The dimensions of the simulator determine the angle of scan which was 30° in the H plane for this case. A consequence of matching into a simulator representing 30° of scan is that the array (and the sub-arrays) are best matched at this angle. This has been borne out

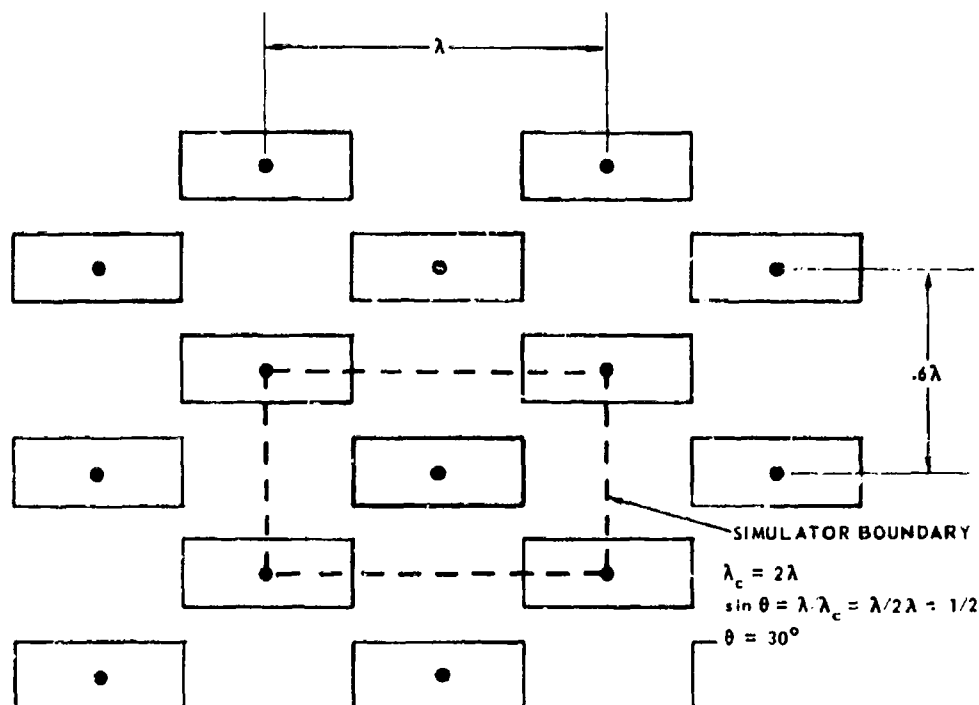


Fig. 2-14 Simulation of a Triangular Spaced Array

experimentally. Figure 2-16 shows the swept VSWR of a subarray scanned to 30° in the H plane as compared to the VSWR at boresight.

The variation of impedance with scanning constitutes one of the most interesting problems in phased array development. Wheeler Labs has suggested (Ref. 4) that a thin sheet of dielectric has reflection properties that are similar in amplitude but opposite in sign to that of a scanning array. A dielectric sheet of this sort could be used to compensate somewhat for a change of impedance with scan angle.

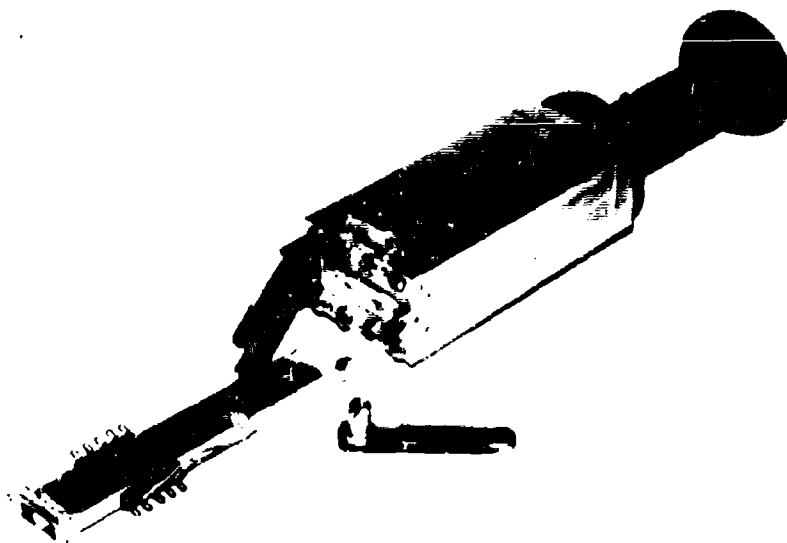


Fig. 2-15 Array Simulator

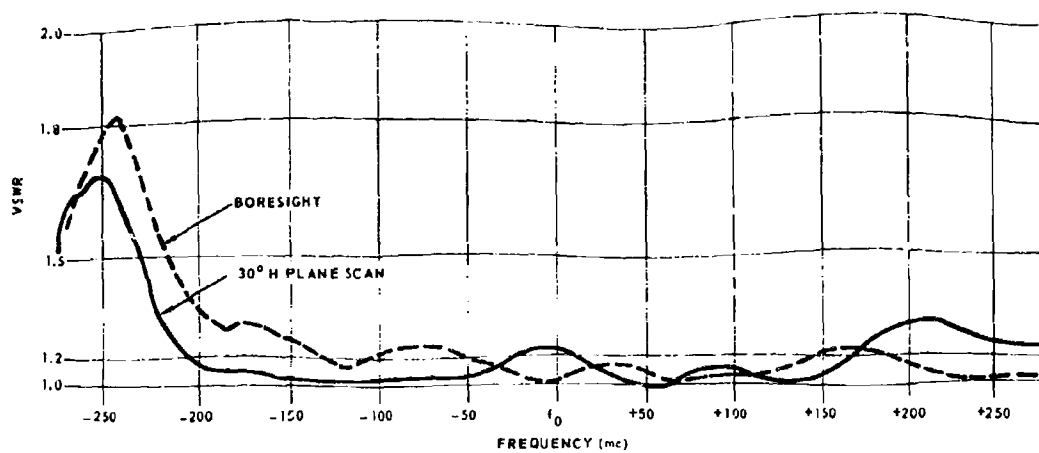


Fig. 2-16 VSWR Variation with Frequency Boresight and 30° H Plane Scan

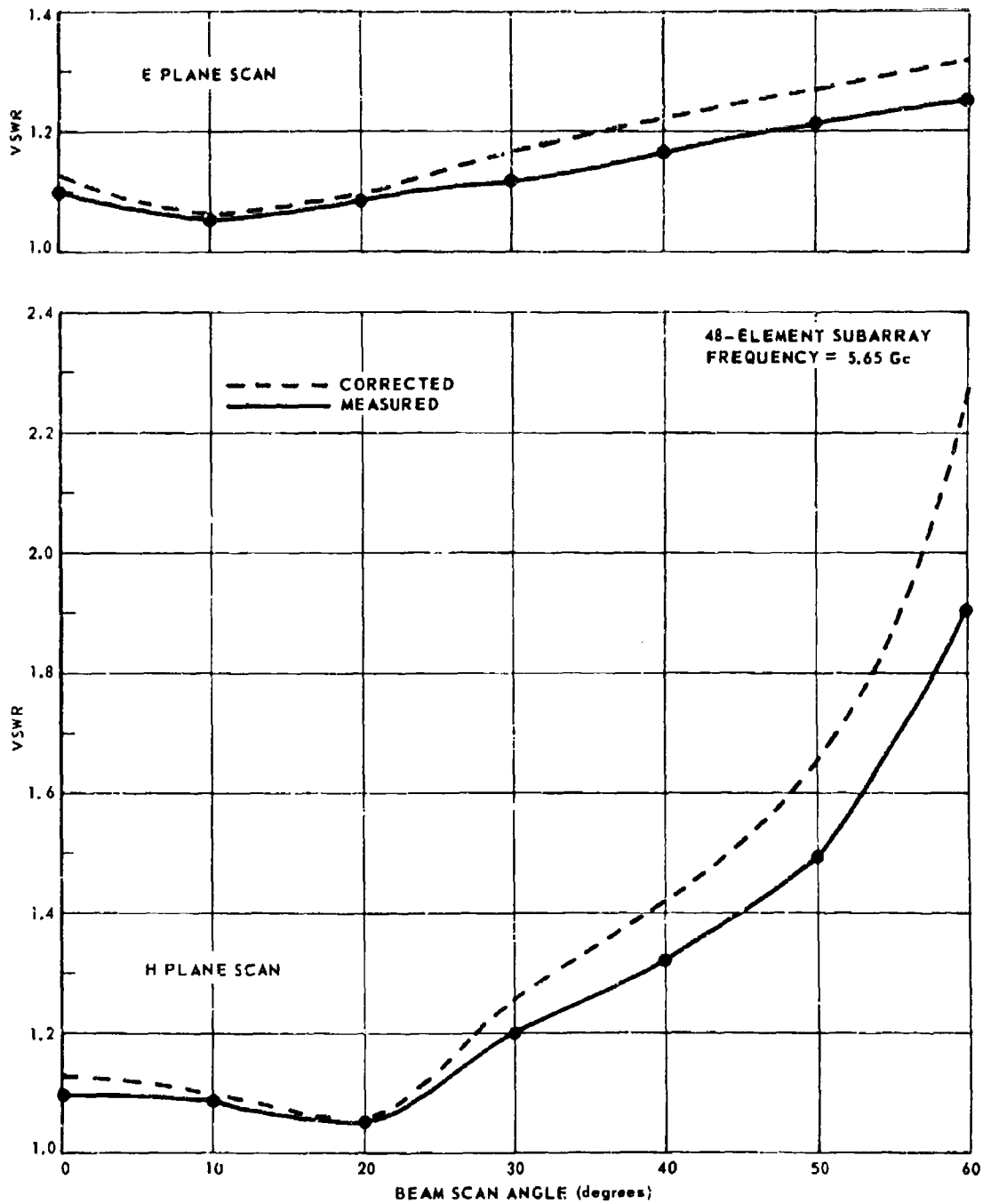


Fig. 2-17 Subarray VSWR Variation with Scan

During this program, such a dielectric sheet has been empirically designed, and does provide some compensation for scanning in both planes of scan. The residual mismatch produced by the dielectric sheet was matched out in the waveguide simulator. Measurements on a subarray (Fig. 2-17) show the resulting variation of VSWR with scan in both planes, using a thin dielectric sheet ($\epsilon = 9$) for compensation. The data presented have been corrected for an assumed 1 db loss between the subarray aperture and the measuring setup.

2.2.4 Beam Steering of a Subarray

In an effort to simplify the wiring, and reduce the computations required for steering, advantage has been taken of the symmetry of a subarray. It may be seen upon examination of Fig. 2-18 that radiators on diametrically opposite sides of the center of the subarray require phase commands of equal magnitude but opposite sign. By wiring the two phase shifters in series, but with the current traveling in opposite directions (Fig. 2-19), the two phase shifters may be controlled simultaneously. This technique does sacrifice some fineness in steering a subarray beam, but does not sacrifice any fineness in the steering of a full array. It does, however, influence the quantization lobe level of the full array. The topics of array steering and array quantization lobes are discussed in Sections 3.4 and 3.5.

In steering the subarray with diametric wiring and 4-bit phase shifters, the coarsest steering increments occur in the H plane. For this plan of scan, the beam is limited to scanning steps of $1/16$ of a beamwidth (0.9° in the vicinity of boresight). For scanning in the E plane, the beam will move in steps of $1/24$ of a beamwidth. Actually, the beam can move in much finer increments if one chooses to apply a

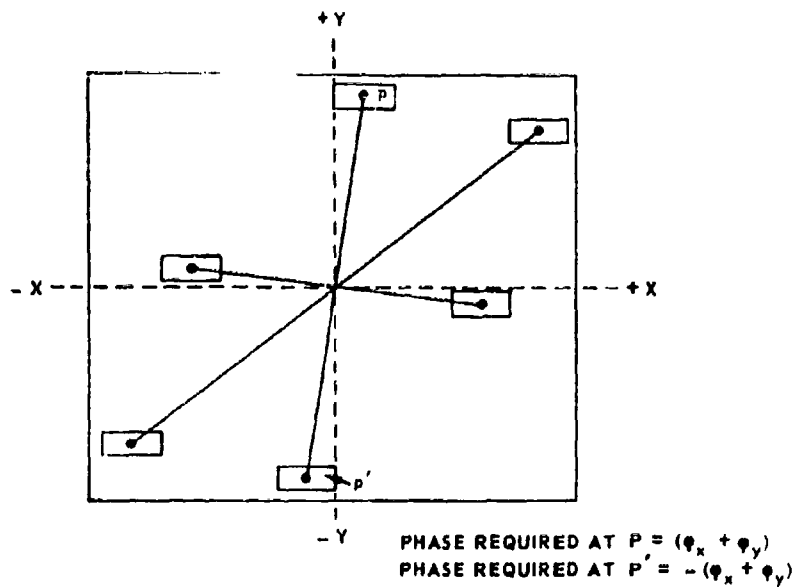


Fig. 2-18 Element Symmetry around the Subarray Center

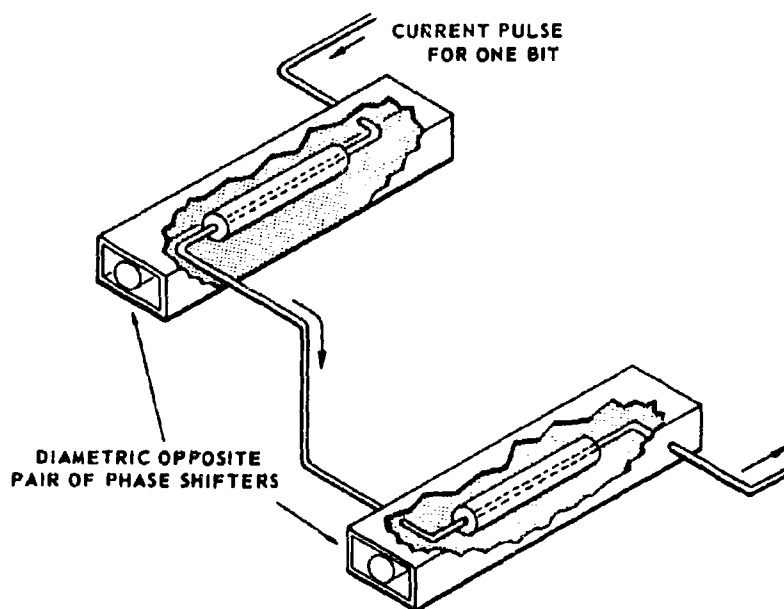


Fig. 2-19 Diametric Opposite Phase Shifter Wiring

different roundoff rule to each phase shifter in the subarray. For this analysis however, it will be assumed for H plane scan that all the phase shifters in one column and their diametric opposites are flipped simultaneously (rows for E plane scan). For these cases, the analysis is that of a linear array.

Consider a linear array of eight isotropic radiators spaced at $\lambda/2$ as shown in Fig. 2-20.

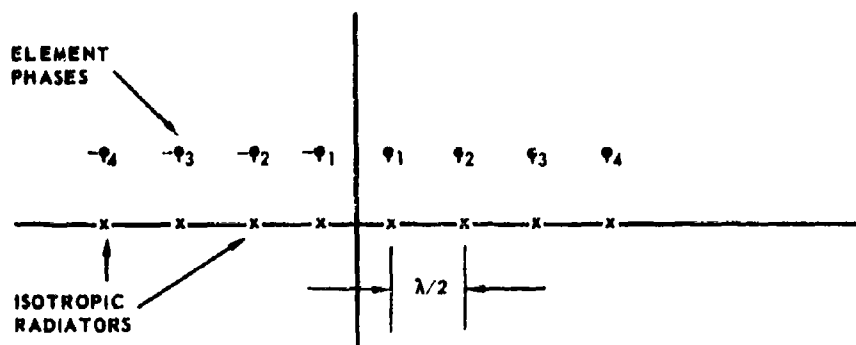


Fig. 2-20 Anti-Symmetrically Phased Array

If the phases to the right of center are $\varphi_1, \varphi_2, \varphi_3, \varphi_4$, and the phases to the left of center are $-\varphi_1, -\varphi_2, -\varphi_3, -\varphi_4$ (i. e., anti-symmetric phasing), then the difference pattern of this array is given by

$$\begin{aligned} \Delta(\theta) = & e^{j(\frac{\pi}{2}\sin\theta - \varphi_1)} + e^{j(\frac{3\pi}{2}\sin\theta - \varphi_2)} + e^{j(\frac{5\pi}{2}\sin\theta - \varphi_3)} + e^{j(\frac{7\pi}{2}\sin\theta - \varphi_4)} \\ & - e^{-j(\frac{\pi}{2}\sin\theta - \varphi_1)} - e^{-j(\frac{3\pi}{2}\sin\theta - \varphi_2)} - e^{-j(\frac{5\pi}{2}\sin\theta - \varphi_3)} - e^{-j(\frac{7\pi}{2}\sin\theta - \varphi_4)} \\ \frac{\Delta(\theta)}{2j} = & \sin(\frac{\pi}{2}\sin\theta - \varphi_1) + \sin(\frac{3\pi}{2}\sin\theta - \varphi_2) + \sin(\frac{5\pi}{2}\sin\theta - \varphi_3) + \sin(\frac{7\pi}{2}\sin\theta - \varphi_4) \end{aligned}$$

For a null of the difference pattern

$$\sum_{n=1}^4 \sin \left[(2n-1) \frac{\pi}{2} \sin \theta_0 - \varphi_n \right] = 0.$$

If the phases $(\varphi_1, \varphi_2, \varphi_3, \varphi_4)$ are nearly those required to point the beam in a direction θ_0 , then $\sin(\arg) \approx \arg$ for each term in the summation and

$$\sum_{n=1}^4 (2n-1) \frac{\pi}{2} \sin \theta_0 - \varphi_n = 0,$$

letting

$$\frac{\pi}{2} \sin \theta_0 = x,$$

$$\sum_{n=1}^4 (2n-1)x - \varphi_n = 0,$$

$$\sum \varphi_n = x + 3x + 5x + 7x = 16x,$$

or

$$x = \frac{\pi}{2} \sin \theta_0 = \frac{\sum \varphi_n}{16}$$

$$\sin \theta_0 = \frac{1}{8\pi} \sum \varphi_n.$$

When the phase at any symmetric pair of radiators is changed by $\frac{\pi}{8}$, the beam will be tilted by

$$\Delta \sin \theta = \frac{1}{8\pi} \times \frac{\pi}{8} = \frac{1}{64}.$$

It should be cautioned, in using this technique, the phase of each element should be close to the rf phase required to point the beam to a direction θ_0 (i. e., within $\frac{\pi}{8}$).

To extend this analysis to a linear array of any size using a 4-bit phase shifter, the steering increment in $\sin\theta$ space will be

$$\Delta\sin\theta = \frac{1}{m^2} \quad m = \# \text{ elements spaced at } \lambda/2.$$

In terms of beamwidth

$$\text{assuming } BW = \frac{\lambda}{a} = \frac{\lambda}{m\lambda/2} = 2/m \quad a = \text{aperture size}$$

$$\frac{\Delta\sin\theta}{BW} = \frac{1/m^2}{2/m} = 1/2m \quad \lambda = \text{free space wavelength.}$$

In the H plane where $m = 8$, the beam steps in increments of $1/16$ of a beamwidth for an increased phase of one bit applied by diametric wiring to a pair of elements.

In the E plane where $m = 12$ and the spacing is approximately $\lambda/3$, a similar analysis shows that the beam will step by $1/24$ of a beamwidth for an increased phase of one bit applied to any pair of elements.

2.2.5 Phase Quantization and Roundoff Rules

Because of the digital nature of the phase shifters, the computed phases must be quantized using some roundoff procedure. The roundoff rule originally selected does not appear to be best from the standpoint of quantization lobe formation as may be observed in the array patterns presented in Section 3.5. The results of subsequent roundoff rules (also in Section 3.5) show a marked improvement in grating lobes. However, the original roundoff rule will be discussed since the majority of the

measurements were made using this system. The slight modification required for grating lobe suppression will then be indicated. Note that these rules are significantly influenced by the diametric wiring of the subarray.

The roundoff rule was:

1. Compute the exact phase required, relative to zero phase at the center of the array.
2. Roundoff to next lower phase shifter setting (i. e., disregard any computed bits smaller than $\pi/8$).

Consider a 4-bit phase shifter with bit sizes of π , $\pi/2$, $\pi/4$, $\pi/8$.

Figure 2-21 represents the quantized phase resulting from the use of this roundoff rule. Note that a line drawn through $-\pi/16$ at an

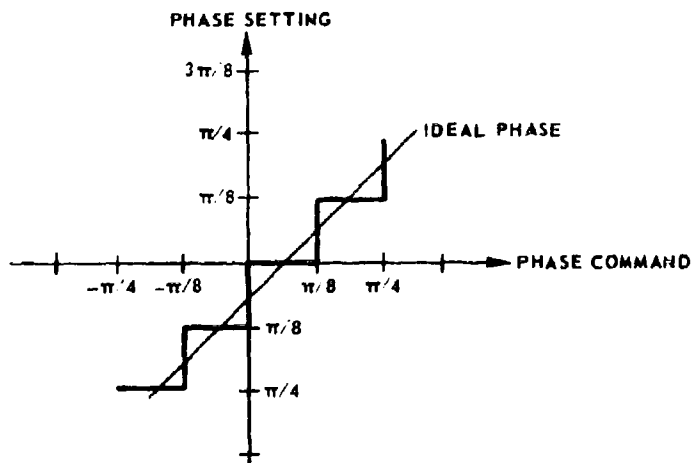


Fig. 2-21 Phase Quantization with Bit Size of $22\frac{1}{2}^\circ$

angle of 45° bisects all of the phase steps. This line represents the ideal phase and none of the phase shifters (including those diametrically wired) ever vary by more than $\pi/16$ ($11\frac{1}{4}^\circ$) from this ideal

phase. The center of the ideal phase curve does not pass through the origin because a phase shifter with bit sizes π , $\pi/2$, $\pi/4$, $\pi/8$ is short of 2π by $\pi/8$.

When the subarray is phased for boresight, half the elements have a relative phase setting of 0° . Because of the diametric wiring, the other elements have a relative phase setting of $337\frac{1}{2}^\circ$ (or $-22\frac{1}{2}^\circ$). The occurrence of a phase split at boresight (rather than another pointing direction) is perhaps fortunate since boresight patterns are usually among the first taken. Therefore, the most undesirable consequence of diametric wiring is immediately demonstrated. This boresight beam represents a worst case in that all phase shifters are $11\frac{1}{4}^\circ$ from the ideal.

For temperature compensation, the phase shifters designed for this program possess 382° of differential phase. For diametric wiring, the decision rule for this quantity of differential phase is to add $23\frac{3}{4}^\circ$ and roundoff to the next lower setting.

Figure 2-22 shows how this type of decision rule comes within $\pm 12\frac{5}{8}^\circ$ of the ideal phase. Note that the ideal phase curve in this case

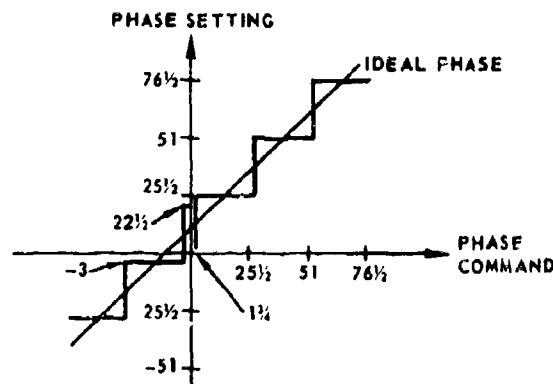


Fig. 2-22 Phase Quantization with Bit Size of $25\frac{1}{2}^\circ$

is $22\frac{1}{2}^\circ$ higher than the previous case. This represents a constant bias to every phase shifter (including those diametrically driven) and has no influence on steering.

In determining the phase commands, the computation was performed for the upper half (E vector is pointed up) of a subarray. This was not the wisest choice in that at boresight a $22\frac{1}{2}^\circ$ split occurred in the center of the array as shown in Fig. 2-23. The phase split caused the supposed boresight beam to tilt approximately 2° . This beam tilt does not affect the pointing of the full array, but it does affect the grating lobes (see Section 3.5).

For grating lobe suppression, the effects of the phase split may be alleviated by modifying the roundoff rule. The addition of a slightly different computational bias to alternate phase shifters will tend to break up the split phase periodicities and result in a decreased grating lobe level. This result has been observed in recent experiments and is reported in Section 3.5.

2.2.6 Assembly of a Subarray

Prior to assembling a given subarray, all of the phase shifters assigned to this subarray had been tested. In addition to having good VSWR, insertion loss, and differential phase characteristics, the phase shifters selected for any given subarray were all within $\pm 8^\circ$ in insertion phase. The 1:4 power splitter and at least one of the E plane horns had also been tested.

First, the 1:4 power splitter and four E plane horns were assembled into a 1:48 power divider. A mounting plate was then mated to each of the E plane horns with stainless steel screws. A photograph

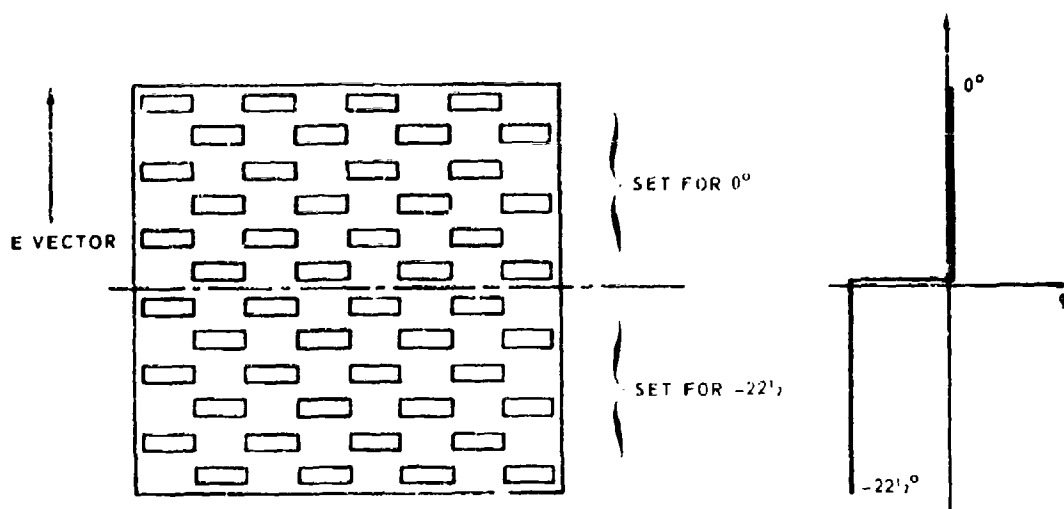


Fig. 2-23 Phase Split Across Aperture at Boresight

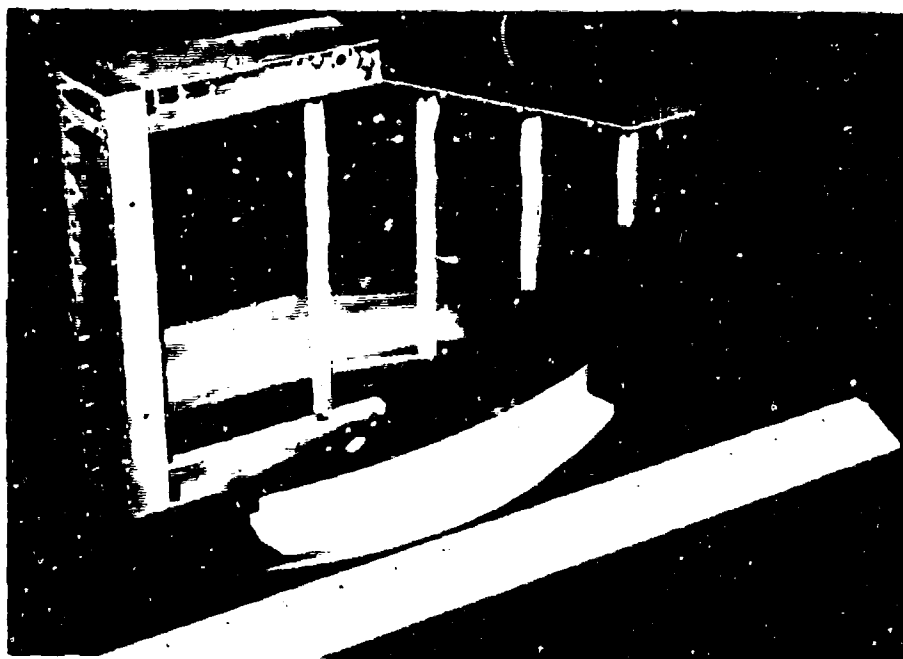


Fig. 2-24 E Plane Horn with Mounting Plate

of the mounting plate mated to the E plane horn is shown in Fig. 2-24. The mounting plate provides matching between the horns and the phase shifters and also provides a solid structure for anchoring the phase shifters. After each phase shifter was fastened to the mounting plate (again using stainless steel screws), the position of the radiating end was checked to ensure the proper triangular spacing at the aperture.

For wiring purposes, it was necessary to first mount the two central rows of phase shifters (four phase shifters per row) and then work outward. This restriction was imposed by the diametrically opposite wiring discussed in Section 2.2.4. A photograph showing two central rows and one additional phase shifter wired in place is shown in Fig. 2-25. Each phase shifter was wired to the diametrically opposite phase shifter and to the subarray connector. After the two central rows had been wired in place, the rf differential and insertion phases were checked by flipping each bit at the connector. When it was determined that every bit on every phase shifter was functioning properly, the next two rows of phase shifters were mounted and the procedure repeated until all of the phase shifters were mounted, wired and tested.

A faceplate (Fig. 2-26) was then fitted over the radiating end of all the phase shifters. Finally, a thin sheet of dielectric material was attached to the face plate by the use of nylon screws and polystyrene spacers. This thin sheet provides some compensation for the variation of impedance with scanning.

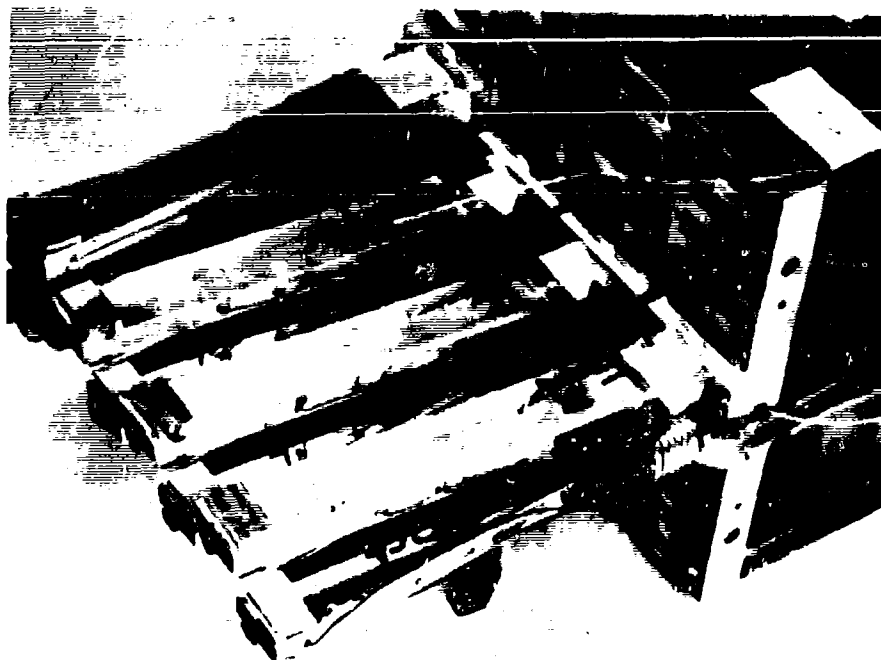


Fig. 2-25 Phase Shifter Wired in Place

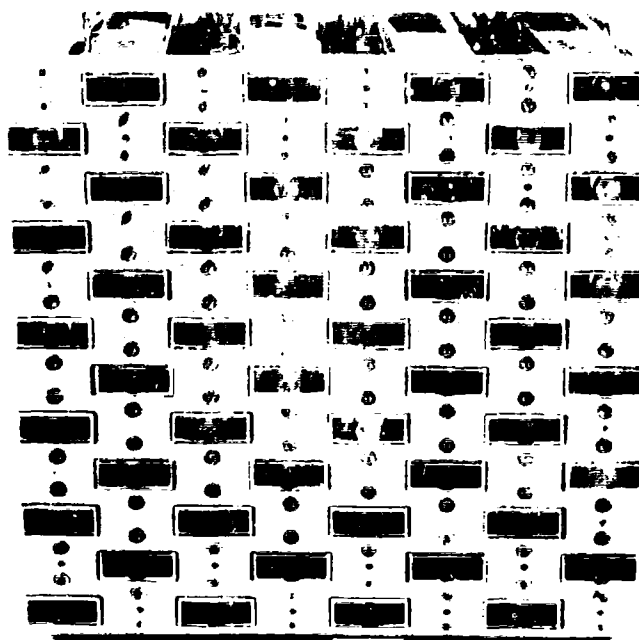


Fig. 2-26 Face Plate

2.3 Power Divider (H. M. Grady)

2.3.1 Introduction

An essential component of a phased array is the power divider. For this program, a previously designed 1:48 power divider was modified to meet the lightweight and close spacing requirements of an array of subarrays. Emphasis was placed on obtaining a geometry wherein the radiating face appears as a regular array of radiators with no discontinuities to mark the edges of a subarray. This goal was achieved with a resultant suppression of the grating lobes. Two types of components comprise the power divider, a 1:4 H plane power splitter and a 1:12 E plane horn. Both are shown in Fig. 2-27.

The power divider was designed to provide approximately equal amplitude and phase to each radiating element in the subarray. Constant amplitude is desired so that the array of subarrays will appear as a continuous aperture. If the distribution across the subarray is other than constant, amplitude periodicities will occur across the array face, causing undesired grating lobes.

Constant phase across the subarray is not a basic requirement since the phase shifters may be programmed to correct for any known phase distribution. A spherical phase distribution may even result in a pattern improvement in that the spherical phase correction will tend to break up the periodicities in phase quantization (caused by using digital phase shifters), and thereby reduce the peak quantization lobes. In this design, however, the spherical phase front was corrected by the use of a dielectric lens in each horn.

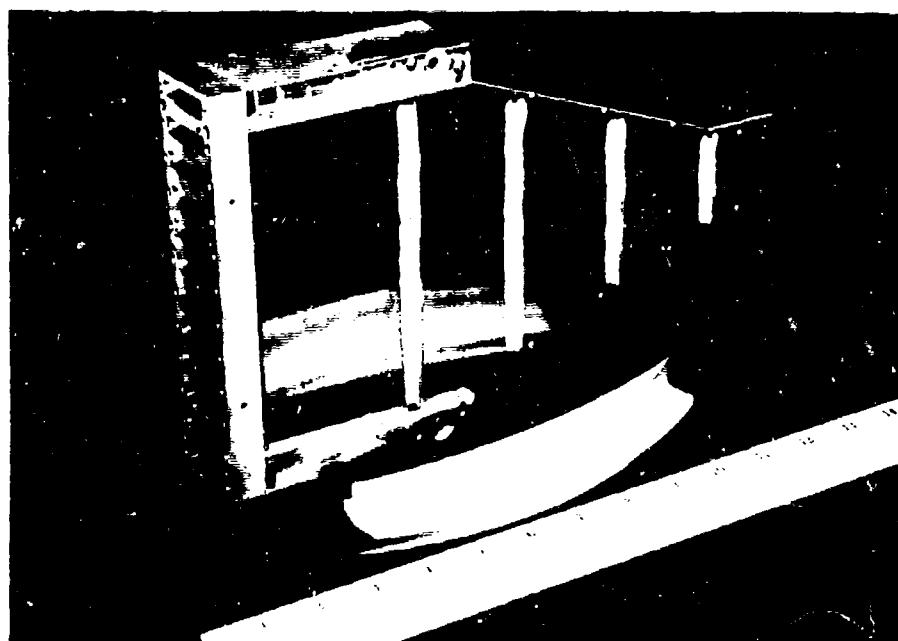
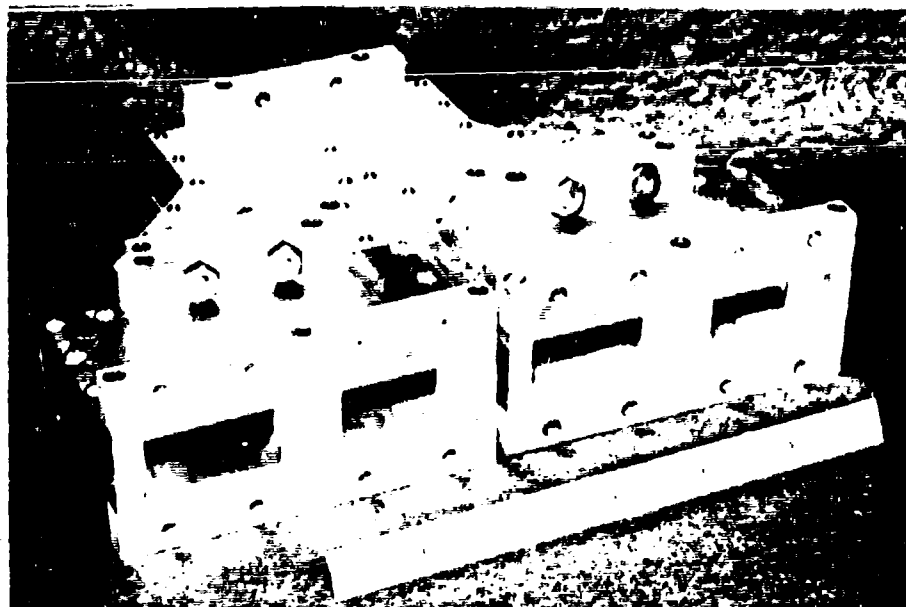


Fig. 2-27 1:4 H Plane Splitter and 1:12 E Plane Horn

Since the lens equalizes all path lengths and the nonreciprocal phase shifters have a constant two-way insertion phase, the reflections from the radiating surface are collimated at the input where the VSWR may therefore be measured. Without a lens, the reflected power would have been scattered partially to side-lobe regions. Further, the spherical phase correction permits a simplified wiring and driving method, using diametric symmetry. Diametric driving is discussed in Section 2.2.4.

A prime consideration in the design of a parallel feed is the interelement spacing. For operation over a range of scan angles with the exclusion of grating lobes from visible space, the maximum spacing between elements is given by

$$\frac{d}{\lambda} = \frac{1}{1 + \sin\theta}$$

λ = wavelength in inches

d = maximum spacing in inches

θ = maximum scan angles.

For a maximum scan angle of 60° , the interelement spacing is limited to a maximum of 0.54λ . This spacing places restrictions on the form of the feed structure. This difficulty is circumvented by using space in the E plane where there are no cutoff restrictions. The 1:12 E plane horn uses the standard waveguide width. As shown in Fig. 2-28, one horn is used to feed two adjacent columns of elements on a triangular grid alleviating the space restriction in the H plane.

As the first few 1:4 power splitters and 1:12 E plane horns were completed, extensive tests were performed to determine the phase and amplitude variations. Samples of the remaining components were measured to ensure that the performance was unchanged. Further, swept VSWR measurements were performed on both the 1:4 power splitters

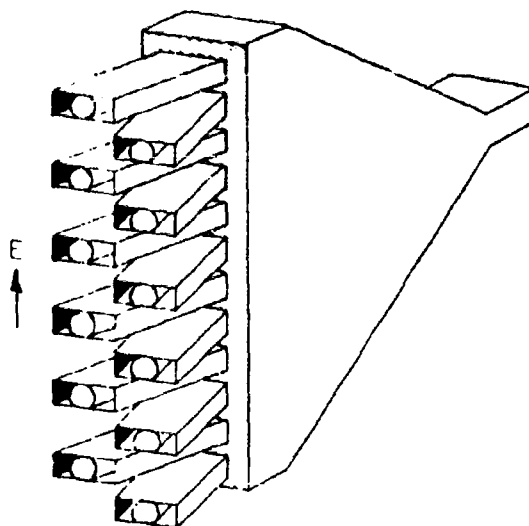


Fig. 2-28 Power Divider for Two Adjacent Columns of Elements

and the E plane horns. The results of these tests are summarized below and in Table 2-2. A block diagram of the test setup is shown in Fig. 2-29.

2.3.2 Results

1:4 Power Splitter

VSWR--Due to the low VSWR associated with the 1:4 power splitter, it was felt that swept VSWR measurements would not suffice. Slotted line measurements were made at 50 mc intervals across the band on every power splitter. The results showed that all were below 1.09 over the band. The average VSWR was 1.06. Swept measurements over the band were also performed on all power splitters, and were in close agreement with the slotted line measurements. A typical swept VSWR measurement is shown in Fig. 2-30.

Table 2-2
Power Divider Characteristics

	1:4 Power Splitter	1:12 E Plane Horn (including lens)
Maximum VSWR	1.09	1.18
Average VSWR	1.06	1.10
Maximum Phase Variation	$\pm 2^\circ$	$\pm 9^\circ$
Maximum Amplitude Variation	± 0.25 db	± 1.85 db
Weight	2.17 lb	2.13 lb (including mounting plate)

Cost of 1:48 Power Divider - \$1490
(components and assembly)

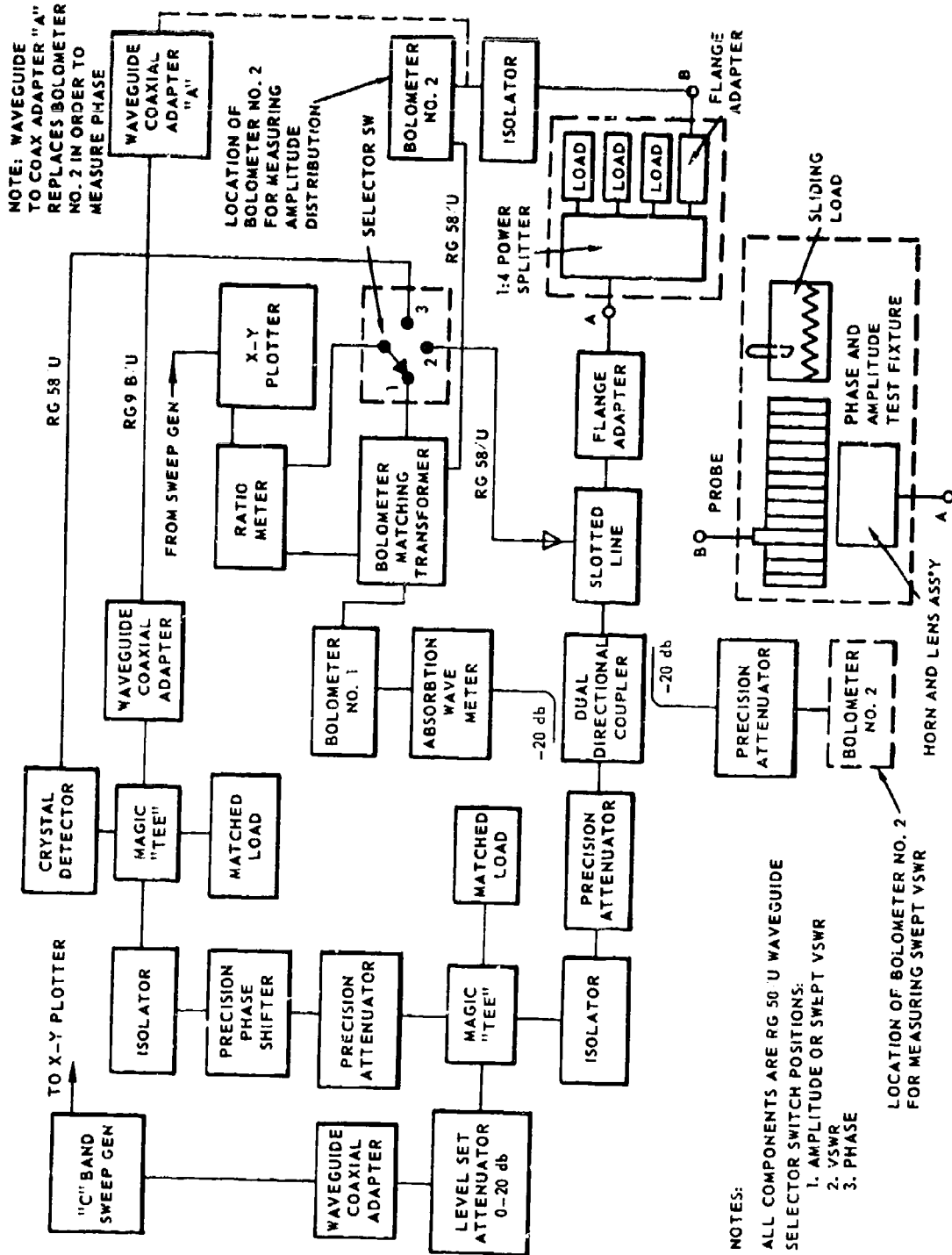


Fig. 2-29 Instrumentation used for Testing 1:4 Power Splitters and 1:12 Horns

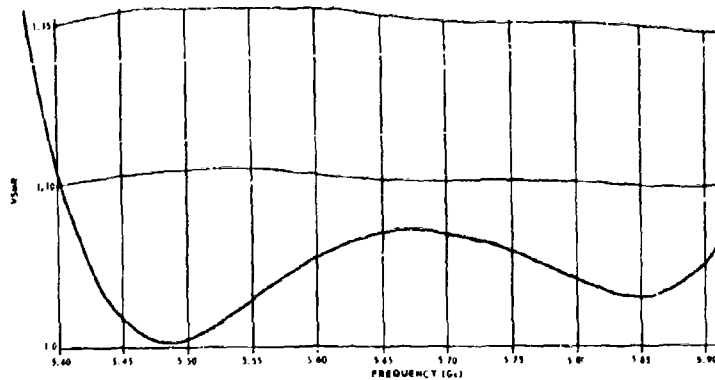


Fig. 2-30 VSWR Variation with Frequency, 1:4 H Plane Power Divider

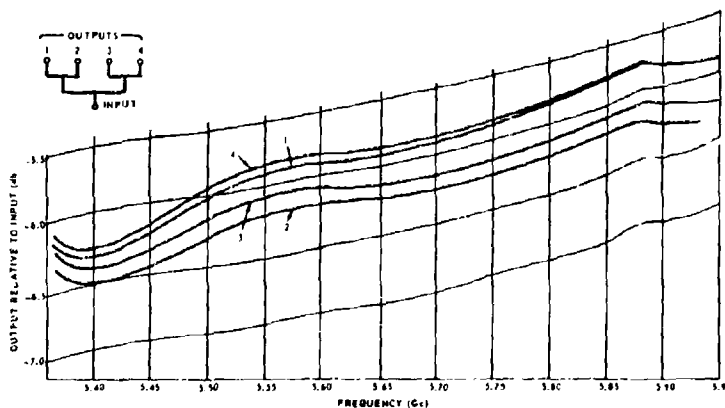


Fig. 2-31 Amplitude Variation with Frequency, 1:4 H Plane Power Divider

Phase Variation--Insertion phase was measured on five of the splitters. Each unit was measured at three frequencies. The maximum phase variation observed from port to port was $\pm 2^\circ$.

Amplitude Variation--Swept amplitude measurements over the band were performed on every splitter. All ports were within ± 0.25 db of each other. A typical measurement showing the variation in amplitude is given in Fig. 2-31.

E Plane Horn (including lens). The first eight horns (for use in the first two subarrays) were all tested as described below. Thereafter, every fourth horn was tested.

VSWR--Accurate measurements were performed using a slotted line (and a sliding load) at 50 mc intervals. In addition swept measurements were performed over the band to ensure that there were no resonances. The largest VSWR recorded was 1.2. The VSWR was 1.1 when averaged over the band. As previously noted, the E plane horn is not quite matched over the desired frequency band. It may be seen upon examination of Fig. 2-32, that the horn is matched over a 10% band which is 50 mc higher than anticipated. A good match over the proper band may be achieved by increasing the "H" dimension of the waveguide by only 0.020 inch.

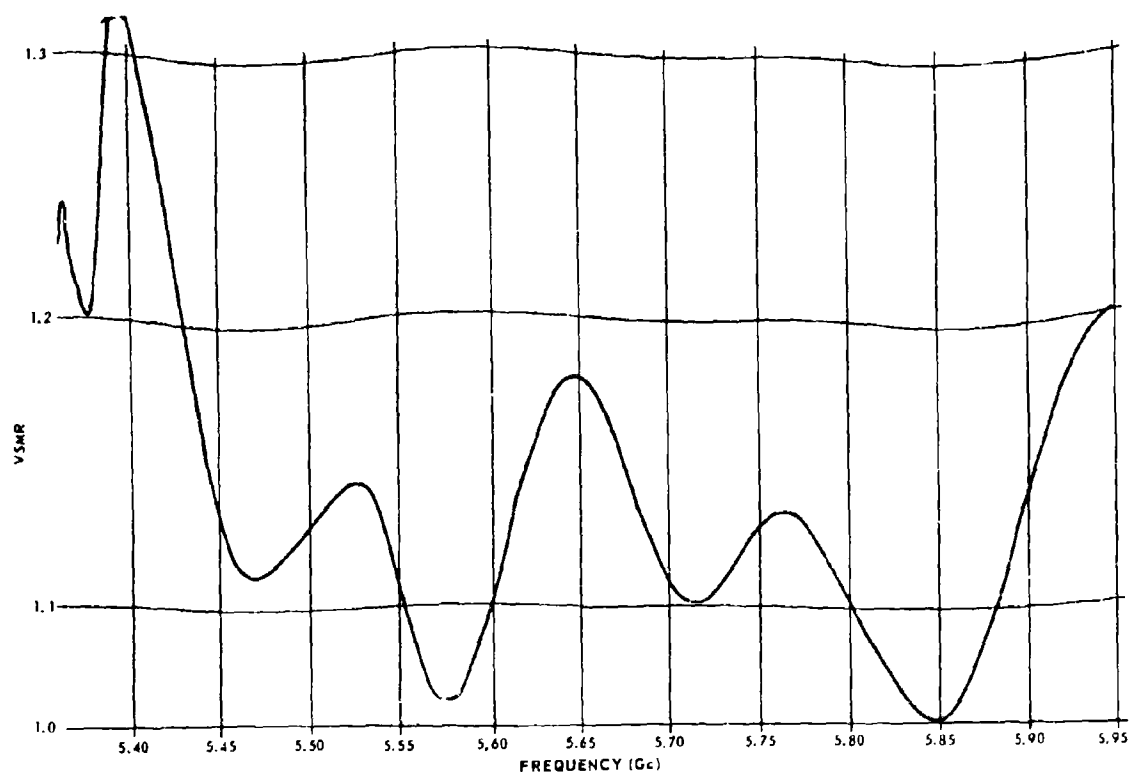


Fig. 2-32 VSWR of Lens Corrected Horn

Amplitude Variation--The amplitude variation across a horn was measured using a test fixture consisting of a stack of waveguides aligned in the E plane. All of these waveguides were terminated except the one used to measure the variation across the aperture. The variation measured at three frequencies, is shown in Fig. 2-33. Swept

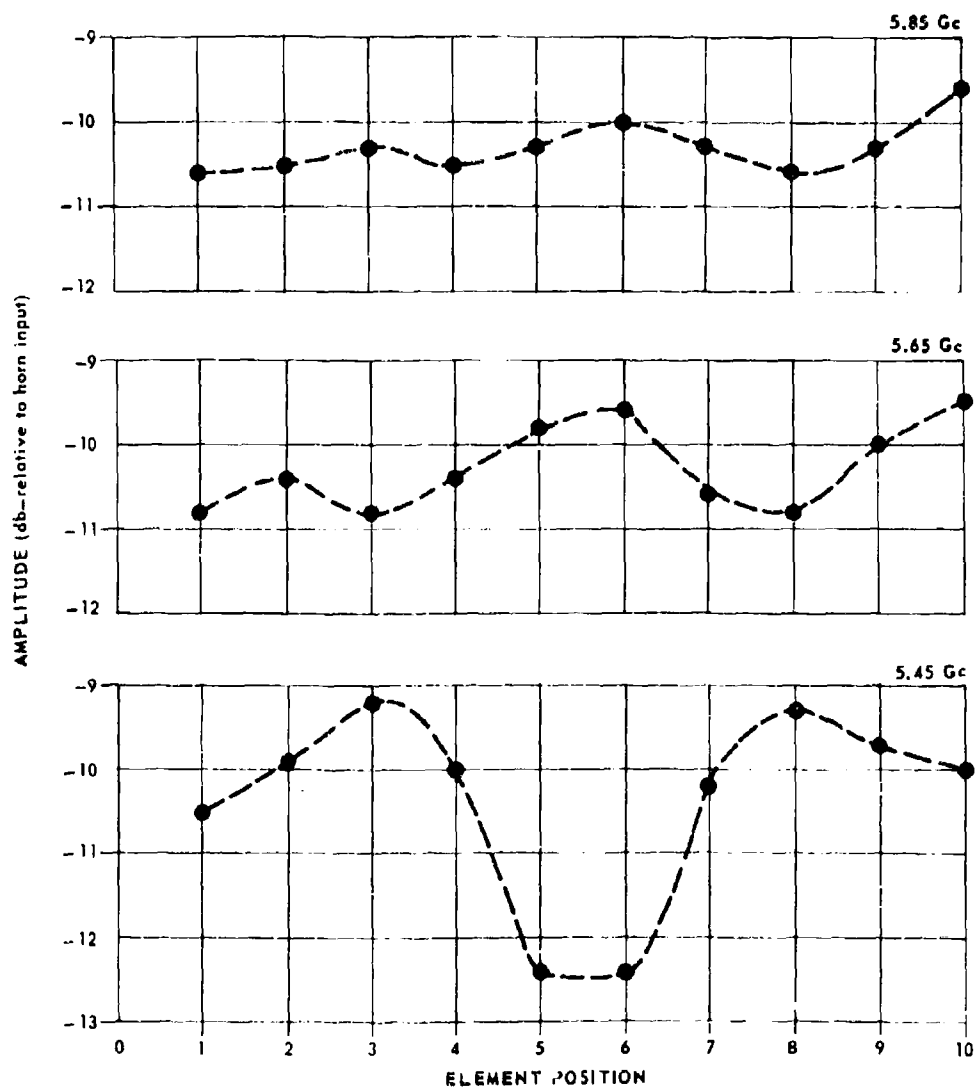


Fig. 2-33 Amplitude Variation across Lens Corrected E Plane Horn

measurements of amplitude were performed at several locations across the mouth of the horn. The amplitude variation was never greater than ± 1.85 db. Typical measurements are seen in Fig. 2-34.

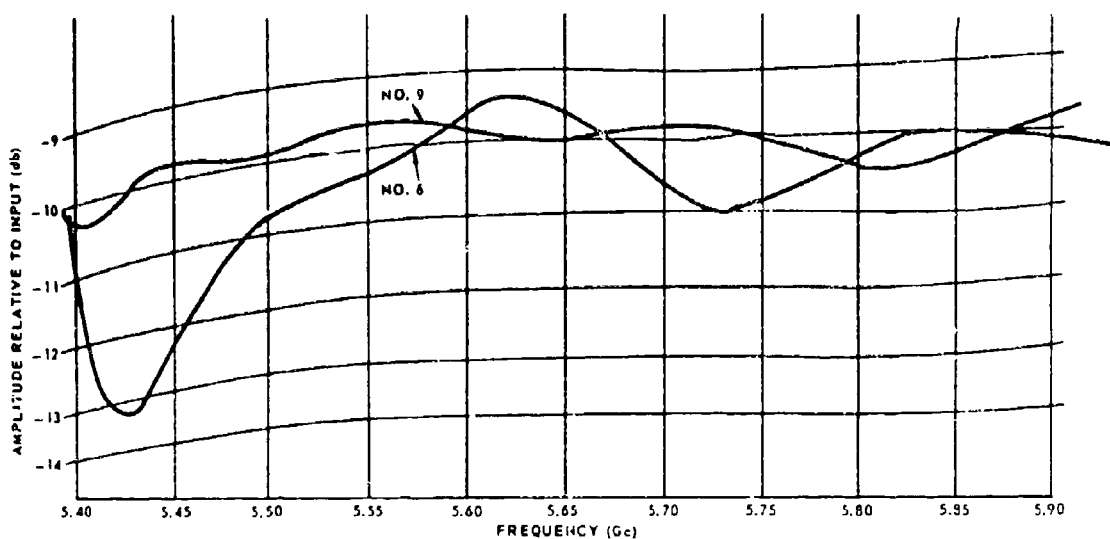


Fig. 2-34 Amplitude Variation with Frequency, E Plane Horn and Lens

Phase Variation--Phase measurements across the horn aperture were performed at three frequencies. The results showed greatest variation of $\pm 9^\circ$ of rf phase across one of the horns. On the average, the maximum variation across a horn was $\pm 5^\circ$. The phase distribution across a typical horn (including the lens) is shown in Fig. 2-35.

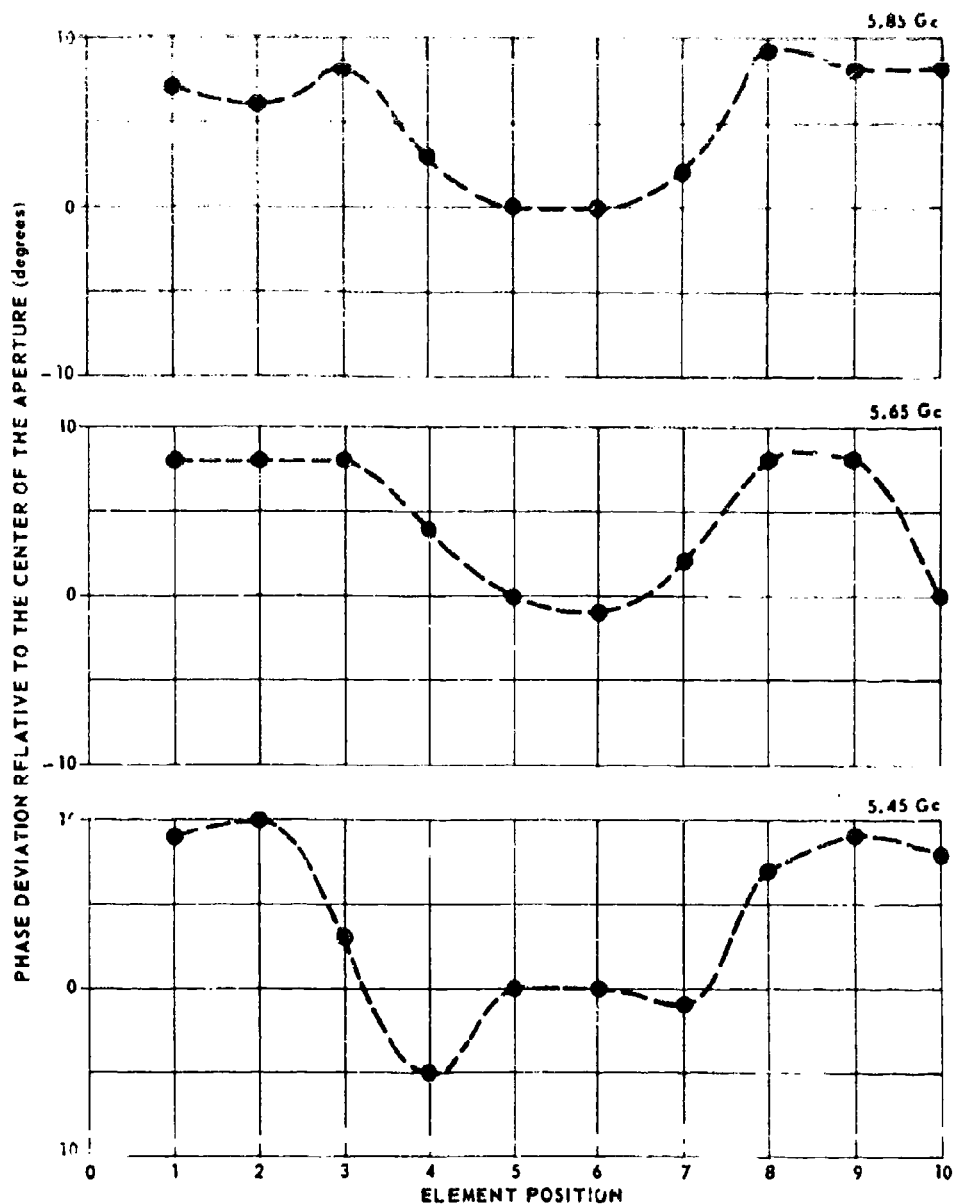


Fig. 2-35 Phase Variation across Lens Corrected E Plane Horn

2.3.3 Design of Power Divider Components

1:4 Power Splitter. The 1:4 H plane splitter is made up of two 1:2 type A power splitters and one 1:2 type B power splitter,

as shown in Fig. 2-36. By breaking up the 1:4 power splitter in this fashion, it was possible to simplify the machining operations. Each of the 1:2 power dividers was matched at a point close to the junction to provide a broadband match.

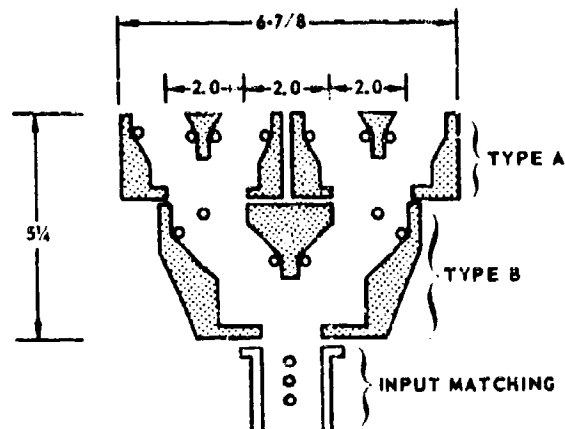


Fig. 2-36 1:4 Power Splitter

The 1:4 power splitter is constructed of aluminum, and fastened together with stainless steel screws for compatibility. Two fixtures were constructed, one each for type A and type B power splitter, which accurately located the various parts of the power divider in their proper relationship. The parts were held in these fixtures during the drilling and planing operation. The results of this procedure were assemblies that were reproducible, as can be seen in the test results. To maintain an input VSWR below 1.10, it is necessary to adjust the input matching stubs on each assembly. These matching stubs are located in the waveguide section that mates with the power divider and forms the support structure for the phase shifter driver cards.

E Plane Horn. The E plane sectoral horn developed as a 1:12 power splitter is both lightweight and simple to construct (Fig. 2-37). It provides nearly a constant amplitude distribution across the aperture thereby tending to suppress the grating lobes in an array of subarrays.

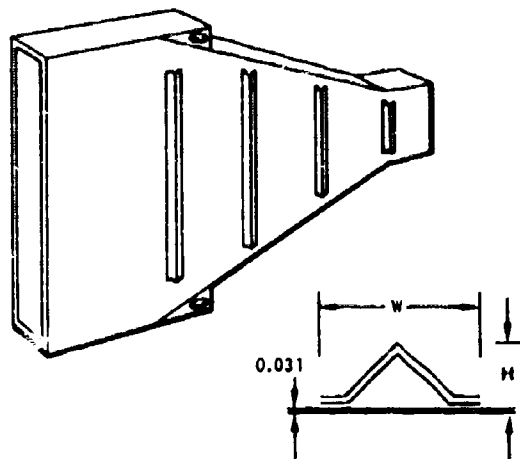


Fig. 2-37 1:12 E Plane Horn

After considering several methods of horn construction, precision casting appeared to offer a method that would provide a low-cost, lightweight device. However, after discussing the dimensions and tolerances of the horn with representatives of several manufacturers, it was apparent that our requirement could not be met by this method. It was decided that machined parts would better meet the construction tolerances for the relatively small quantity required.

The narrow wall of the horn was machined from aluminum stock to a thickness of 1/8 inch with a heavier triangular section at each end. These heavier sections provide mounting surfaces for connecting the horns to adjacent components in the subarray. The broad walls of the horn were made from 1/32-inch stock aluminum sheet machined to the

contour of the horn. Since energy is propagated through the horn with the E field parallel to the broad wall, any variation in the dimension between the broad walls will cause a change in the guide wavelength and a corresponding change in phase across the aperture of the horn.

To hold the phase across the aperture to within 10°, the dimension between the horn walls must be held to a tolerance of ± 0.005 inch. After machining, the broad walls were warped in excess of this tolerance; this warping was corrected by placing the walls on a surface plate and holding them flat with weights while bonding (with an epoxy cement) thin aluminum stiffeners to each wall in four places. Figure 2-37 shows the shape of the stiffeners. After the epoxy had cured, a number of walls were checked for flatness along the direction of the stiffeners, the maximum deviation measured was 0.003 inch.

The horn components were assembled and held in exact alignment in a fixture during the drilling of screw and alignment pin holes. After tapping holes in the narrow wall, the horn was reassembled and its walls fastened together with stainless steel screws. The final operation performed on the horns was to machine the overall length and the mounting surfaces to tolerance.

The horns were then degreased and a 1/16 inch radius bead of conductive epoxy was applied to the inside corners of the horn to prevent rf leakage. A lens was inserted into each horn and bonded in place with Duco cement. The final operation was the placement of a small piece of aluminum tape across the small end of the horn. This acted as an inductive iris which reduced the "a" dimension of the horn from 1.372 inch to 1.100 inch and corrected for the discontinuity caused by the flare in the E plane. Additional details may be found in Ref. 5.

Lens. The E plane horn was constructed with an $\frac{f}{D}$ of 1.3 which made it reasonably compact without introducing serious amplitude taper in the aperture. This short focus does, however, give a spherical phase distribution across the aperture of 65° at 5.65 Gc. This spherical distribution was corrected by inserting a lens in each horn. The purposes of this method of correction are: (a) with uniform phase across the horn aperture, the mismatch of the four sections of the radiating face of the subarray are brought back to the input of the 1.4 power divider in phase and, therefore, can be measured, and (b) the computer load is reduced since no spherical phase corrections are required.

Initially two lenses were designed for evaluation. Mod I was a convex-planar lens, i. e., one-surface plane and the other curved while Mod II was a two-curved surface lens whose rear surface was at a radius the length of the horn wall from the focus. The Mod I lens had an edge-dimming characteristic, i. e., the illumination at the edges of the lens horn assembly was down approximately 3 db, while the Mod II lens exhibited edge-brightening characteristics of approximately 2.0

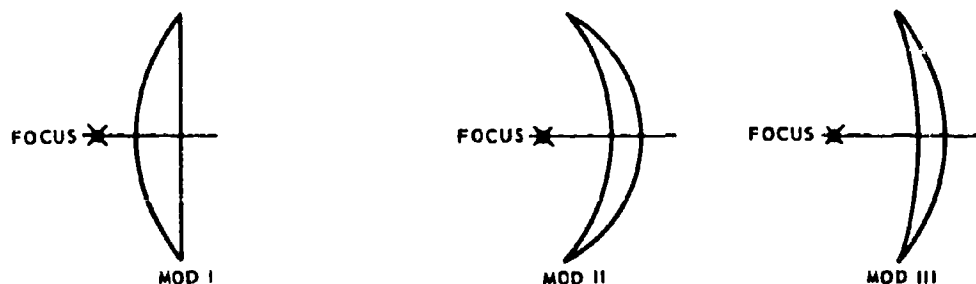


Fig. 2-38 Lens Curvature Design

db. The lens configuration that was used in the eight subarrays was a compromise between Mods I and II in that it was a two-curved surface lens, but with less curvature than Mod II, the rear surface being at 1.5 times the radius of Mod II. This lens, Mod III, gave an amplitude variation across the aperture of between 1.0 and 2.0 db over most of the band. The three general lens shapes are shown in Fig. 2-38.

Both surfaces of the lens were matched with a narrow slab of polystyrene approximately a quarter wavelength long placed along the center of both faces of the lens.

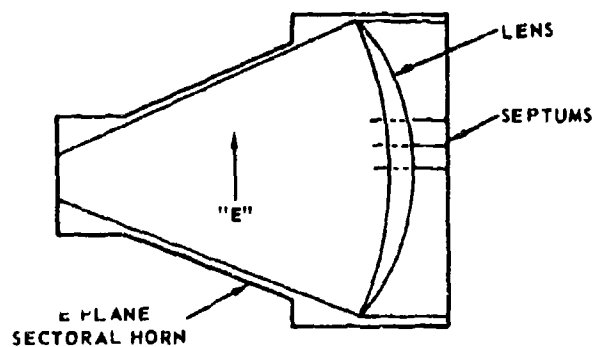


Fig. 2-39 Lens Matching

Lens Matching. Figure 2-39 illustrates an E plane horn and lens. Conceptually, thin septa may be placed in the aperture, normal to the E field, without causing a reflection. The region bounded by two septa and the walls of the horn form a waveguide having an impedance determined by the spacing of the septa and the width of the horn. By spacing the septa at 0.622 inch, we then have the horn and lens

facing a stack of RG 50/u waveguides since the dimensions of the horn in the H plane is identical to that of RG 50/u. Each of these waveguides may be terminated in its characteristic impedance and would then appear to the lens and horn as a matched load. By extending the septa through the lens, it is apparent that the lens-matching operation is equivalent to one of matching a polystyrene block in an RG 50/u waveguide.

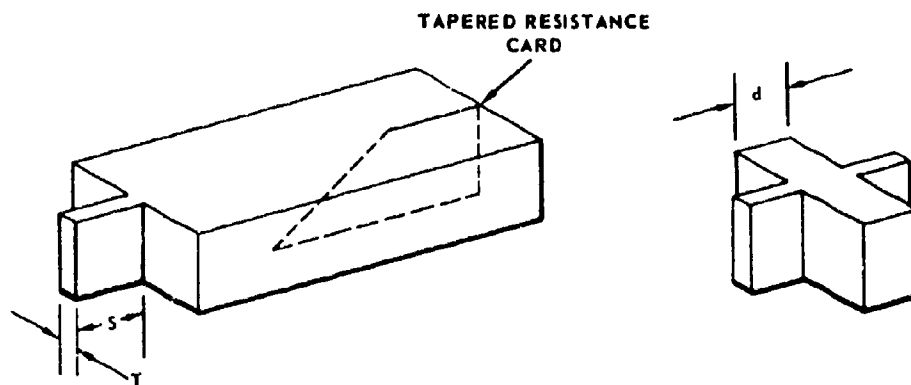


Fig. 2-40 Waveguide Technique for Lens Matching

Figure 2-40 shows a polystyrene block with the matching slab at one surface, and a resistance card termination. The dimensions "s" and "t" were adjusted to produce a $\lambda/4$ section of the proper impedance to match the air filled waveguide to the dielectric filled and terminated waveguide. After determining the optimum dimension, several short blocks were constructed with the matching slab on two surfaces.

These blocks were of differing thickness "d" representing several locations along the lens. VSWR measurements of these sections showed the match was only slightly affected by the lens thickness, and the lens VSWR should not exceed 1.15 over the band. The measured VSWR of the horn and lens together was approximately 1.10 over most of the band rising to a maximum of 1.18 at the low end of the band.

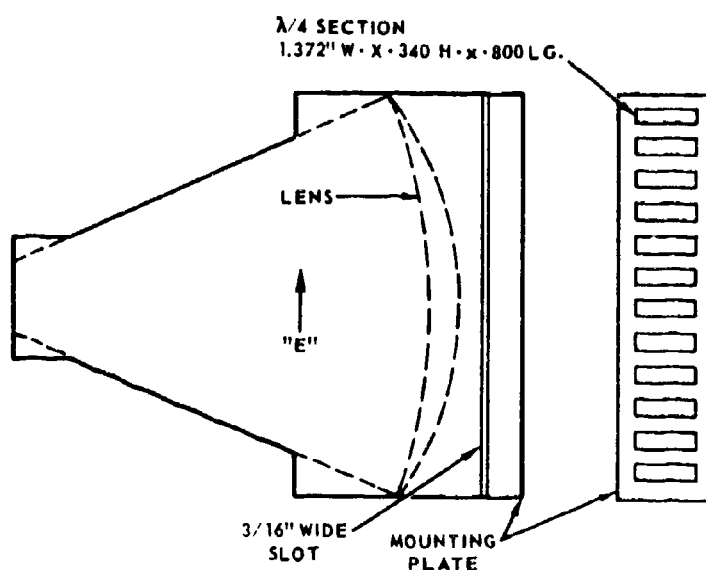


Fig. 2-41 Mounting Plate

Mounting Plate. Located in the aperture of the horn is the mounting plate (see Fig. 2-41). This unit provides a surface to which the phase shifter elements are attached, it also contains the quarter wave step which forms a part of the structure which matches the horn to the phase shifters.

After attaching the mounting plate to the horn, the amplitude appearing at each port was measured with a sweep generator and a ratio meter. This measurement showed a sharp loss of approximately 6 to 8 db in the power transmitted through the horn at two frequencies in the band.

Further examination showed this effect was caused by the excitation of a mode having a polarization orthogonal to the desired mode. The lens appears to be the element responsible for exciting the undesired mode since the loss spikes are not present when the lens is removed from the horn. As the rf energy propagates through the lens towards the mounting plate, apparently a small portion of this energy is transferred into an orthogonal mode. Upon reaching the mounting plate, the undesired mode is reflected since the $\lambda/4$ sections are cut-off to an orthogonal mode. The horn now becomes a high Q cavity for this mode since it cannot propagate back through the horn input port which is cutoff for this mode. At two frequencies in the band, conditions are such that the horn resonates and most of the input energy is transformed into the orthogonal mode, causing the aforementioned transmission loss spikes.

This problem was corrected by placing a 3/16 inch wide slot across the broad wall of the horn at the point where the horn and the mounting plate meet. This slot is very lightly coupled to the mode that is being transmitted, but is very tightly coupled to the undesired orthogonal mode. The slot couples the orthogonal mode to the exterior of the horn where it is absorbed in a 3/16 inch thick sheet of microwave absorber. The slot introduces no measurable loss to the desired mode.

2.3.4 Special Test Fixtures

To perform the several measurements of phase and amplitude across the horn aperture, a simple test fixture was designed which enabled accurate measurements to be taken rapidly. The test fixture consisted of a group of 19 short lengths of RG 50/u waveguide soldered broad wall-to-broad wall. The center waveguide contained an isolator and a detector, the nine waveguides on each side were terminated in resistance card loads (see Fig. 2-42).

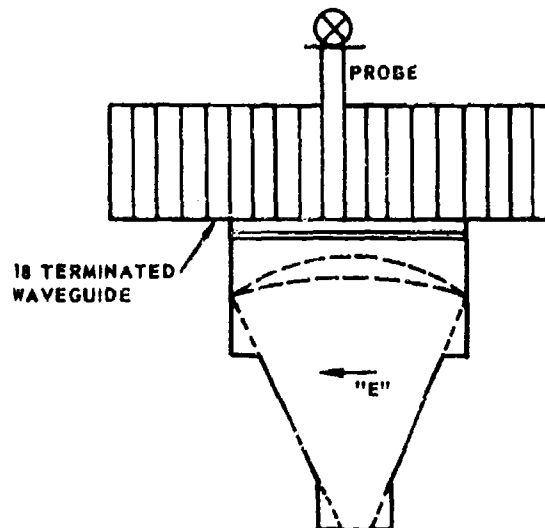


Fig. 2-42 Test Fixture for Aperture Phase and Amplitude Measurements

The device can be slid across the horn to examine the amplitude and phase at various positions. The waveguide assembly is matched by means of a quarter wave transformer which compensates for the finite wall thickness between elements.

A sliding load was required for accurate measurements of the horn and lens (Fig. 2-43). This unit consists of a section of waveguide

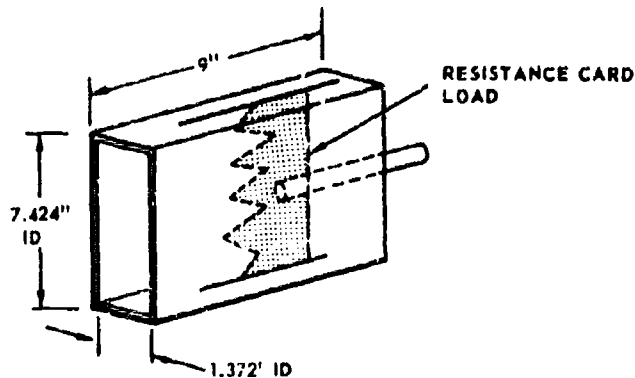


Fig. 2-43 Sliding Load

having the same cross section as the E plane horn, i. e., 1.372 inches in the H plane and 7.424 inches in the E plane. The center of the narrow wall is slotted to accept a resistance card and hold it in the center of the waveguide. Using the sliding load technique, it was possible to accurately measure the VSWR of the horn and lens assembly with the assembly terminated in a less than perfect load. With the fixture connected to the aperture of the horn, two values of VSWR are measured, ρ_{\max} . (load positioned to produce maximum VSWR) and ρ_{\min} . (load positioned to produce minimum VSWR). The two mismatches producing these readings are:

$$\rho_1 = \sqrt{\frac{\rho_{\max}}{\rho_{\min}}} \quad \text{and} \quad \rho_2 = \sqrt{\rho_{\max} \rho_{\min}}.$$

2.4 Phase Shifter (C. A. Shipley)

2.4.1 Summary and Results

A 4-bit latching ferrite phase shifter is used for steering the subarray beam. A photograph of the phase shifter (Ref. 6) is shown in Fig. 2-44 and a summary of the characteristics is given in Table 2-3.

The phase shifter was designed to provide a minimum system cost and weight while maintaining good microwave performance. Briefly, the phase shifter is a digital device where each bit is activated by a short current pulse which flips the direction of magnetization, changing the propagation constant and, hence, effecting a change in phase. The desired value of phase is retained until a current pulse of the opposite polarity resets the bit. The magnitude of the phase shift is controlled by using digital bits of differing lengths. A 4-bit phase shifter would generally have lengths giving phase shifts of 180° , 90° , 45° , and $22\frac{1}{2}^\circ$.

The phase shifters for this program were designed for 10% more phase shift (198° , 99° , etc.) which permits a reasonable amount of temperature compensation. This is desirable since the material being used (TT1-109) exhibits a loss in remanence magnetization (and differential phase shift) with increasing temperature. The loss in phase shift amounts to 0.2% per $^\circ\text{F}$ over the range 70°F to 120°F so that the additional 10% phase shift can compensate for a temperature range of 50°F . The phase setting accuracy lost through this increase in phase shift amounts to $\pm 5\%$ of the smallest bit (i. e., approximately $\pm 1^\circ$ of rf phase).

A total of 438 phase shifters were built and tested. Table 2-4 presents a statistical analysis of the results. The insertion phase of all

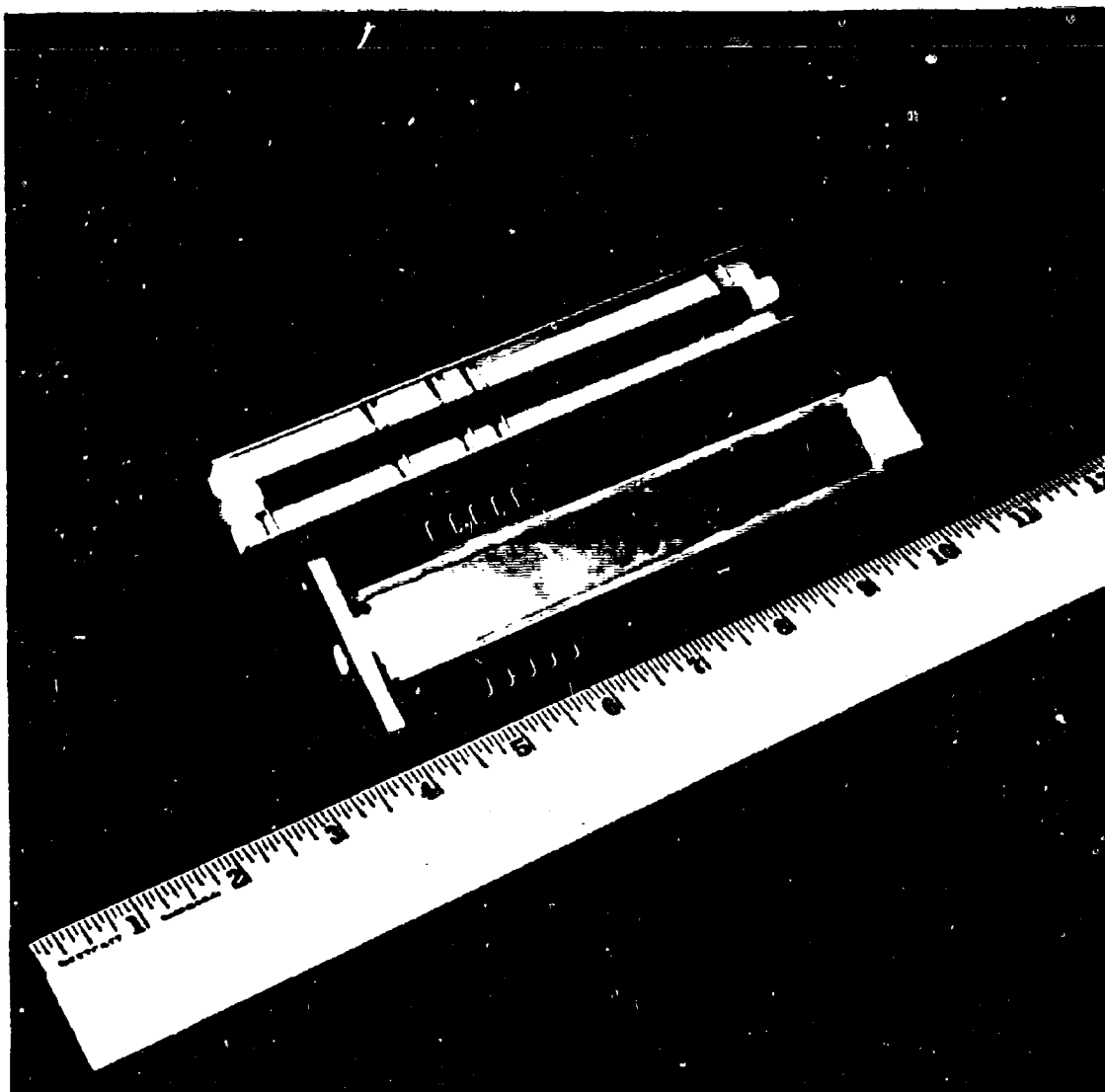


Fig. 2-44 Ferrite Phase Shifter

Table 2-3
Summary of Phase Shifter Characteristics

Operating Frequency	500 Mc /s bandwidth at C-band
Insertion Loss	3/4 db
VSWR	<1.25
Switching Current	4 amps
Peak Power	1.2 KW
Temperature Sensitivity of Differential Phase	0.2% per °F over range 70°F to 120°F
Differential Phase vs Frequency	3.5% increase over the 500 Mc /s band
Switching Time (four 180° bits in series)	6 μ sec
Switching Energy (one 180° bit)	80 μ joules
Weight of Phase Shifter	3 ounces
Cost of Components	\$36
Assembly Time	3 hr

Table 2-4
Statistics Concerning all Phase Shifters
Constructed for the Eight Subarrays

The following pertains to all phase shifters built:

Number Built	438
Number Rejected and Rebuilt	49
Number Rejected for:	
Insertion Loss	9
VSWR	15
Insertion Phase	25

The following pertains to those phase shifters used in
the eight subarrays:

Differential Phase:		RMS
Nominal Bit Size	Measured Average Value	Deviation from Average
22 $\frac{1}{2}$ °	26.40°	0.78°
45°	50.14°	1.15°
90°	102.31°	2.12°
180°	205.50°	3.37°
Total	337 $\frac{1}{2}$ °	4.21°

Insertion Phase:

Overall Phase Spread	52°
Phase Spread within Each Subarray after Selection (see text)	16°

the phase shifters used in the eight subarrays spreads over a range of 50° , however, the phase shifters were selected and assigned to subarrays so that within each subarray the spread in insertion phase was less than 16° . The resulting difference in insertion phase between subarrays was then corrected at each subarray input port.

2.4.2 Design

The C-band phase shifter consists of a ferrite assembly fixed in a modified X-band waveguide body, as shown in Fig. 2-45. Except for flat surfaces on opposite sides, the ferrite cylinders are circular in cross section with a small circular hole provided for the control wire. The circular geometry permits all of the ferrite to be magnetized to saturation with the smallest possible current. In production, the small center hole is extruded, resulting in relatively low machining costs. During development of the phase shifter it was convenient to machine the body from ordinary X-band aluminum waveguide. For production it was found that the same cross sectional geometry, complete with finished grooves, could be obtained as an aluminum extrusion at a cost of about 9 cents per foot.

Insertion loss, VSWR, insertion phase, and differential phase are all critically dependent on the quality of contact between the waveguide walls and the ferrite surfaces. Even a very small gap extending over only a short length of the assembly will cause spikes of insertion loss and VSWR at several frequencies in the operating band. Such gaps also result in sensitivity to mechanical pressure on the waveguide wall and in unpredictable insertion phase and differential phase. Good contact is achieved by using an aluminum waveguide which has one broad

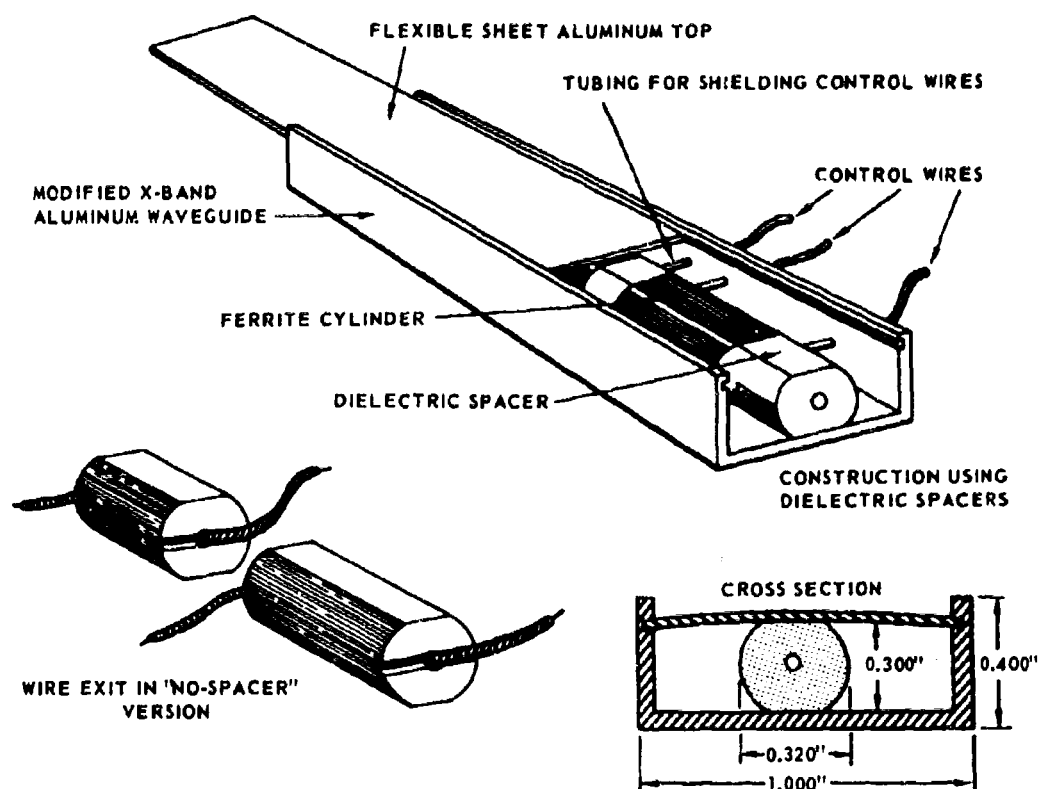


Fig. 2-45 Phase Shifter Construction Details

THE UNIVERSITY OF CHICAGO
DIVISION OF PHYSICS
RESEARCH REPORT
1964

wall replaced with a 0.025-inch flexible aluminum sheet. The height of the waveguide is 0.010 inch less than the height of the ferrite cylinder. In addition, the aluminum sheet is made from a hard temper aluminum and is preformed so that its transverse cross section is a section of a circle. In assembly of the phase shifter the aluminum top sheet is placed so that its convex surface faces the ferrite assembly. When snapped into place the top curves in the opposite direction and the resulting stresses maintain a constant 100 lb/in^2 pressure on the ferrite. In addition to providing good contact, this arrangement holds the ferrite assembly firmly in position.

In some cases microwave radiation from the control wires had caused variations in insertion phase, VSWR, and insertion loss. To correct for this, small diameter stainless steel tubing is placed over each of the control wires so that it extends from the ferrite surface through the wave guide wall where it is tightly fitted.

The use of dielectric spacers between ferrite bits was originally intended to provide a means of exit for the control wires and to prevent any possibility of interaction between the bits. The spacers have been eliminated and the ferrite bits bonded directly to one another. The control wires exit through small grooves cut across the ends of each ferrite bit (see Fig. 2-45). This has resulted in a phase shifter which is physically shorter, has simpler construction, and has lower VSWR due to fewer discontinuities. There were two possible sources of difficulty which were anticipated from this "no-spacer" construction. First, because of the close contact of adjacent bits, switching the latch state of one bit might have affected the magnetization of the adjacent bit, thus producing phase shift interaction. However, because of the low switching current used, this interaction was found to be less than ± 1

degree of rf phase. Further, grooves across the ends of the ferrite bits result in regions which are no longer closed magnetic paths and cannot retain magnetization after removal of the switching current pulse. It was expected that these unmagnetized regions might introduce high insertion loss and VSWR. Apparently, the grooves are sufficiently small so that no increase in insertion loss or VSWR is observed.

A two-step transformer was used to match the phase shifter into RG-50 waveguide. One of the steps is an integral part of the phase shifter and consists of a $\lambda/4$ dielectric cylinder. This section is similar in cross section to the ferrite cylinders and is made from Trans Tech's Forsterite, a magnesium silicate ceramic having a dielectric constant of 6.2. The second step is a $\lambda/4$ reduced height section of RG-50 waveguide external to the phase shifter. Prior to matching, this end of the phase shifter had a VSWR of 9.0 as seen from RG-50 waveguide. The two-step transformer reduced this to <1.08 over a 10% band as shown in Fig. 2-46.

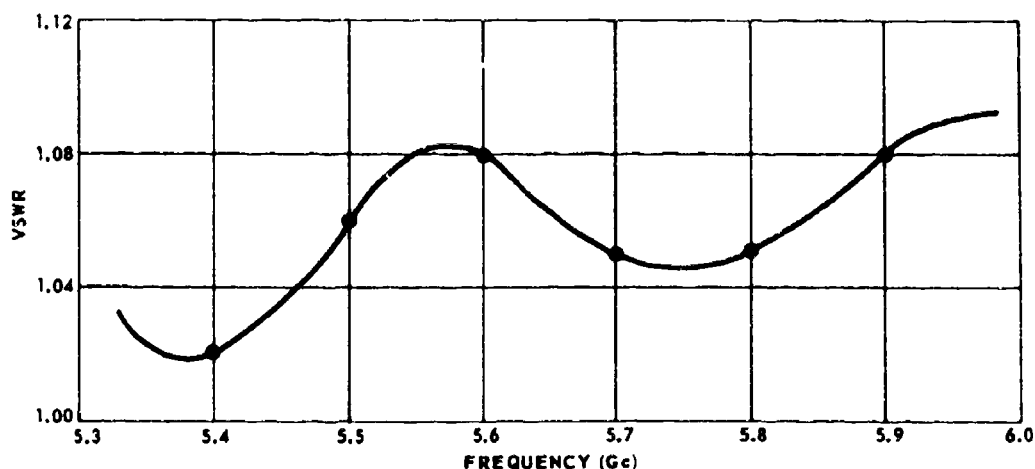


Fig. 2-46 VSWR of Power Divider End of Phase Shifter

Matching of the radiating end of the phase shifter was accomplished with the aid of a waveguide array simulator. This simulator consists simply of a rectangular waveguide. A single radiating element placed at one end of the waveguide will see an infinite series of images of itself reflected in the walls. If the cross sectional dimensions are properly adjusted, the series of images will have a spacing and arrangement identical to that of the actual array. The relative phasing of the images (and the effective array scan angle) is dependent on the waveguide dimensions, frequency, and particular waveguide mode being propagated. The simulator used for matching the phase shifter simulated a scan angle of 30° in the H-plane; it contained a section of the dielectric sheet intended for matching the array on scan (described in Section 2.2.3). The impedance matching configuration consisted of a $\lambda/4$ section of Pyrex having a cross section identical to that of the ferrite (except that the center hole was absent). This was inserted in the end of the phase shifter adjacent to the ferrite section. Most of the Pyrex section was within the phase shifter body, but it was found necessary for matching to have a small portion of the glass protruding outside the end of the phase shifter. As seen from the simulator this ferrite-Pyrex assembly produced a VSWR of about 4.0 which closely balanced the 4.0 VSWR produced by the scan matching dielectric sheet. The result for the simulated 30° H-plane scan angle was a VSWR < 1.18 across the 10% band for the radiating end of the phase shifter. This VSWR measurement is shown plotted in Fig. 2-47.

Careful measurements of phase shifter insertion loss were made using a substitution technique. The insertion loss of the phase shifter, exclusive of the array simulator, was determined to be 0.7 db, with a measurement uncertainty of 0.1 db. Within the 0.1 db measurement uncertainty, the insertion loss was independent of frequency in the 10% frequency band. These insertion loss measurements included the losses of the input and output transformers.

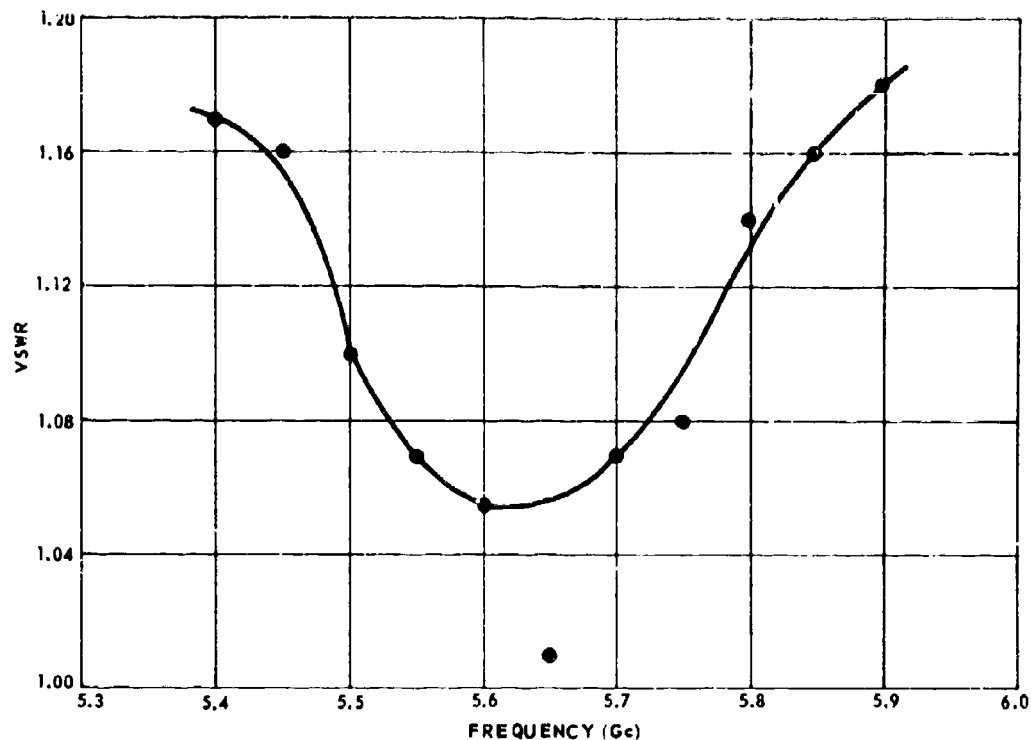


Fig. 2-47 VSWR of Radiating End of Phase Shifter in Array Simulator

Experience had shown that variations in remanent magnetization from batch-to-batch of the ferrite material were sufficient to cause small but significant variations in the length of ferrite section needed to produce a given amount of differential phase shift. The amount of ferrite the manufacturer could produce in one batch was limited. The amount of ferrite needed for the 440 phase shifters had to be made in three separate batches which were produced before any ferrite bits were machined. Sample bits from each batch were measured to determine the length needed for a given amount of phase shift. With this information the lengths were then specified with the 180° bits for all the

phase shifters coming from one batch, all the 90° bits from the second batch, and all the 45° and $22\frac{1}{2}^\circ$ bits from the third batch. This technique obtains the desired result that all the phase shifters are identical in physical and electrical length.

The phase shifters produced for this program used Trans Tech's TT1-109 Ferrite material. The use of Trans Tech's G-1001 Garnet material in the same geometry as the ferrite was also investigated. The results (Figs. 2-48, 2-49, and 2-50) show the G-1001 material to be superior in the phase shift versus temperature characteristic and in peak power handling capacity. However, the garnet requires more switching current and is more costly than the ferrite.

2.4.3 Measurements

All phase shifters were subjected to a testing program which included swept measurements of VSWR and insertion loss across the frequency band, and measurements of insertion phase and differential phase at band center. Since more than 400 phase shifters had to be tested, a measurement facility was constructed which allowed all the above measurements to be made rapidly without removing the phase shifter from the setup. A quick connect mechanism was provided to permit rapid insertion and removal of the phase shifter under test. A block diagram of the setup is shown in Fig. 2-51. As indicated in the diagram, the two arms of the phase bridge were identical. The lengths of the two arms were carefully equalized so that phase shift measurements were essentially independent of frequency.

The purpose of the swept measurements was to determine quickly whether the phase shifter was acceptable, unacceptable, or should be examined more closely. For this purpose a gross indication of VSWR

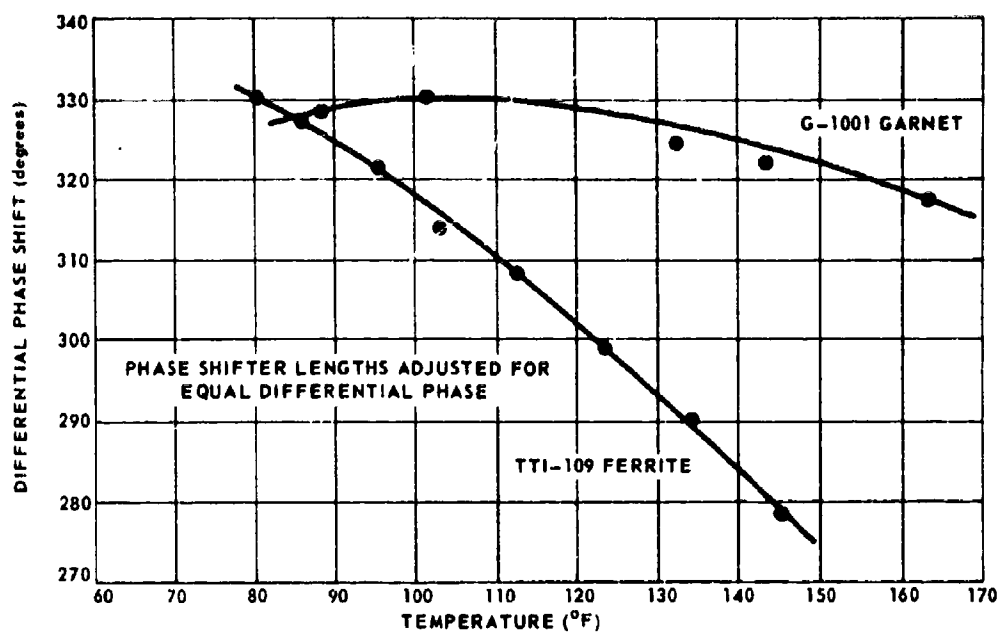


Fig. 2-48 Differential Phase Variation with Temperature

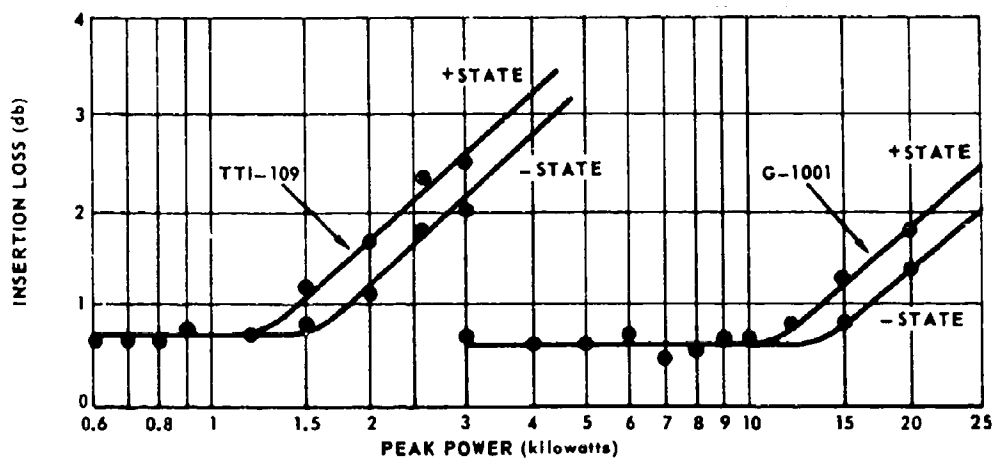


Fig. 2-49 Peak Power Handling Capacity of the Phase Shifter

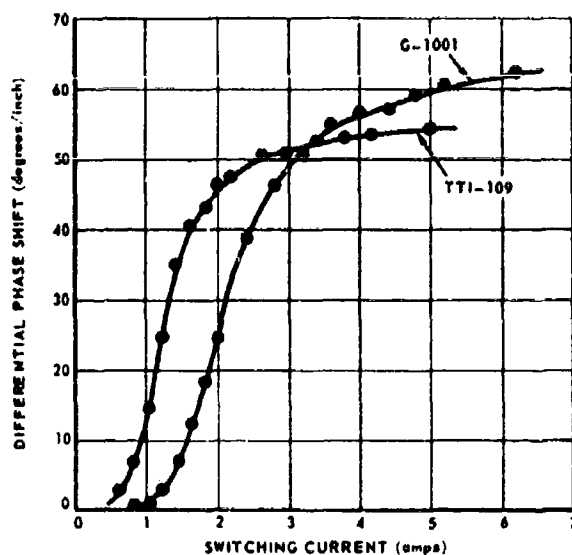


Fig. 2-50 Differential Phase Variation with Current

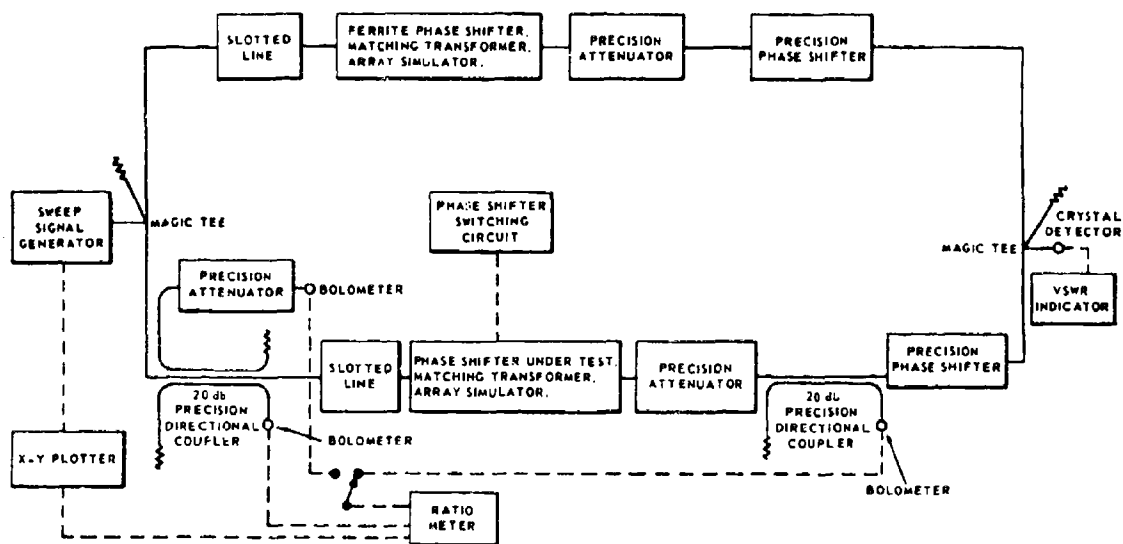


Fig. 2-51 Phase Shifter Test Setup, Block Diagram

and insertion loss as a function of frequency was all that was necessary. Specifically, a phase shifter was unacceptable if the data showed:

1. The presence of narrow "spikes" of insertion loss or VSWR which would indicate mechanical gaps between the ferrite and waveguide wall; or
2. Large deviation of the VSWR or insertion loss curves, in character or magnitude, from the established average behavior which would indicate either mechanical problems internal to the phase shifter or poor connection of the phase shifter flanges to the measurement setup.

A phase shifter was unacceptable if the data showed a VSWR >1.40 anywhere in the band. However, this was not an indication of the true VSWR of the phase shifter. Referring again to the block diagram (Fig. 2-51), the connection from the waveguide simulator to the RG-50 waveguide of the test equipment produced a VSWR of 1.15. The precision attenuator following this junction produced another 1.15 VSWR. These reflections made accurate measurements of the phase shifter VSWR impossible in this setup. There were similar problems associated with the swept insertion loss measurements. A phase shifter was acceptable if the loss was less than 1.2 db over the band. This includes the loss in the simulator (approximately 0.2 db) and any reflection loss. More precise measurements of VSWR and insertion loss showed considerably better performance.

The insertion phase measurement of each phase shifter was used for the selection and assignment of the phase shifter to a sub-array. This process was previously described in Section 2.4.1. The insertion phase data and the statistics of the differential phase data are presented in Table 2-4.

Complete details of the phase shifter assembly procedure are given in Ref. 7.

2.5 Driver Circuit

(J. H. Kuck)

2.5.1 Summary and Results

The driver circuit was designed to deliver 4-ampere current pulses of either polarity. These current pulses contain sufficient energy to switch four 180° bits, or eight 90° bits, etc. This may be used to advantage in an array of such subarrays where many of the elements always receive the same phase setting. By wiring similar bits of several phase shifters in series, one driver may be used to provide the energy to switch one bit in several phase shifters. During this program, the use of this technique resulted in a significant reduction in the number of drivers required and simplified the wiring considerably. For simplicity of wiring one driver was used to drive any of the following load conditions: (a) four 180° bits, (b) eight 90° bits, (c) eight 45° bits, or (d) eight 22½° bits.

On the average, one driver was required for every 1.6 phase shifters. Four drivers were wired on one printed circuit board and 60 such boards were required to drive all the phase shifters (384) in the array. A photograph of the driver board containing four drivers is shown in Fig. 2-52.

A driver box was designed to house the drivers. The driver box provides room for eight cards (32 drivers), and fits immediately behind the subarray. It contains all the necessary connections for the computer commands, monitoring, and power supplies. It also contains connectors into which the cards slide, thereby providing for quick replacement. A photograph of the driver box is shown in Fig. 2.53.

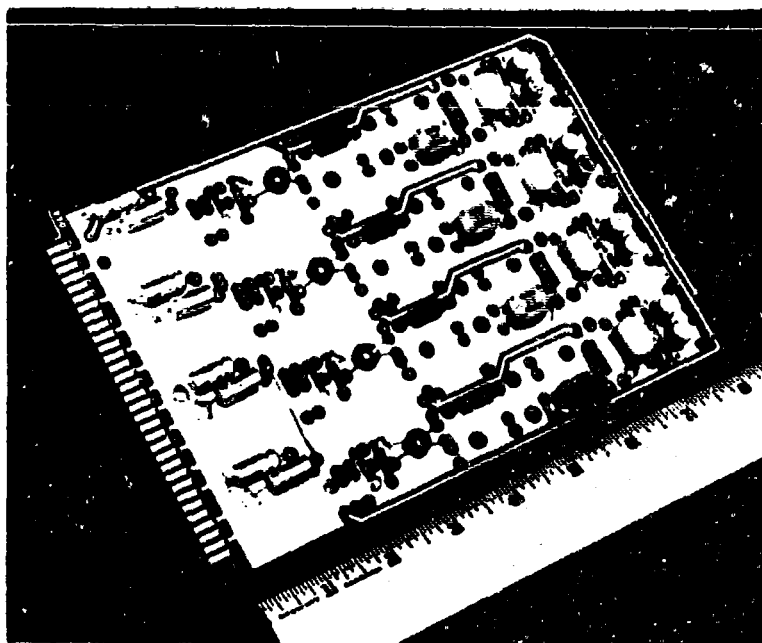


Fig. 2-52 Driver Board Containing Four Drivers

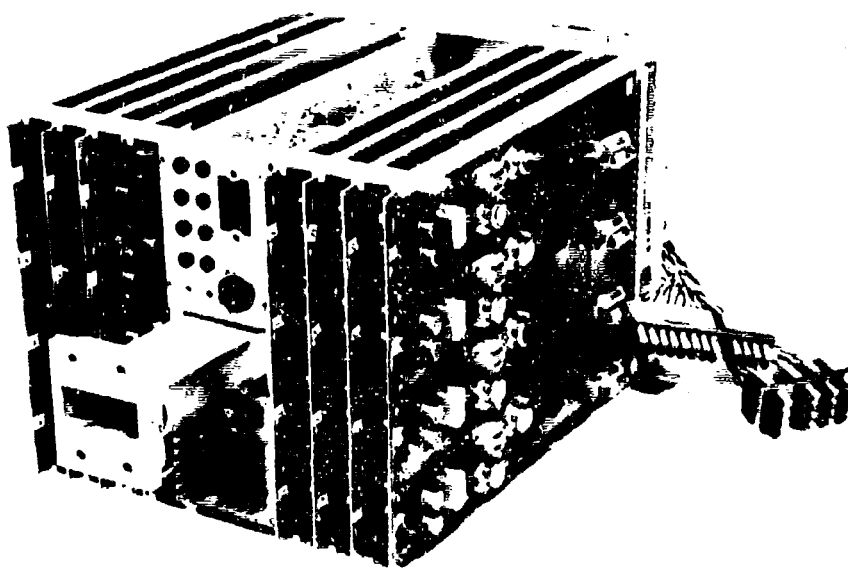


Fig. 2-53 Driver Box Housing Eight Driver Cards

The basic operation of the driver circuit is to connect either a positive or a negative 40-volt power supply to the output terminal. The switching operation is accomplished by means of two silicon NPN transistor switches (Transitron type ST-7708). Transistors were chosen after a comparison with SCR's indicated that transistors were less expensive and could be turned off more easily and more quickly.

The efficiency of the driver averages 60% and four 180° bits can be switched by one driver in 6 microseconds. The circuit has been operated at up to 5000 repetitions/sec (i. e., 10,000 switching operations/sec) with no deterioration of the pulses. The effects of temperature variations between 25°C and 100°C and power supply variations of 10% have also been examined. These variations cause a current change of less than 0.5 ampere resulting in a phase change of less than 2° in the 180° bit. Table 2-5 presents some of the driver characteristics.

2.5.2 Design

The driver circuit produces current pulses of either polarity in a single output conductor. This is accomplished by means of two transistor switches connected to power supplies of opposite polarity.

Figure 2-54 shows the driver circuit. Each driver board contains four of these circuits. In addition to the two switching transistors (Transitron ST-7708), each driver circuit contains two low-power transistor emitter-followers. By use of a complementary pair (2N1308 and 2N1309), a circuit arrangement is obtained by which input signals of opposite polarity can be brought in on a single input line to turn on either switch, as desired. This reduces the number of interconnections between the computer and the drivers by a

Table 2-5
Driver Characteristics

Efficiency	60%
Switching Time (4-180° bits in series)	6 μ sec
Max. switching operations tested	10,000/sec
Temperature Range	25°C. - 100°C
Permissible Power Supply Variations	10%
Total Power Consumption (of one driver at 2000 switching opera- tions/sec)	1.5 watts
Cost of Driver Components (per phase shifter)	\$14.00
Assembly Time (per phase shifter)	0.5 hr
Testing and Trouble Shooting Time (per phase shifter)	0.16 hr
Percent Failures of ST-7708 Switches	3%

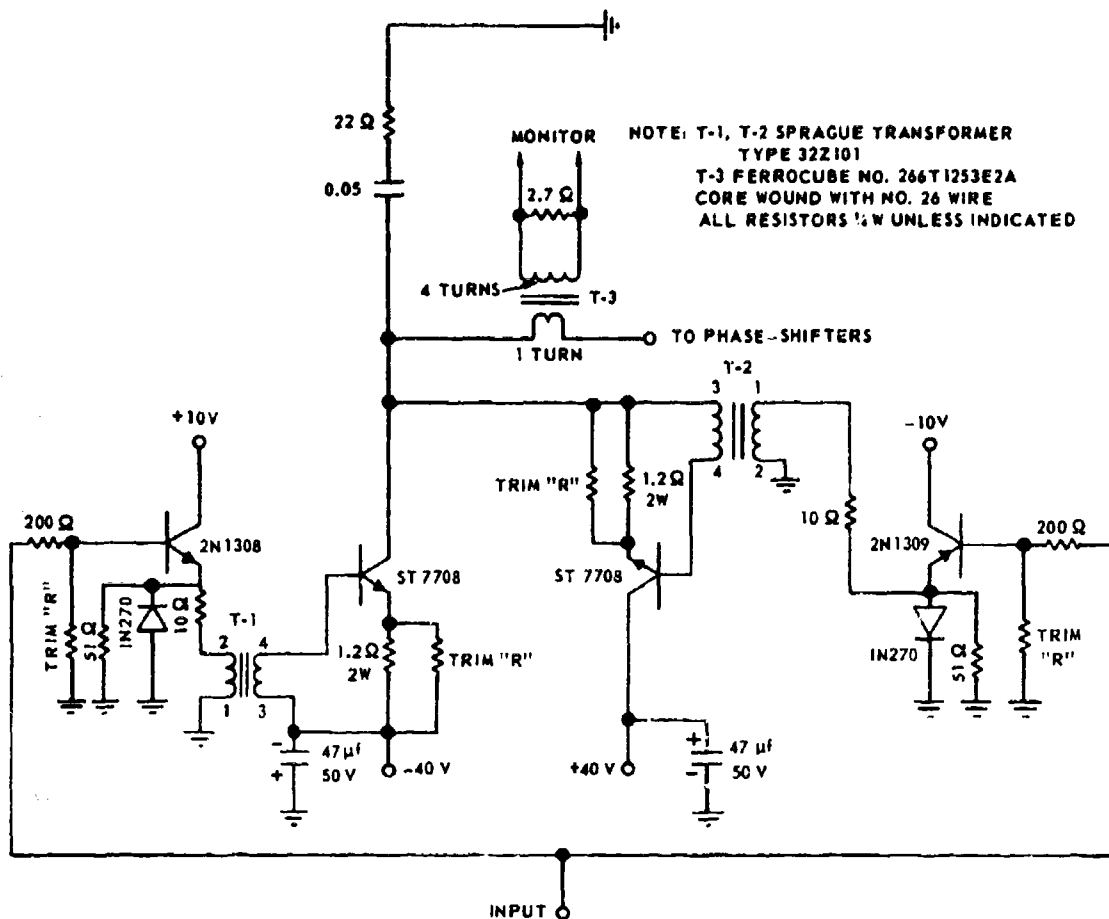


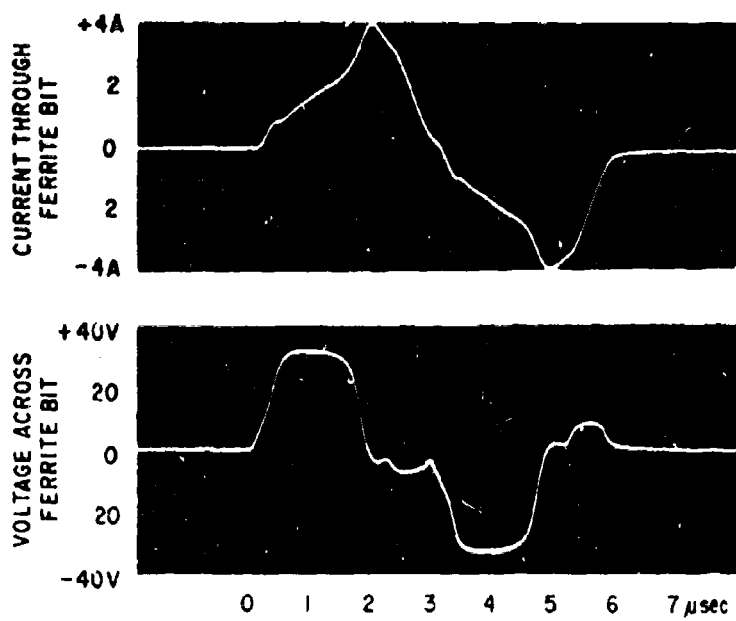
Fig. 2-54 Driver Circuit

factor of two compared with the alternative arrangement in which input pulses are brought in on two separate input wires.

Since the two power switches are identical NPN transistors, transformer coupling of the input pulse is required for one of these switches. The emitter of this switch is connected to the output of the driver circuit, requiring a floating secondary transformer winding so that the desired input pulse can be added to the fluctuating potential of the emitter. To preserve circuit symmetry and provide identical biasing arrangements, transformer coupling is used for the inputs to both switches.

When one of the switching transistors is turned on by an input pulse of the appropriate polarity, it connects a constant voltage power supply (40 volts) across the ferrite load. The resultant load current increase is approximately linear to two amperes, at which point the ferrite becomes nonlinear and the current increases much more rapidly. Some method of limiting the current is required. Negative feedback by means of a small emitter resistor was used since it yields high efficiency and fast switching. Two successive current pulses of opposite polarity are shown in Fig. 2-55.

During the time prior to ferrite saturation, the collector voltage of the switching transistor is very low, the voltage being dropped across the ferrite. During this period, stored charge is accumulated in the transistor. When the ferrite saturates, the voltage drop across it suddenly disappears and the collector voltage rises. As a result the stored charge is released, causing a large current to flow. There is thus a time delay before the feedback caused by the emitter resistor can take effect. This time delay is the "storage time" effect, which results from the release of the stored charge accumulated in the transistor.



In this circuit, the stored charge is actually beneficial in that it results in a higher peak current with a lower voltage drop in the switch than might otherwise be obtained. Note in Fig. 2-55 that the peak current is about twice as high as the final value at which the current is stabilized by the feedback just before the pulse is terminated.

A small current transformer, T-3, is in series with the output of the driver and is useful for monitoring the performance of the driver. (Other monitoring schemes are discussed in Ref. 8 wherein diode logic circuits would be built onto the driver boards in order to reduce the number of connections required between the drivers and the centrally located monitor console that would be needed for an operational system.) Additional information on the driver circuit may be found in Ref. 9.

2.5.3 Overall Characteristics of the Driver

During production, a change was made in the driver circuit in the hopes of improving its reliability, i. e., the two 51-ohm load resistors were added on the emitters of the 2N1308 and 2N1309 transistors. This change was instituted in an effort to reduce failures of the ST-7708 transistor switches. Prior to the change, it was found that when one transistor switch was turned on, some narrow positive voltage spikes of the order of 0.7 volt appeared on the base of the other switch. Since these voltage spikes bring the base voltage of the off transistor closer to the turn-on threshold level, it was reasoned that these spikes might reduce the breakdown voltage of the off-switch and cause a higher probability of failure.

The statistical evidence appears to indicate that the addition of the 51-ohm resistors plus 100% factory tests by Transistron have reduced the failure rate of the transistors by a factor of three to a failure rate of 3%.

2.5.4 Cost of Drivers for Eight Subarray Antenna

Sixty-six driver boards were constructed. Each board contained four driver circuits. The total cost per board of components, including the recurring cost for the driver board, was \$89.06. This cost does not include the cost of assembling the components onto the board or testing and trimming some resistors to obtain the specified output current. The assembly time was three operator hours per board. Testing and trimming required about 18 operator minutes, if the board was not defective. Some defective boards required several hours for trouble shooting.

With the present method of interconnection of subarrays, 30 driver boards are required for four subarrays having 192 phase shifters. In other words, there are 6.4 phase shifters per driver board.

The driver costs, on a per phase shifter basis, are obtained by dividing the aforementioned figures by the factor 6.4. Table 2-6 gives a cost breakdown, which is summarized here.

Cost of Components (per phase shifter)	\$13.90
Time for Assembly (per phase shifter)	0.5 hr
Estimated Time for Testing and Trouble Shooting (per phase shifter)	0.16 hr

Table 2-6
Cost of Components for Four Driver Boards

Component	Unit Cost	No. per Board	Cost per Board
Resistor 200 ohm 5%, 1/4W	0.045	8	0.360
Resistor 51 ohm 5%, 1/4W	0.037	8	0.296
Resistor 10 ohm 5%, 1/4W	0.045	8	0.360
Resistor 22 ohm 5%, 1/4W	0.085	4	0.340
Resistor 2.7 ohm 5%, 1/2W	0.0275	4	0.110
Resistor 1.2 ohm 5%, 2W	0.076	8	0.608
Transistor 2N1308	0.54	4	2.16
Transistor 2N1309	0.54	4	2.16
Transistor ST7708	4.40	8	35.20
Diode IN270	0.24	8	1.92
Sprague Cap. Type 109D 47uf 50V	1.90	8	15.20
Cap. Disc. 0.05uf 50V	0.087	4	0.348
Transformer Sprague 1:1 #32Z101	2.805	8	22.440
Cores Ferroxcube #266T1883F2A	0.34	4	1.36
Total			\$82.862
Printed Circuit Card (recurrent cost only)*			6.20
Total Component Cost per Board			89.062
Total Cost per Driver			22.266
Total Component Cost per Phase Shifter			13.90

* Note: There was a non-recurring charge of \$443.00

2.6 Wiring

2.6.1 Summary

The problem of wiring a phased array antenna is far from trivial. Simply stated, the experimental array of only 384 phase shifters requires 1536 inputs to provide 4-bit commands to each phase shifter. To prevent radiation and coupling between lines, twisted pairs or shielded cables are required so that the total number of lines is twice the number of inputs, 3072. Since each of these lines must pass through a connector to permit disassembly of the array, the same number of connector terminals is required. For this program, an additional requirement was the rearrangement of subarrays into several configurations for experimental studies.

A considerable amount of time was spent investigating different types of wire and wiring schemes with the following considerations in mind:

1. Cost and complexity.
2. Loss and inductance of a cable which runs 18 feet due to phase shifters in adjacent subarrays being wired in series.
3. Radiation from many lines, each of which is carrying a narrow current pulse of several amperes.
4. Coupling between adjacent lines.
5. Space requirements with emphasis on room for cooling air to flow freely through the array.

To meet these requirements, several types of cable were tested in the laboratory. For use within a subarray, a flat ribbon cable was developed. Each cable contained four signal-carrying lines and a ground return. The ground return consists of two copper foil shields, pressed together between the signal carrying lines to minimize the coupling between these lines. The four lines were used to carry the required current pulses from the subarray input connector to the four bits of a phase shifter. The signal out of the phase shifter is carried by a similar ribbon cable to a second phase shifter located at the diametrically opposite location in the subarray. Here the connections are made to allow each current pulse to travel through the phase shifter in a direction opposite to that in the first phase shifter. The output line from the second phase shifter is wired to the subarray output connector. In this manner, the symmetry properties of the subarray are utilized to reduce the number of computations and the number of input-output connections by a factor of two. A photograph of the internal subarray wiring is shown in Fig. 2-56.

For external connections from the drivers to the subarrays and for connections between subarrays, a less expensive cable was used. This cable consisted of four twisted pairs embedded in an insulating plastic. A photograph of the external wiring is shown in Fig. 2-57. This wiring provided the means by which one driver may drive four 180° bits (or $8\text{-}90^\circ$ bits or $8\text{-}45^\circ$ bits or $8\text{-}22\frac{1}{2}^\circ$ bits) in series.

Table 2-7 presents some of the characteristics of the cable. Additional details on wiring may be found in Ref. 10.

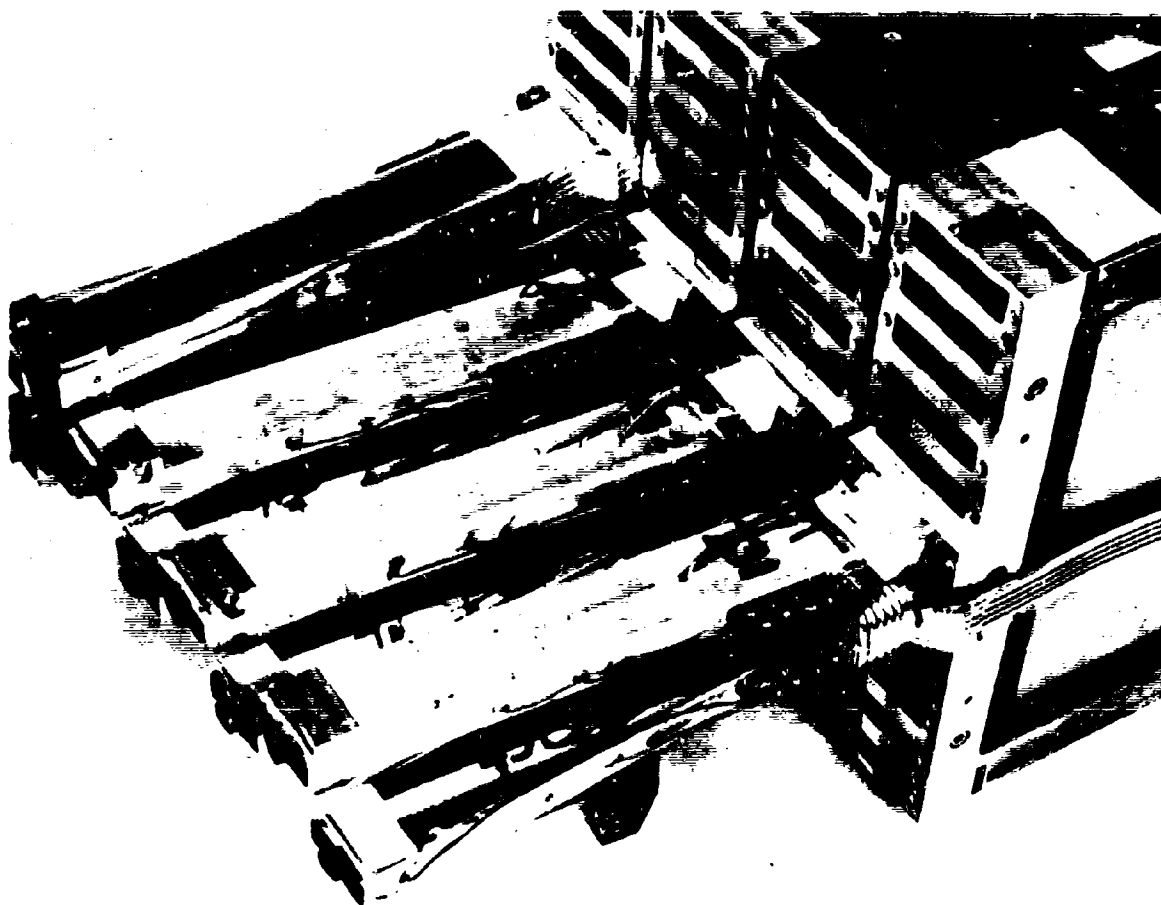


Fig. 2-56 Internal Subarray Wiring

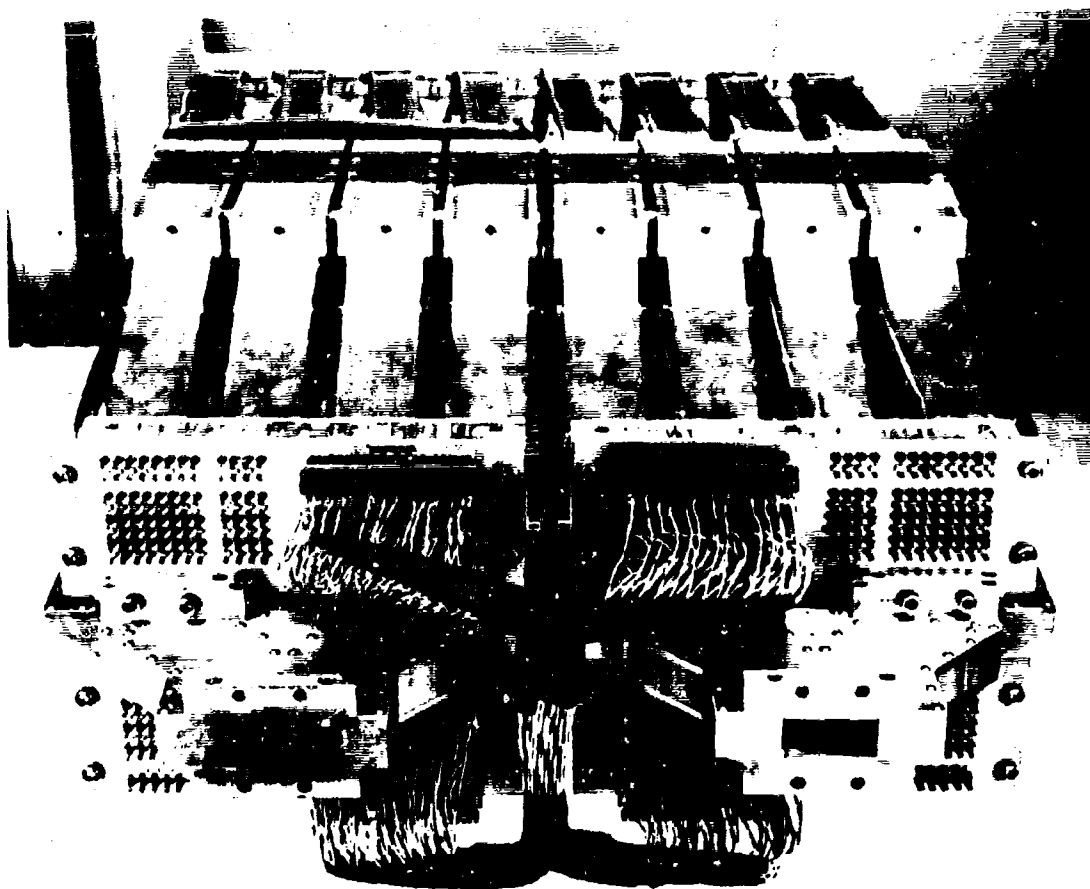


Fig. 2-57 External Subarray Wiring

Table 2-7
Wire Characteristics

Internal Wiring

Type	4 conductor shielded ribbon
Wire Size	AWG #26
Insulation	Teflon
Wire Spacing	0.1 inch on centers
Shield	Mylar insulated copper foil
Cost (1000 ft)	\$1170
Manufacturer	Gore

External Wiring

Type	4 twisted pairs in a ribbon
Wire Size	AWG #24
Insulation	Mylar
Cost (1000 ft)	\$490
Manufacturer	Gore

2.6.2 Wiring Techniques

Preparation of the shielded ribbon cables for the internal wiring of the subarray presented some special problems. To solve these problems, the following techniques were developed:

1. The copper foil shield had a tendency to rip as it was peeled away from the center conductors. To prevent this, the ends of the ribbon were heated with a heat gun. As the ribbon was heated, the bond between the shield and the wires was weakened. The shield was then easily peeled away from the wires.
2. For connecting to the mylar coated copper shield, it was found that reliable connections could be made by soldering right through the mylar coating.
3. To produce many cables rapidly and accurately, a set of patterns was used. The ribbon cables were placed directly on the patterns for cutting, stripping, and preparation of the foil ends.
4. The shielded ribbon, containing four wires, bends easily in only one plane. To provide a small-angle bend, which was required in the other plane, a "wrinkling" fixture was designed. This fixture will set a tapered wrinkle into the ribbon causing the ribbon to bend in its own plane by a predetermined amount.

Section 3 PHASE II--ARRAY PERFORMANCE

3.1 Summary of Phase II

Concurrent with the construction of the subarrays, a room was prepared for the necessary antenna measurements of Phase II. One wall of the room was constructed of solid polystyrene foam, transparent to microwave frequencies. The antenna radiates through the foam wall to a horn located on a tower 350 feet distant. Photographs of the facility, the array, and the microwave-measuring apparatus are shown in Fig. 3-1.

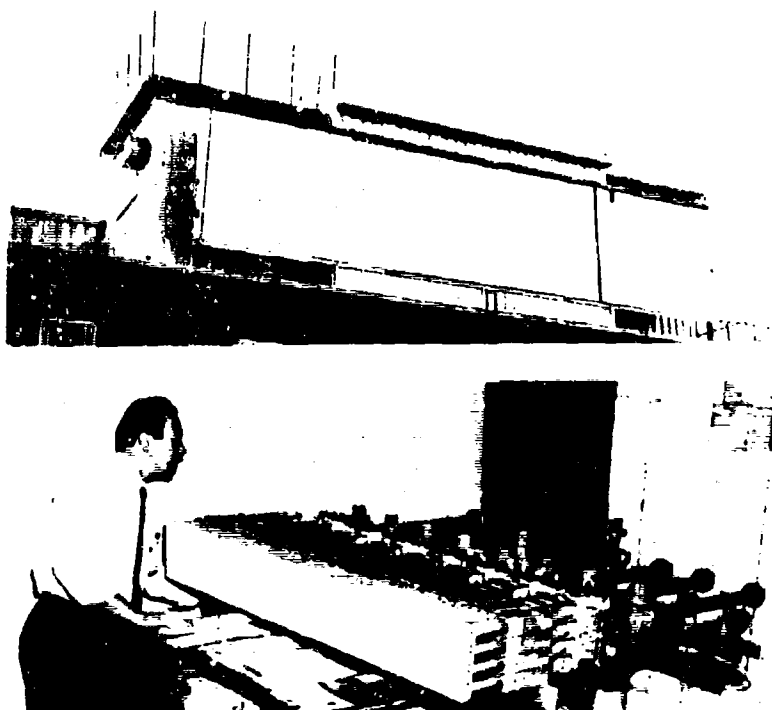


Fig. 3-1 Antenna Measurements Facility

Measurements were taken with the subarrays arranged in three different configurations (Fig. 3-2):

The performance measured in these geometries was considered typical of the performance of a full array. Since an array of subarrays is easily adapted for optimal sum and difference patterns, tapered sum and difference illuminations were investigated in addition to uniform illumination. In particular, the large number of measurements performed were designed to discover any anomalous behavior on the part of the array. None was discovered.

In the text to follow, the pertinent measurements of performance (Gain, VSWR, Beam Pointing Accuracy, and Patterns) will be discussed and the detailed results presented. The introduction preceding each topic is designed to define the quantities used in reporting the data, and to point out the interrelation between the parameters measured. For example, a gain measurement is more meaningful when the reflected power and the power radiated into quantization lobes are also measured and taken into account. This has been done, and it will be seen that the array performs in a predictable manner.

In addition to the original measurements program, this report contains results obtained in an extension program. This program began in November 1966 with the completion of the original program and is still in progress. Additional information will be reported in future documentation.

The results to date are summarized briefly below and detailed in the sections to follow:

1. The gain of a uniformly illuminated array of eight subarrays was measured at boresight and found to be 30.1 db. This compares with a maximum theoretical gain $(\frac{4\pi A}{\lambda^2})$ of 31.4 db for a lossless antenna. The loss of 1.3 db indicates an overall efficiency of 74% at boresight.

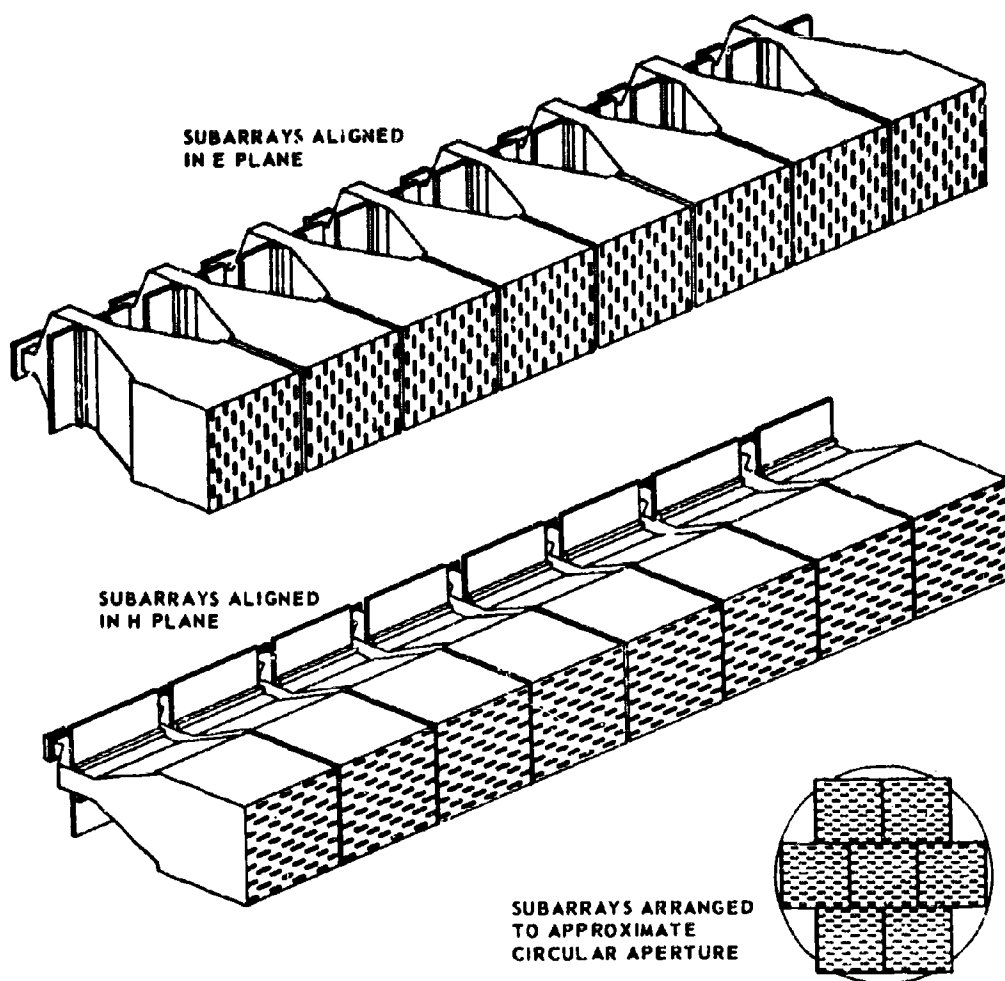


Fig. 3-2 Array Configurations

2. The VSWR of a subarray immersed in an array of radiating subarrays was measured at scan angles up to 60° for the three array configurations. The peak value of VSWR measured was 2.1. Correcting for losses in the subarray, this value corresponds to a VSWR of 2.6. Under most conditions of operation, the VSWR was significantly less.
3. The maximum absolute pointing error of the array was measured to be $\frac{1}{50}$ beamwidth (\approx milliradian). The rms pointing error was $\frac{1}{100}$ beamwidth. The pointing errors were too small to permit an accounting for the source of the errors.
4. A large number of antenna patterns were taken. These patterns indicate good predictable performance in all modes of operation. No evidence of "lost beams" (a surface wave phenomenon) was ever encountered. Figure 3-3 shows the near theoretical boresight pattern for subarrays aligned in the H plane with the $\frac{\sin x}{x}$ theoretical envelope superimposed.

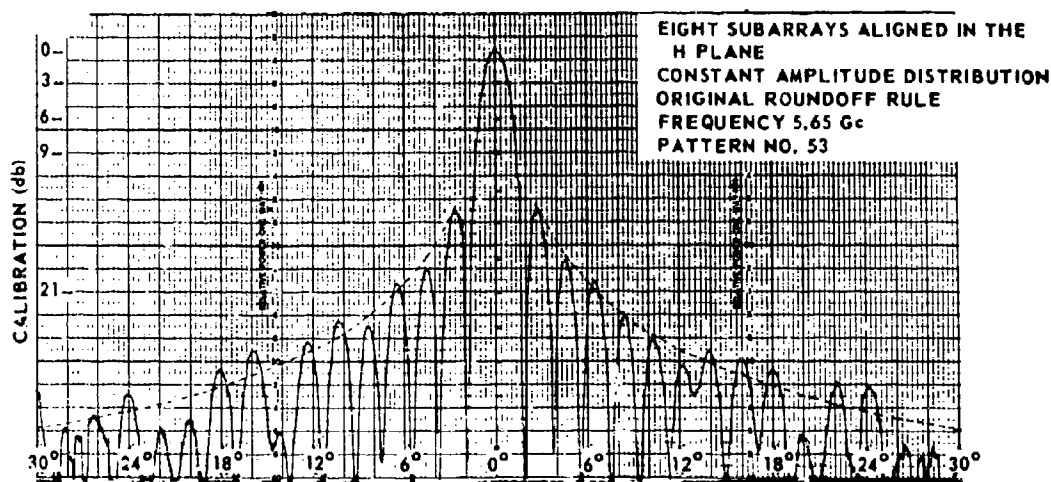


Fig. 3-3 Boresight Pattern Compared with Theoretical $\left(\frac{\sin x}{x}\right)$ Envelope

3.2 Gain and Efficiency

3.2.1 Introduction

The maximum theoretical gain of an antenna whose aperture is significantly larger than λ^2 is given by

$$G_d(\text{max.}) = \frac{4\pi A}{\lambda^2}$$

A = area

λ = free space wavelength

$G_d(\text{max.})$ = Maximum directive gain.

From physical considerations of the projected aperture, the maximum gain at any scan angle θ from boresight will be

$$G_d(\text{max.}) = \frac{4\pi A}{\lambda^2} \cos \theta .$$

When the amplitude and phase variations across the antenna are introduced, the directive gain becomes

$$G_d = \eta G_d(\text{max.})$$

G_d = directive gain

where η is referred to as the tapering efficiency, a measure of the power radiated into directions other than the direction of scan.

$$G_d = \eta \frac{4\pi A}{\lambda^2} \cos \theta .$$

This expression gives a good indication of the gain of the aperture as compared to the average radiation intensity. However, it does not take into account the losses (dissipative or reflective) inherent in most antennas. The realized gain (G_r) of the antenna may be expressed

as $G_r = \frac{\text{maximum radiation intensity of antenna being tested}}{\text{radiation intensity of a lossless isotrope with same input power}}$

The relationship between G_r and G_d is given by

$$G_r = G_d - L - |\Gamma|^2 \quad \begin{array}{l} L = \text{dissipative losses (db)} \\ |\Gamma|^2 = \text{reflective losses (db)} \end{array}$$

Another measure of antenna efficiency may be written as

$$\rho = \frac{G_r}{G_d} = 1 - L - |\Gamma|^2 \quad \begin{array}{l} L = \text{fractional dissipative loss} \\ |\Gamma|^2 = \text{fractional reflective loss} \end{array}$$

We may define ρ as the ratio of radiated power to the power available. A realistic estimate of the efficiency of the antenna is the product of the two previous efficiencies,

$$\text{Efficiency} = \rho \eta.$$

This definition compares the realized gain (G_r) to the maximum theoretical gain of a lossless antenna, $G_d(\text{max.})$, so that

$$\text{Efficiency} = \frac{G_r}{G_d(\text{max.})}.$$

With an array of subarrays, it is expected that the gain of the array will be the gain of a subarray multiplied by the number of subarrays in the array. A deviation from this would indicate that mutual coupling between subarrays had caused a change in the reflections, and perhaps a misphasing of the radiating elements. In the array under consideration, effects of mutual coupling on reflections are readily observed by VSWR measurements. These measurements are reported in Section 3.3. To observe the effects of coupling on amplitude and phase variations across the array, it is convenient to measure the gain and add to it the power lost due to reflections. Then, the corrected gain is defined as

$$G_{\text{cor}} = G_r + |\Gamma|^2 = G_d - L \quad G_{\text{cor}} = \text{corrected gain.}$$

Since the ohmic losses in the subarrays should remain constant with scan angle, the variation of G_{cor} with scan should theoretically follow $\cos \theta$ as the array is scanned. Deviations from $\cos \theta$ are attributed to phase or amplitude variations. In the following sections, it will be seen that all gain deviations from $\cos \theta$ are small and can be traced to power in grating lobes, a consequence of known phase periodicities inherent in the array caused by quantized phase commands and an amplitude taper across the E plane horn.

3.2.2 Results of Gain Measurements

Many gain measurements were taken to determine the gain variations with plane of scan, scan angle, frequency, and amplitude taper. The results are consistent and close to theoretical expectations. These results have been plotted in a series of graphs, Figs. 3-4, 3-5, and 3-6. All of these graphs have been corrected for VSWR so that the plotted gain is higher than measured, by an amount equal to the reflection loss. This was done to separate the effects of VSWR from the power radiated in undesired directions as discussed in the previous section. The VSWR variation with scan angle is discussed in detail in Section 3.3. It is noted here that the loss due to reflections was never greater than 1.0 db and this loss was observed only at 60° scan in the H plane.

Calculated Gain--To obtain a measure of the efficiency, the maximum gain of a lossless uniformly illuminated array is computed for the array of eight subarrays under investigation,

$$G_d(\text{max.}) = \frac{4\pi A_s}{\lambda^2} \times 8$$

$A_s = 7.5 \text{ inches} \times 8 \text{ inches}$
(Subarray area)

$\lambda = 2.09 \text{ inches}$

$$G_d(\text{max.}) = 31.4 \text{ db.}$$

Next the assumed dissipative losses are noted

phase shifter	3/4	db
power divider	1/4	db
total dissipative	1	db

then

$$G_{\text{cor}} = G_d - L = 30.4 \text{ db.}$$

This is the gain that would be expected, assuming perfect phasing and constant amplitude across the array. For an amplitude taper which approximates $1 + \cos \frac{\pi x}{a}$, the calculated G_{cor} is

$$G_{\text{cor}} = G_d(\text{max.}) - L = 30.2 \text{ db.}$$

Measured Gain--Absolute gain measurements were taken at boresight for both planes of scan with uniform and tapered distributions. Measured values of gain fell between 0.15 db and 0.5 db lower than those computed above. Assuming an average case of 0.3 db added loss, the total of all losses (dissipative, misphasing, amplitude errors, and reflections) is 1.3 db. This represents an overall efficiency of 74%,

$$\text{Efficiency} = \rho\eta = 0.74.$$

As the antenna is scanned away from boresight, the reflection loss generally increases, and the efficiency is reduced. A further reduction is caused by misphasing of the subarray elements (due to quantized phase shifting) and the resulting quantization lobes. The variation of corrected gain with scan has been plotted for each plane of scan for both uniform and $1 + \cos \frac{\pi x}{a}$ amplitude distributions; the effects of quantization lobes on corrected gain are readily observed in these graphs.

Figure 3-4 shows the H plane gain variation for a uniformly illuminated aperture at three frequencies. At 5.65 Gc, the gain falls very close to $\cos \theta$. At both the higher and lower frequencies, the gain falls off more rapidly. This is caused by an increase in the quantization lobes at both the high and low ends of the band (see Section 3.4).

Figure 3-5 shows the gain variation in the E plane for uniform illumination. In this case, the quantization lobe is most severe at the low end of the frequency band with a resultant decrease in gain at 60° scan.

Figure 3-6 shows the gain variation with scan for a tapered illumination at 5.65 Gc. It is seen that in both E and H planes, the gain variation follows $\cos \theta$. Quantization lobes have little effect on the gain since the quantized phase settings for 60° scan at 5.65 Gc are quite close to the calculated values. It will be noticed that in the E plane relative, rather than absolute, gain measurements were performed.

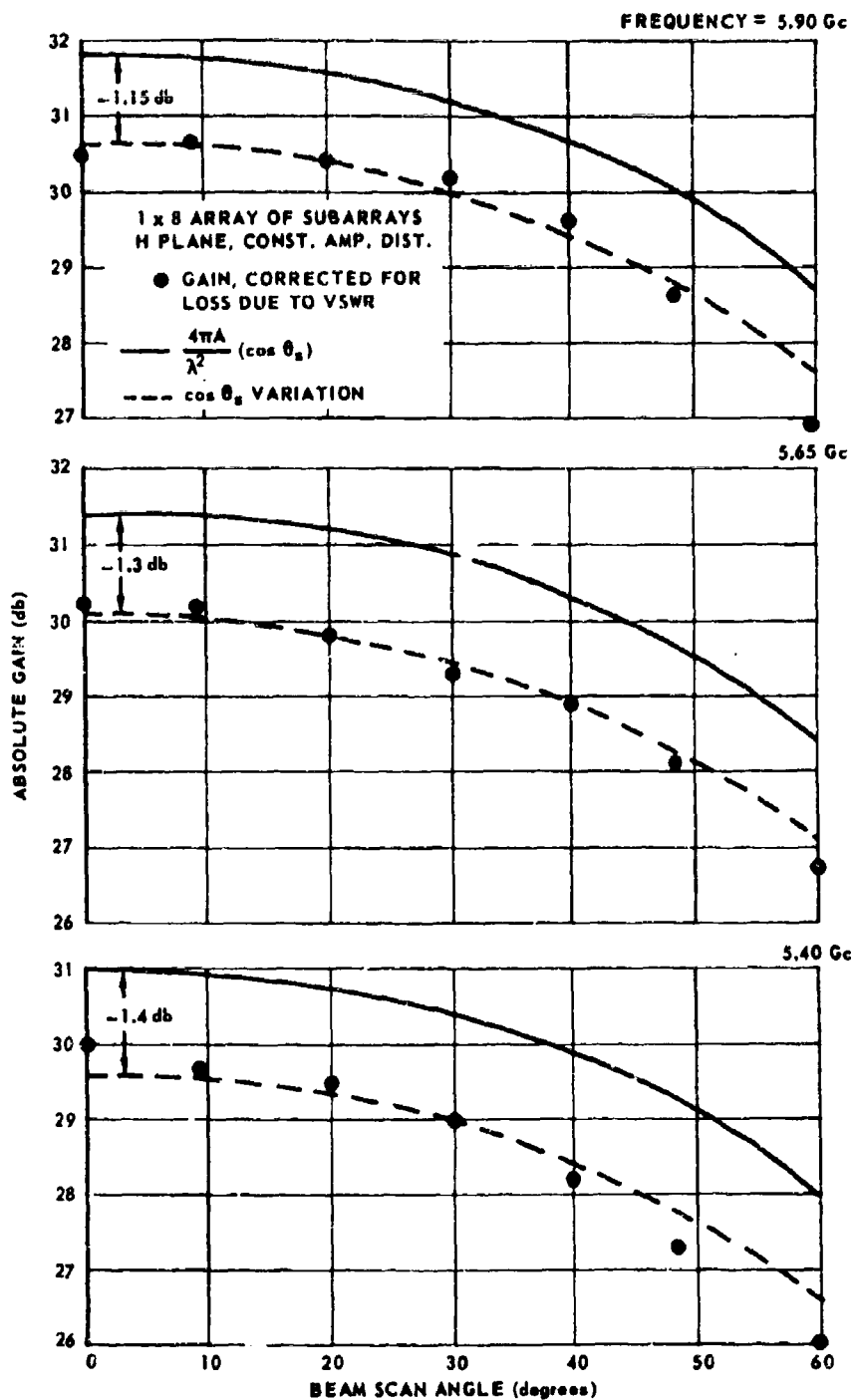


Fig. 3-4 H Plane Gain Variation vs. Scan Angle

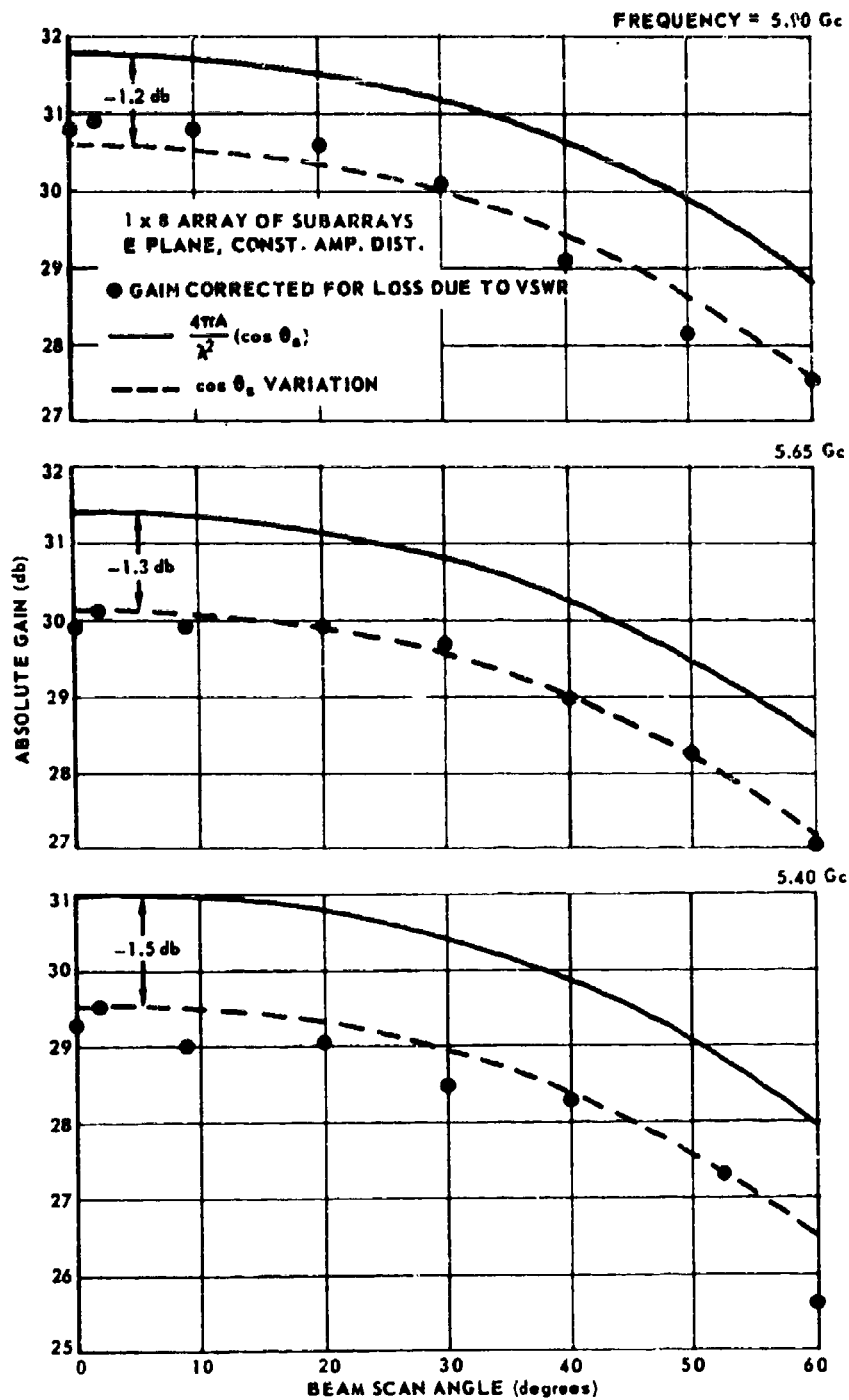


Fig. 3-5 E Plane Gain Variation vs. Scan Angle

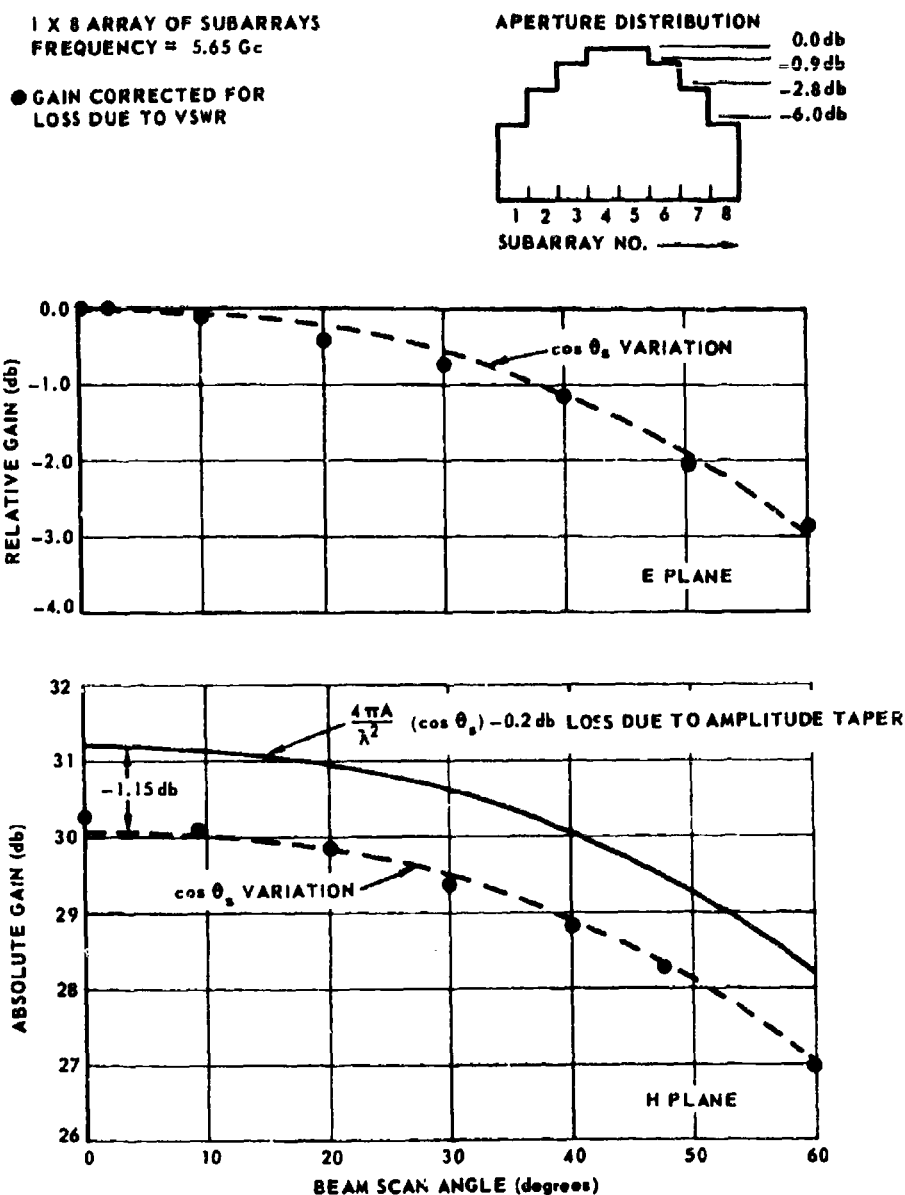


Fig. 3-6 Gain Variation vs. Scan Angle, Tapered Amplitude Distribution

3.3 VSWR

3.3.1 Introduction

During the past few years, the topic of mutual coupling and its effects on VSWR have been studied in detail (Refs. 11 and 12). Although these studies are not conclusive, several effects may be predicted. In particular, it has been shown that the variation of VSWR with scan angle is decreased as the element spacing is decreased. This, in spite of the fact that the mutual coupling is increased. The limiting case of close spacing is a continuous aperture and for this case, the variation with scanning is given by

$$\frac{R}{R_o} = \frac{\cos \theta}{1 - \sin^2 \theta \cos^2 \phi}$$

θ = angle of scan from boresight
 ϕ = angle in plane of array
 R = resistance of free space
 R_o = resistance of radiator .

For the scanning in the E and H planes, the expression is reduced to

$$\begin{array}{ll} \text{E plane, } \phi = \frac{\pi}{2} & \frac{R}{R_o} = \cos \theta \\ \text{H plane, } \phi = 0 & \frac{R}{R_o} = 1 / \cos \theta . \end{array}$$

These are believed to be limiting values for an array of radiators, and the reported results of many investigators show VSWR variations significantly greater than $\cos \theta$ as the array is scanned. Wheeler Labs has suggested several methods for scan compensation (Refs. 4 and 13), and theoretically it is possible to have the array matched for all angles

of scan. During the course of this program, some scan compensation was achieved through the use of a dielectric sheet. The matching procedure is summarized in Section 2.2.

3.3.2 Results of VSWR Measurements

During Phase I, the variation of VSWR with scan angle of a single subarray was measured. The results are reported in Section 2.2. It was of interest to determine whether the VSWR characteristics of a subarray were altered when the subarray was immersed in the midst of an array of radiating subarrays. Any variation in VSWR would be taken to be caused by mutual coupling, and thus provide insight to the magnitude of the subarray to subarray coupling. As seen from the following results, the subarray to subarray coupling is quite small. Upon examining the data, it should be noted that in every case, an isolated subarray is compared to the same subarray while immersed in the array of radiating subarrays. However, for each array configuration, a different subarray was used for the comparison. Three array geometries were investigated: eight subarrays aligned in the E plane, eight subarrays aligned in the H plane, and seven subarrays arranged to approximate a circular aperture. As expected, the circular approximation exhibited the greatest variation in VSWR, since the surrounding subarrays are located more closely than in the other cases.

Two types of measurements were taken; at boresight swept measurements were taken over the 10% band of interest; off boresight measurements were taken at three frequencies.

Swept Measurements--When the array is phased for boresight, the beam direction is insensitive to a change of frequency. For this phasing, swept VSWR measurements were performed on a subarray immersed in an array with the subarrays aligned first in the H plane and then in the E plane. In Figs. 3-7 and 3-8, results of these measurements are compared to measurements on the same subarray when isolated. The largest effect of coupling is seen to occur at 5.4 Gc in the H plane where the measured VSWR changes from 1.8 to 2.07 corresponding to a coupling of -22.5 db.

Scanned Measurements--Since the direction of the scanned beam varies with frequency, scanned VSWR measurements were performed at spot frequencies. At each frequency, the beam was scanned in 10° increments and the VSWR was recorded. This procedure was followed for the three array configurations.

Figures 3-9 and 3-10 compare the VSWR of an immersed subarray to that of an isolated subarray for E and H plane scan. For these cases, the largest coupling effect is observed at 60° H plane scan at the low end of the band. The difference in VSWR's (immersed to isolated) corresponds to -16.8 db of coupling. Note that in the E plane, at 5.4 Gc, the VSWR decreases with scan. This is caused by the initial mismatch at boresight being cancelled by the increased reflection from the aperture of the array.

Figure 3-11 compares the VSWR of the central subarray immersed in an array which approximates a circular aperture to the VSWR of the same subarray when isolated. For this configuration, scanning in the 45° plane was performed in addition to E and H plane scanning. The coupling for the 45° plane is seen to be slightly less than for the E plane. In the E plane, the coupling peaks at -15.4 db for 60° of scan.

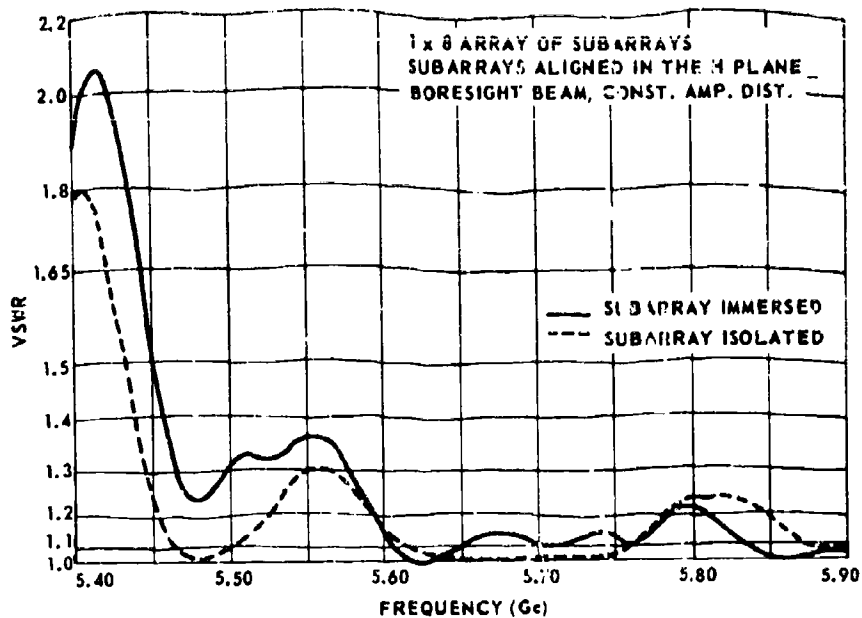


Fig. 3-7 Swept VSWR Comparison of Isolated and Immersed Subarray, Subarrays Aligned in H Plane

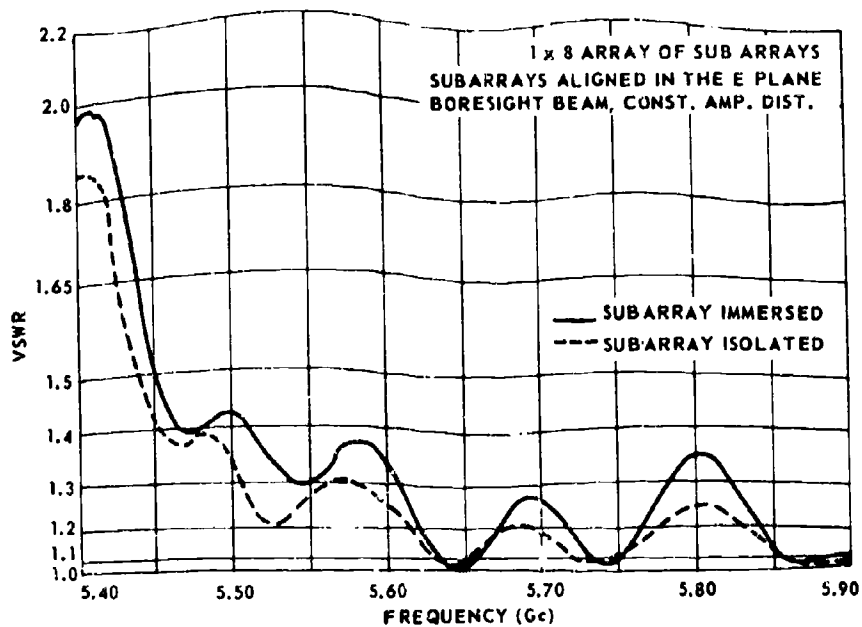


Fig. 3-8 Swept VSWR Comparison of Isolated and Immersed Subarray, Subarrays Aligned in E Plane

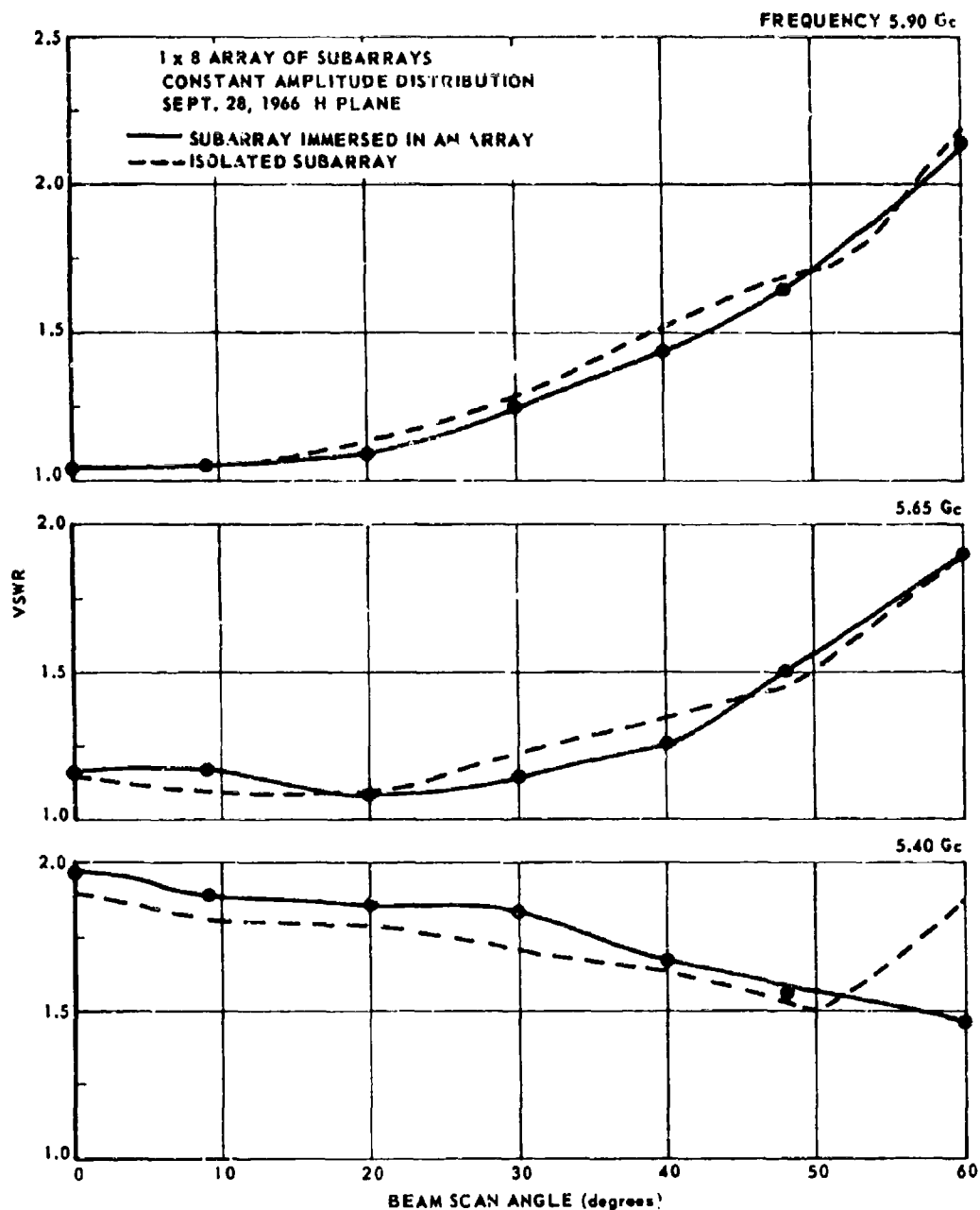


Fig. 3-9 Scanned VSWR Comparison of Immersed and Isolated Subarray, H Plane

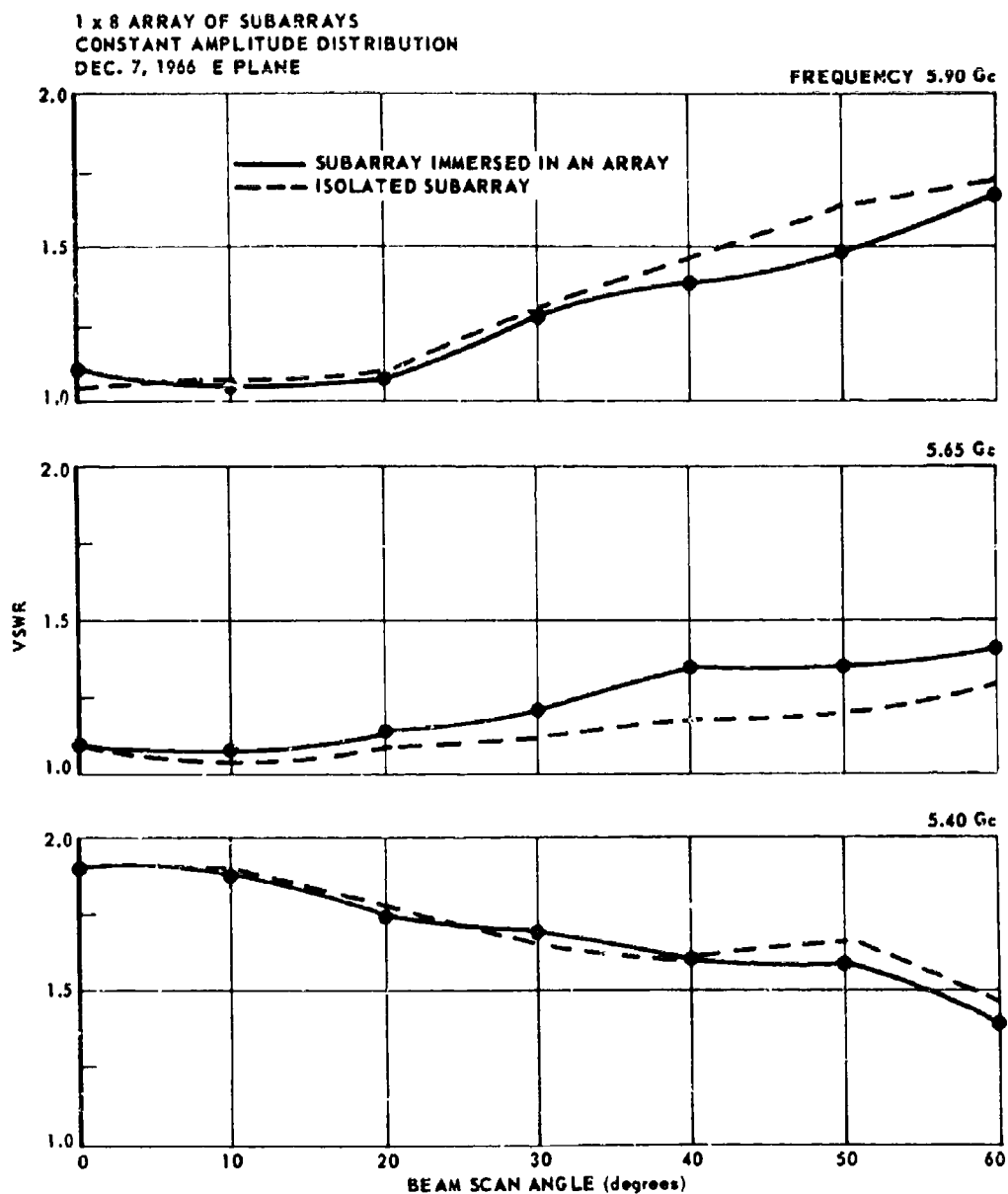
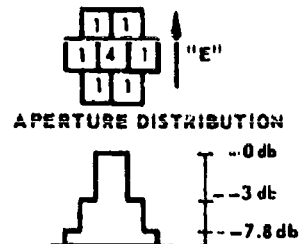


Fig. 3-10 Scanned VSWR Comparison of Immersed and Isolated Subarray, E Plane

MEASURED VSWR HAS BEEN PLOTTED
THESE VALUES HAVE NOT BEEN COR-
RECTED FOR THE 1.0 DB INSERTION
LOSS OF THE SUBARRAY

FREQUENCY = 5.65 Gc



— SUBARRAY IMMERSED IN AN ARRAY
- - - SUBARRAY ISOLATED

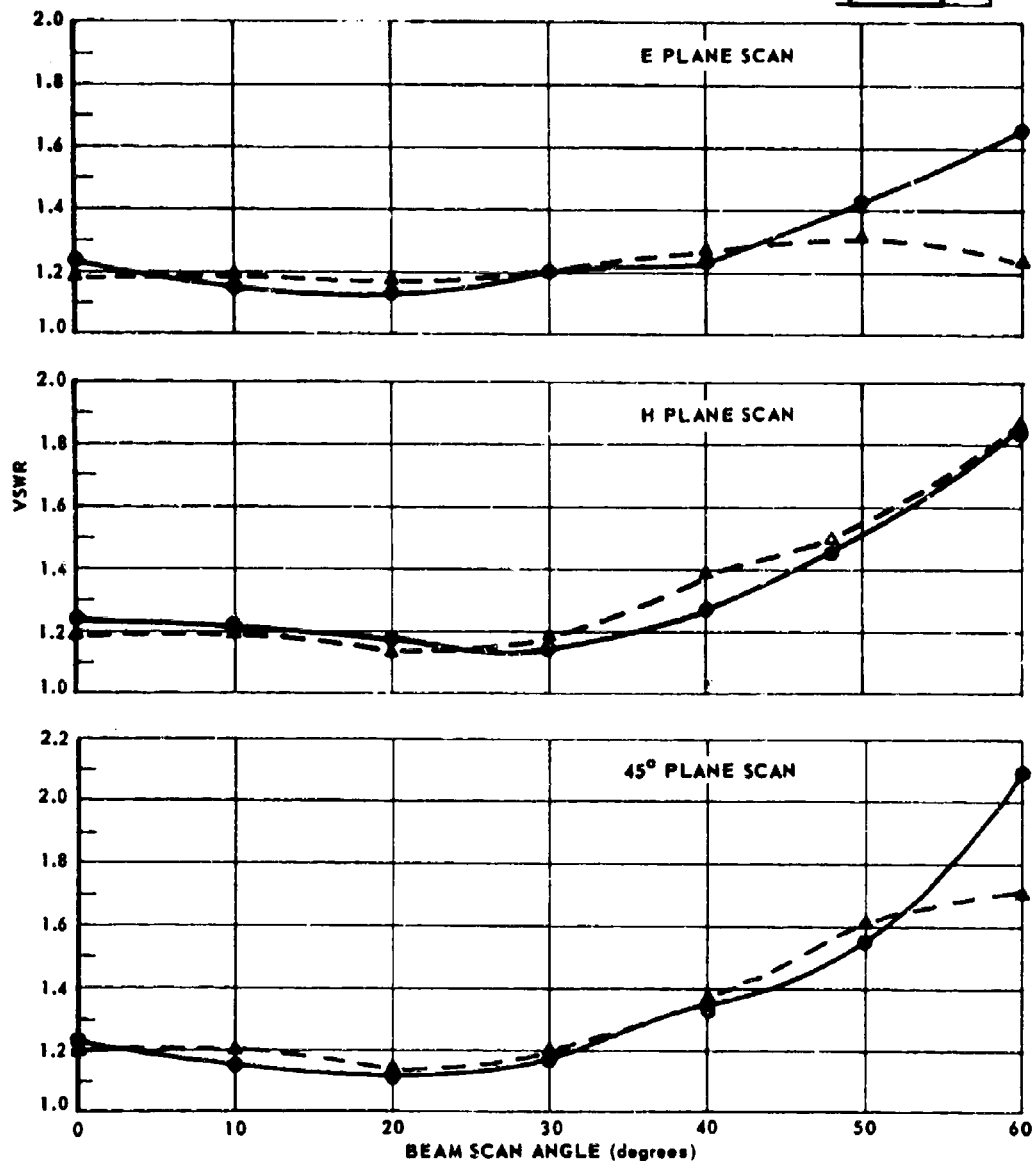


Fig. 3-11 Scanned VSWR Comparison of Immersed and Isolated Subarray, Circular Aperture

Figure 3-12 compares the VSWR of a central subarray immersed in a uniformly illuminated array to the same subarray with a quantized $1 + \cos \frac{\pi x}{a}$ distribution across the array. In both the E plane and H plane cases, it is seen that the difference in measured VSWR is negligible.

In all cases, the results presented are measured results. To convert these results to a VSWR at the aperture face, it is necessary to use the curve provided in Fig. 2-6. This has been done in computing the couplings given above.

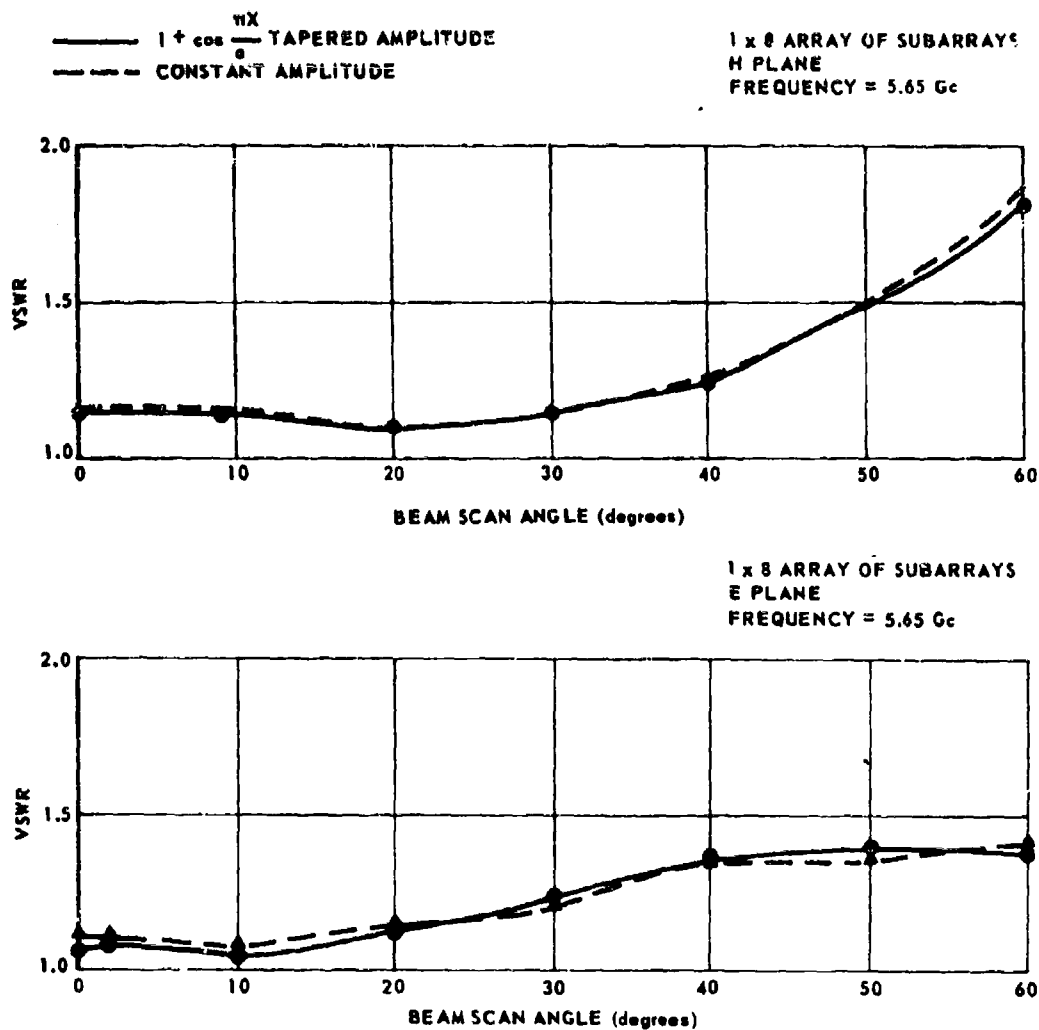


Fig. 3-12 VSWR Comparison of Tapered and Uniformly Illuminated Array

3.4 Beam Steering Accuracy

3.4.1 Introduction

Steering a phased array requires a large number of computations, many drivers and complex wiring. Each of these items was reduced in number and simplified by taking advantage of the symmetry properties of an array of subarrays.

Using such an array, the phase commands computed for one subarray may be applied to similarly located elements in all other subarrays. Steering the subarray beam will be referred to as the coarse steering. Behind each subarray, an additional phase shifter (or time delay) is required and this will be referred to as the fine steering. If amplifiers are placed between the fine steering and the subarrays (Fig. 3-13), then no additional loss is incurred by the fine steering.

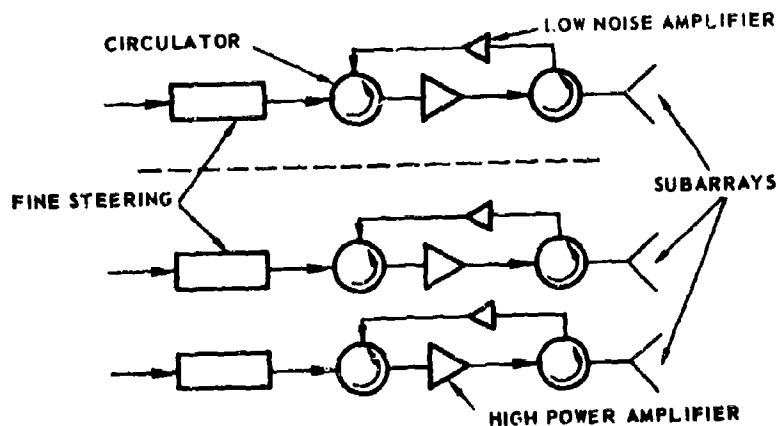


Fig. 3-13 Fine Steering and Array of Subarrays

The beam steering accuracy is determined almost entirely by the fine steering. This may be seen by considering the subarray as an element with a pattern of $\frac{\sin nx}{n \sin x}$ as shown in Fig. 3-14. This element pattern, with a relatively broad beam (typically 14° at 3 db), is steered by means of the subarray phase shifters (coarse steering). With four-bit phase shifters and diametric wiring, it was shown in Section 2.4 that the subarray beam moves in steps of approximately $3/4^\circ$, thus the name, coarse steering.

Now consider the pattern of an array of isotropes, one located at the center of each subarray. This will be referred to as the array factor. This array factor is steered by means of the phase shifters behind the subarray (fine steering).

The antenna pattern is the product of the subarray pattern and the array factor (Fig. 3-14). Therefore, if there is a null in the array

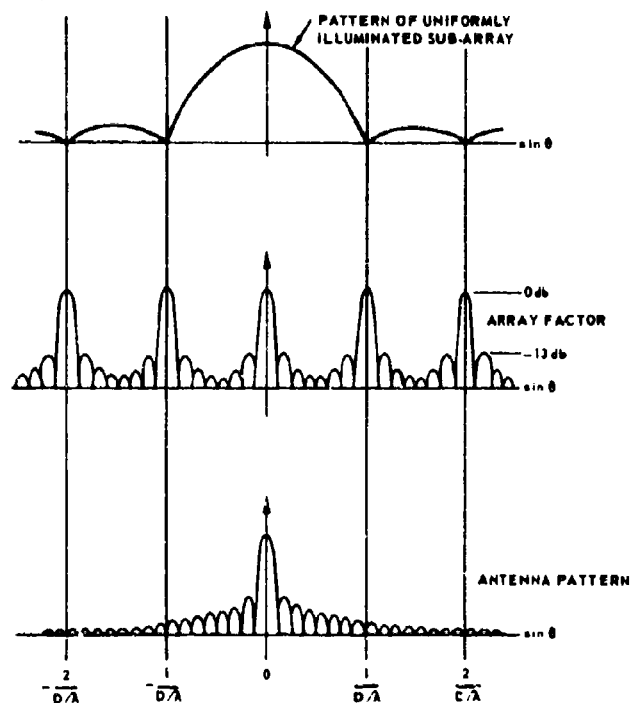


Fig. 3-14 Subarray Pattern, Array Factor and Antenna Pattern

factor, a null will appear at the same position in the overall pattern regardless of the pointing direction of the subarray pattern. In practice, the subarray is pointed as close to the beam pointing direction as possible (say within $\frac{1}{2}^\circ$) and the array factor is steered within the subarray pattern to a much finer accuracy. For purposes of visualization, it is convenient to think of the subarray pattern as remaining fixed in space as the array factor is steered within the subarray pattern (Fig. 3-15).

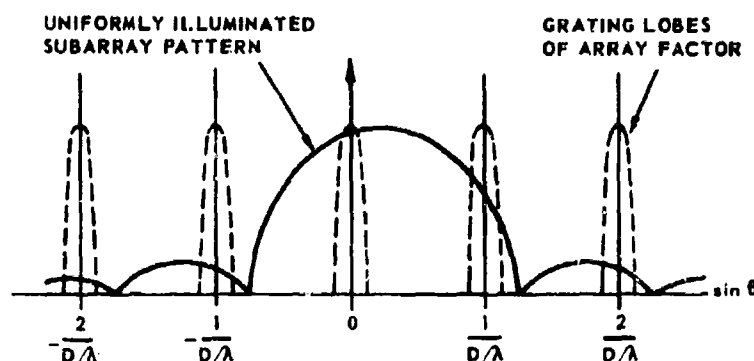


Fig. 3-15 Fine Steering within Subarray Pattern

The previous discussion assumed identical phasing on similar elements in each subarray. In practice, there are random phase errors caused by variations in insertion phase, differential phase, driver currents, etc. An exact analysis does not permit pattern multiplication as performed above. Still, the above analysis provides both insight into the steering and an excellent estimate for the fine steering. The effects of the random phase errors may be computed by assuming perfect fine steering. The aperture then appears as a continuous one with random phase errors. This problem has been discussed by several researchers (Refs. 14 and 15), and Allen has provided a simple formula to compute the rms difference pattern beam pointing error for a linear array. To account for the planar array of elements used in this program, the formula has been modified slightly, the error in fractional beamwidths being

$$\frac{\Delta\theta}{BW} \approx 0.56 \frac{\sigma}{N}$$

σ = rms phase error (radians)

N = number of elements

BW = beamwidth of array.

Assuming an rms error of 20° (considerably greater than can be accounted for in this array), the rms beam pointing accuracy would be 0.01 beamwidth, approximately $\frac{1}{4}$ milliradian for the array of eight subarrays.

It is seen that for this case, the random errors have little influence on the beam pointing accuracy, and pattern multiplication is a valid method for analyzing the beam pointing direction. The increments of fine steering may be calculated using a technique similar to that employed in Section 2.4. In this case, consider the pattern of eight isotopes, one at the center of each subarray. This pattern will be the array factor. Since the spacing is exactly eight times that of the elements, the angular variation may be written immediately

$$\sin \theta_o = \frac{1}{8\pi} \sum \varphi_n \times \frac{1}{8}.$$

If opposite phase increments of $\frac{\pi}{64}$ ($\approx 3^\circ$) are applied to a pair of symmetrically displaced isotopes, the null of the difference pattern will move by

$$\Delta \sin \theta = \frac{1}{8\pi} \times \frac{\pi}{64} \times \frac{1}{8} = \frac{1}{(64)^2}.$$

At boresight, this corresponds to a null movement of approximately $\frac{1}{4}$ milliradian. For the laboratory measurements, the fine phase control was done using Hewlett-Packard precision phase shifters, with a specified accuracy of 3° ($\approx \frac{\pi}{64}$). The pointing error, caused by all eight precision

phasors being in error by 3° each, could achieve a maximum value of 1 milliradian.

3.4.2 Results of Beam Steering Accuracy Measurements

As shown in the previous section, a phased array with reasonable phase errors will have good beam pointing accuracies. So good, in fact, that the errors due to the measuring apparatus may be larger than the errors caused by the array itself. Comprehensive measurements are still required to determine that the array is functioning properly and that changes in scan angle or frequency (both causing changes in mutual coupling) do not affect the pointing accuracy.

Two techniques were used for measuring the beam pointing accuracy; the first technique involved scanning the beam through the use of phase shifters, the second involved changing the frequency and noting the change in null position. The results of these measurements are discussed below. It will be seen that the maximum error observed was 1.2 milliradians ($\approx 1/50$ BW) and the rms error was approximately half of this. Such small errors can be accounted for by the fine steering alone, or by the measuring apparatus alone. It was felt that the small errors observed indicate a good overall performance, and no further investigation into the source of the errors was initiated.

Steering Array by Phasing--In these measurements, a quantized approximation to a $\sin \frac{\pi x}{2}$ (difference pattern) amplitude distribution was excited across the array by adjusting the RF amplitude into each subarray (Fig. 3-16). The array was then phased to boresight. To steer the null to the desired scan angle, both the fine steering (precision phase shifters, one behind each subarray) and the coarse steering (ferrite phase shifters

in the subarrays) were employed. The null of the difference pattern was taken to be the pointing direction of the array.

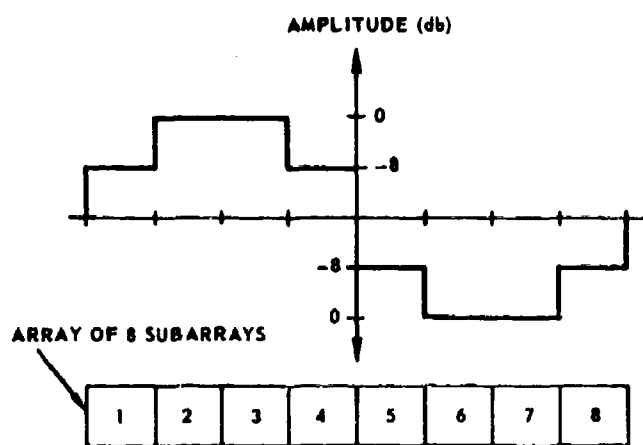


Fig. 3-16 Quantized Approximation to $\sin \frac{2\pi x}{a}$

Seventy measurements were taken, 35 in the H plane, and 35 in the E plane. Figures 3-17 and 3-18 present the results of these measurements. As seen from these graphs, all but one of the 70 points fall within $\frac{1}{50}$ BW of the calculated beam pointing direction. In terms of absolute error, the worst error occurs in the E plane and is 1.2 milliradians. From these data, the absolute rms errors have been calculated as $\frac{1}{136}$ beamwidth in the H plane and $\frac{1}{89}$ beamwidth in the E plane.

Steering Array with Frequency--Since the array does not have time delay steering, the beam will scan as the frequency is varied. This may be seen upon examination of Fig. 3-19.

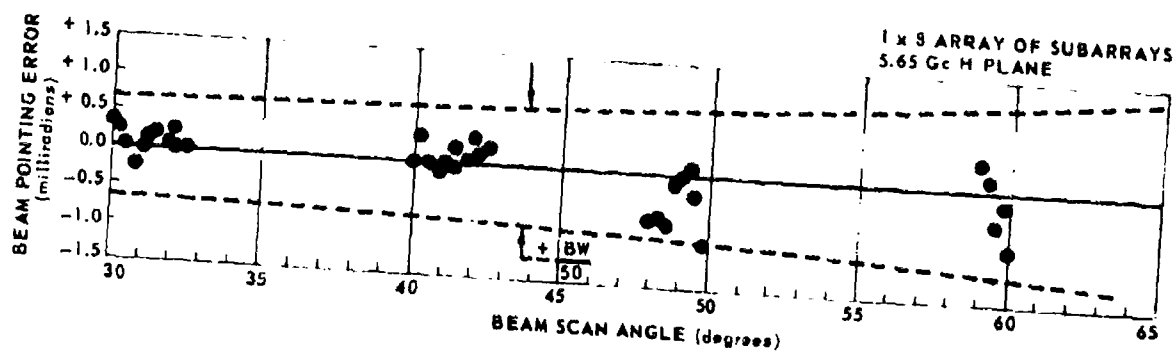


Fig. 3-17 Absolute Beam Pointing Accuracy vs. Beam Scan Angle, H Plane

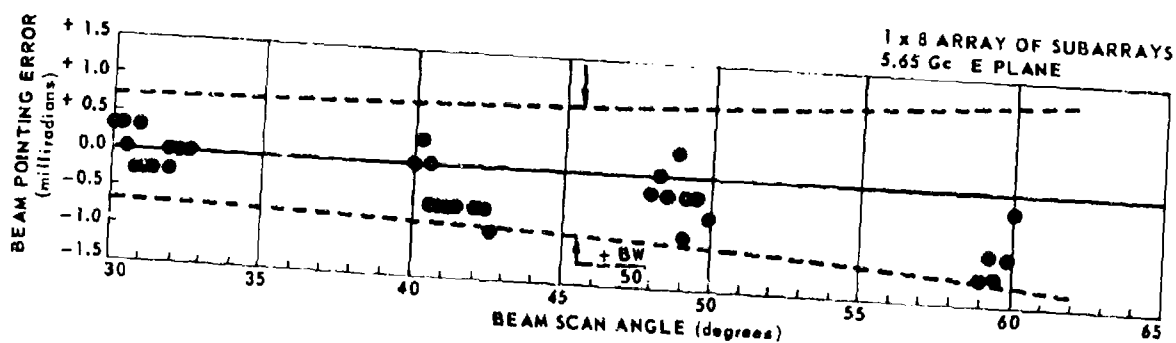


Fig. 3-18 Absolute Beam Pointing Accuracy vs. Beam Scan Angle, E Plane

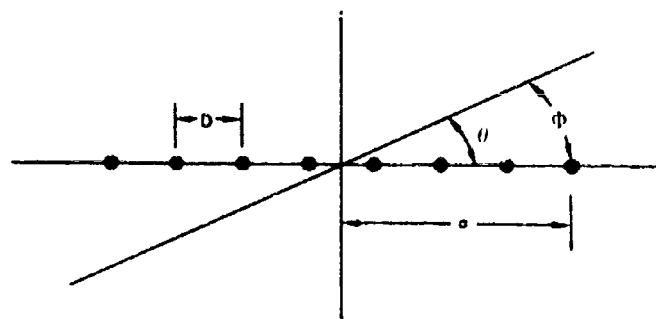


Fig. 3-19 Frequency Steering of Array

Consider the array of isotropes, one at the center of each subarray, representing the array factor. The scan angle θ is determined by

$$\Phi = \frac{2\pi a}{\lambda} \sin \theta$$

$$\sin \theta = \frac{\Phi}{a} \frac{\lambda}{2\pi}$$

a = distance to center of end subarray (inches)
 Φ = fixed phase (radians)
 λ = free space wavelength (inches).

If the phase setting (Φ) and the aperture size are fixed, then $\sin \theta$ is directly proportional to the wavelength; a 10% change in λ inducing a 10% change in $\sin \theta$.

For these measurements, the beam was initially scanned to 60° in the H plane by means of the fine and coarse steering. The frequency was then changed over a 10% band and the movement of the null position was tracked. The results are presented in Fig. 3-20. The largest error is seen to be less than $\frac{1}{60}$ of a beamwidth (1 milliradian) from the calculated value.

1 x 8 ARRAY OF SUBARRAYS
ALIGNED IN THE H PLANE
AMPLITUDE DISTRIBUTION $\approx \sin \frac{2\pi x}{a}$

BEAM STEERED TO 60° AT 5.65 Gc
FREQUENCY WAS CHANGED AND
THE POINTING DIRECTION MEASURED

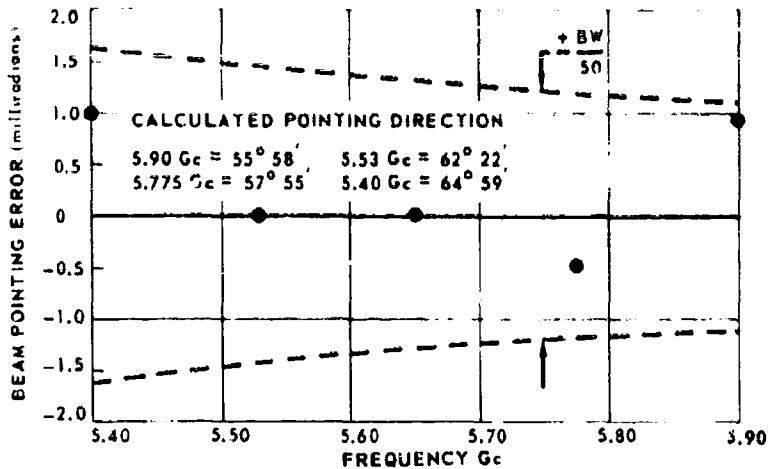


Fig. 3-20 Beam Pointing Error vs. Frequency, H Plane

A similar experiment was performed at boresight where the beam should not scan with frequency since $\Phi = 0$. The results of this experiment are presented in Fig. 3-21. Once again, the null movement was less than $\frac{1}{60}$ of a beamwidth as the frequency was changed over a 10% band.

1 x 8 ARRAY OF SUBARRAYS
ALIGNED IN THE H PLANE
AMPLITUDE DISTRIBUTION $\approx \sin \frac{2\pi x}{a}$

BEAM STEERED TO BORESIGHT
AT 5.65 Gc FREQUENCY WAS CHANGED
AND THE VARIATION FROM BORESIGHT
MEASURED

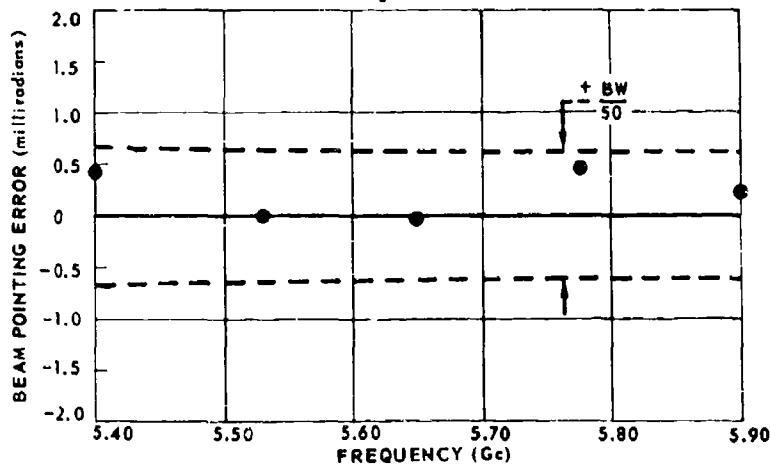


Fig. 3-21 Boresight Pointing Error vs. Frequency, H Plane

3.5 Patterns and Quantization Lobes

3.5.1 Introduction

An array of subarrays may be analyzed by considering independently the pattern of a subarray, and the pattern of an array of isotropes (an isotrope being located at the center of each subarray). Multiplying these two patterns produces the antenna pattern (Fig. 3-22). A necessary restriction is that the patterns of all subarrays are the same.

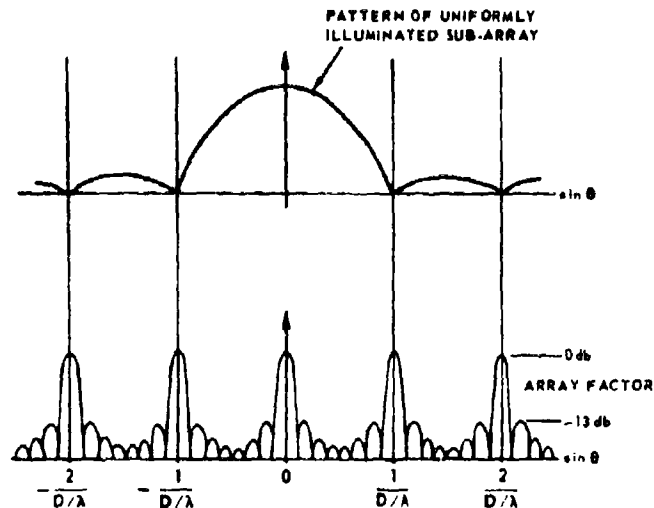


Fig. 3-22 Subarray Pattern and Array Factor

For this program, the amplitude distribution across any given subarray was approximately uniform, resulting in the typical $\frac{\sin 2kx}{2k \sin x}$ pattern expected of a uniformly illuminated array of $2k$ elements. The subarray pattern may be derived as in Section 2.2.4. In this case, the sum pattern is computed. If there are $2k$ elements in a linear array, the sum pattern is

$$v = \sum_{n=1}^k e^{-j \left\{ \frac{2\pi}{\lambda} \frac{(2n-1)}{2} d \sin \theta - \phi_n \right\}} + \sum_{n=1}^k e^{-j \left\{ \frac{2\pi}{\lambda} \frac{(2n-1)}{2} d \sin \theta + \phi_{-n} \right\}}$$

d = interelement spacing

ϕ_n = phase at element n

$2k$ = number of elements in line.

With diametric wiring, the phases on elements symmetrically displaced about the center are related by

$$\phi_n = -\phi_{-n}$$

then

$$v = \sum_{n=1}^k \cos \left\{ \frac{2\pi}{\lambda} \frac{(2n-1)}{2} d \sin \theta - \phi_n \right\}.$$

This pattern should be multiplied by $\sqrt{\cos \theta}$ to account for the directional properties of the individual radiators. The resultant pattern is the pattern of a subarray. If the phasing were perfect, the pattern would have exactly the right shape. With quantized phasing, the patterns are still near theoretical as evidenced by the subarray patterns in Section 2.2.2.

The array factor, determined by the array of isotropes, may have an amplitude distribution other than uniform. The pattern for the array factor is given by

$$V \sum_{N=1}^K A_N \cos \left\{ \frac{2\pi}{\lambda} \frac{(2N-1)}{2} D \sin \theta - \phi_N \right\}.$$

D = intersubarray spacing

$\Phi_N = \frac{\pi(2N-1)}{\lambda} D \sin \theta_0$ = phase at subarray N to steer
 array factor to θ_0

A_N = amplitude at subarray N

$2K$ = number of subarrays in line .

This is a pattern of grating lobes with the lobe spacing given by

$$\sin \chi = \frac{\lambda}{D} \quad \chi = \text{angle between grating lobes.}$$

It is illustrative to consider a few simple cases of scanning to observe the manner in which undesirable lobes form.

Case I - Uniform amplitude distribution across entire array;
 subarray and array pointed in the same direction.

In this case, the radiation pattern is known to be that of a linear array of $4kK$ elements, which has the shape $\frac{\sin 4kKx}{4kK \sin x} \sqrt{\cos \theta}$.

Examining the two patterns (Fig. 3-22), it is seen that aside from the main lobe, the maximum of each grating lobe falls at a null of the subarray pattern. At the position of the grating lobes, the product of the two patterns is therefore zero, and side lobes of opposite phase are formed on either side of the null to conform to the pattern expected.

Case II - Uniform amplitude across entire array. Subarray
 pattern and array factor slightly displaced.

The subarray beam steering is done in quantized steps. In Section 2, it was shown that in the H plane the beam moves in steps of $1/16$ of a subarray beamwidth. Assuming the fine steering (array

factor) to be correct, the null of the subarray pattern may be displaced from the grating lobe by $1/32$ of a subarray beamwidth, resulting in a quantization lobe of -30 db (Fig. 3-23). As discussed in Section 2.2.5, one roundoff rule produced a displacement of $1/8$ of a subarray beamwidth with a resultant quantization lobe of -18 db.

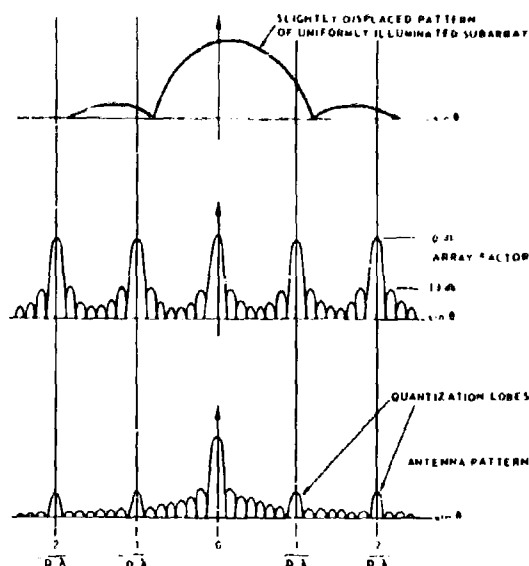


Fig. 3-23 Quantization Lobe Caused by Displacement of Array Factor from Subarray Pattern

The level of the quantization lobe may be simply calculated by noting that the slope at the null of the subarray pattern has an absolute value of approximately unity per beamwidth. Therefore, the fractional beamwidth is approximately equal to the fractional amplitude (i.e., $1/8$ BW displacement implies a lobe with $1/8$ the voltage of the main lobe). This technique assumes a very narrow array factor corresponding to a large number of subarrays. In practice, the finite width of an array factor grating lobe may have significance. This additional factor will

be taken into account in the next section where individual patterns are analyzed. Another technique for computing the quantization lobes is given in Appendix B.

Further displacement between the grating lobe and the null of the subarray pattern may be caused by a change in frequency. If it is assumed that the grating lobe pattern remains fixed in space (i. e., time delay used for fine steering), the displacement of the subarray null may amount to $1/6$ BW for a $\pm 5\%$ frequency variation resulting in a -15 db quantization lobe. This can be easily corrected by steering either the array factor or the subarray pattern.

Case III - Amplitude taper across the subarray.

If the subarray pattern is broadened, the nulls will be displaced from the grating lobe maxima. The resulting lobe will be dependent upon the extent of the beam broadening. To determine the level of the lobe, it is only necessary to note the level of the subarray pattern at the grating lobe position. Some typical examples are:

Cosine amplitude taper -14 db

$1 + \cos \frac{\pi x}{a}$ amplitude taper -18 db .

Case IV - Constant illumination across each subarray, quantized amplitude distribution across array.

In this case, the null of the subarray pattern once again falls exactly at the peak of the grating lobe. However the grating lobe is broader and will cause the sidelobes on either side of the null position to increase slightly. This effect is considered to be negligible in a sizeable array where the beamwidth of the array factor is considerably smaller than that of the subarray. The quantization lobes for an

array factor stemming from a tapered illumination should be much the same as for an array factor stemming from a uniform illumination.

3.5.2 Results of Antenna Pattern Measurements

In an effort to detect any odd behavior in the performance of the array, more than 200 antenna patterns were taken. In this section, 32 of the patterns are presented along with performance charts which contain data extracted from many more patterns. The patterns were taken at various scan angles, frequencies, array configurations, and scan planes. In general, they indicate good predictable performance under all conditions of operation.

Of particular concern was the formation of grating lobes (quantization lobes). The primary cause of these lobes is the coarse steering of the subarray and the resulting displacement of the subarray pattern from the array factor. A secondary cause is the amplitude ripple in the E plane which produces a beam broadening of the subarray pattern in that plane. When these two additive affects, are accounted for, the calculated quantization lobes are in close agreement to the observed lobes.

The curves in Figs. 3-24 and 3-25 present the highest grating lobes observed in the two principal planes of scan. Note that at 5.65 Gc in both the E and H planes, the grating lobe level increases as the array is scanned. This is partially caused by a decrease in the gain of the main lobe at large scan angles, while the quantization lobes being closer to boresight, are not decreased nearly so much. Additionally, at very small scan angles the saw toothed phase error function (caused by quantized phasing) across the subarray contains very few cycles (say less than two). As the scan angle increases, the number

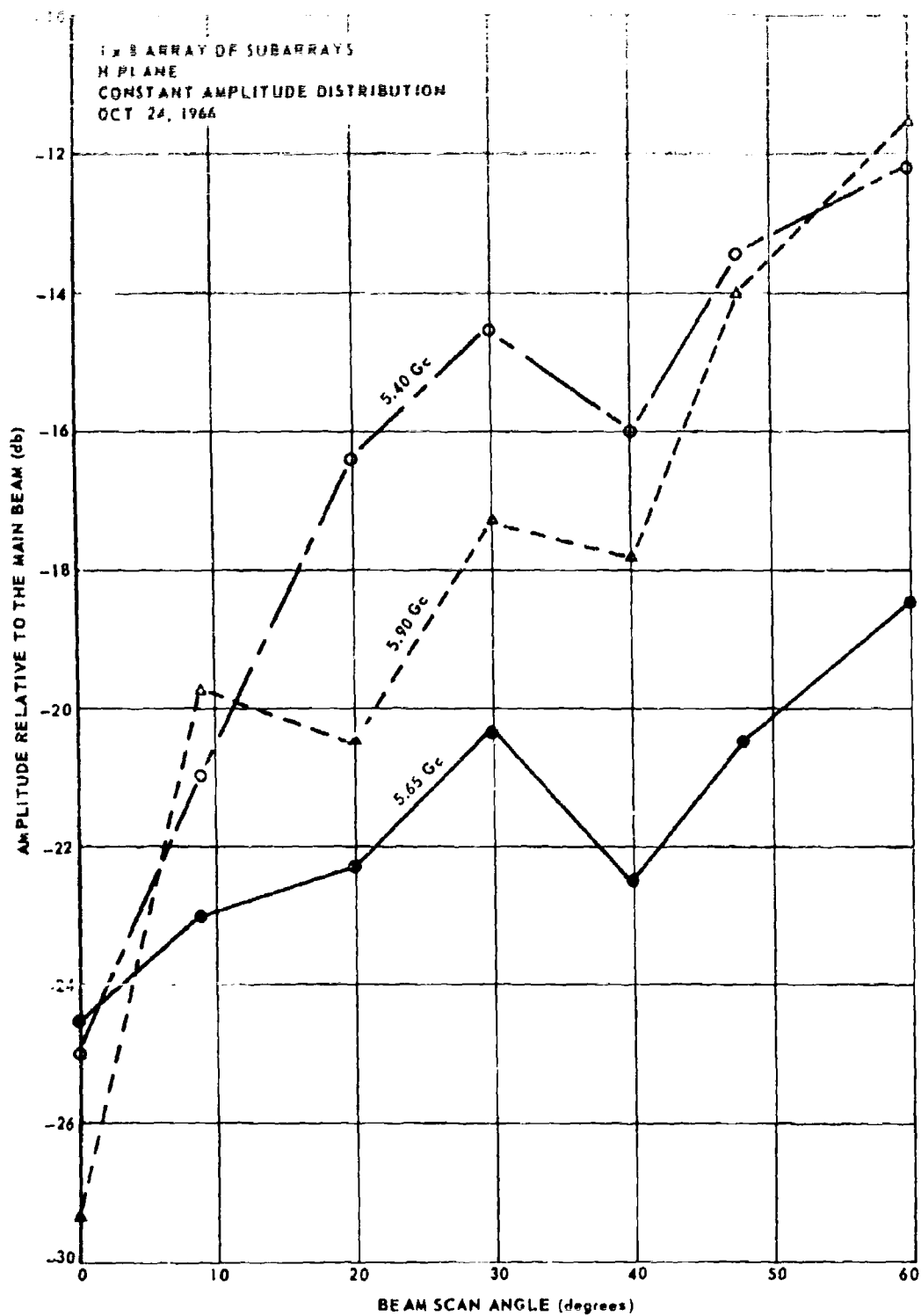


Fig. 3-24 Peak Quantization Lobe, H Plane Scan

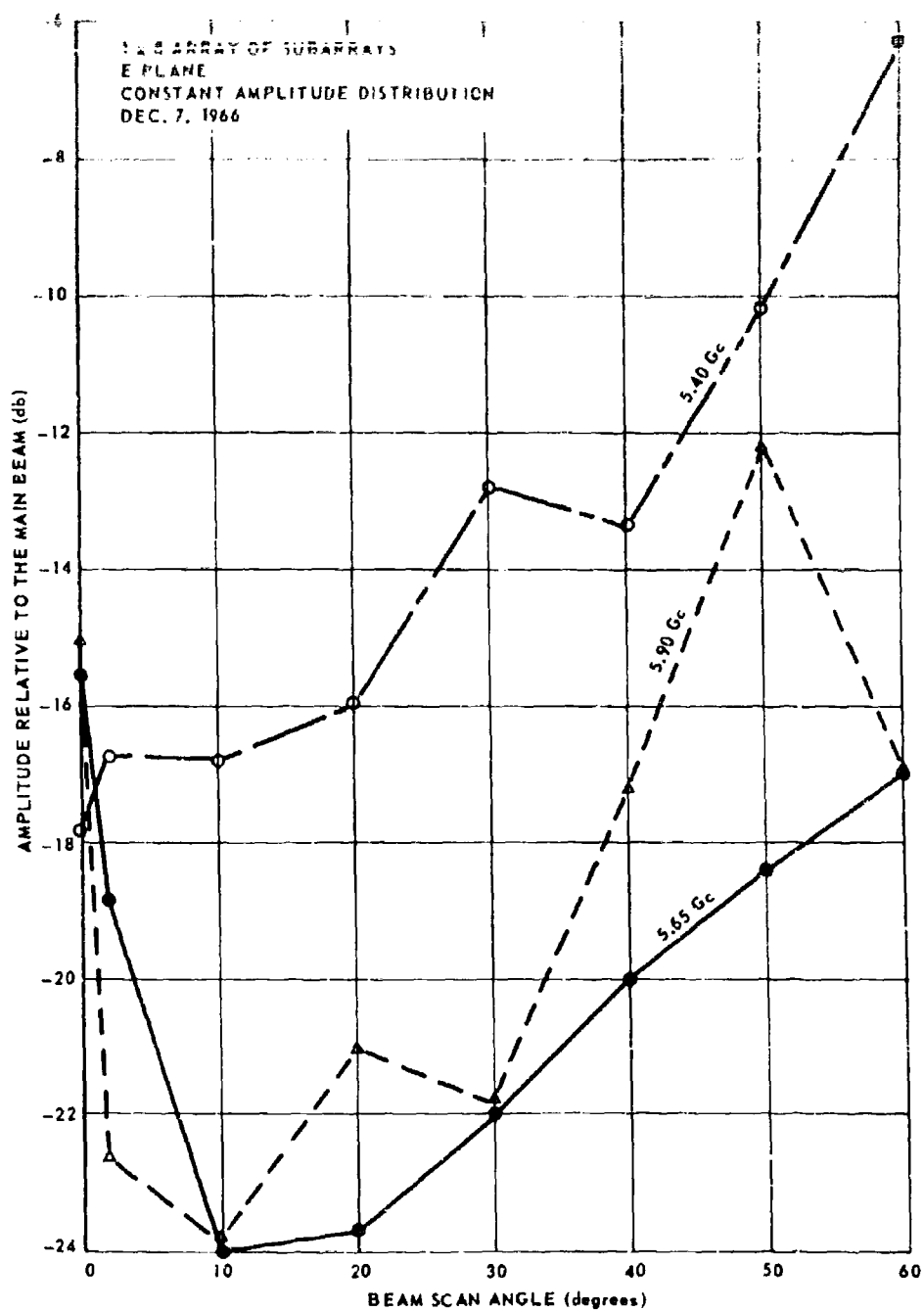


Fig. 3-25 Peak Quantization Lobe, E Plane Scan

of saw tooth cycles increase and the error pattern exhibits the quantization lobes expected from a periodic phase error. At 5.4 Gc and 5.9 Gc, the quantization lobes are aggravated by the subarray scanning as the frequency is changed. A remedy for this increase in quantization lobe level is to compute the element phasing at the desired frequency, rather than at the center of the band. This was not done during this program, since the instantaneous bandwidth of the array was the primary consideration. At 5.4 Gc in the E plane, the quantization lobes attain their highest level, the result of both a 3 db amplitude ripple across the E plane horn and the offset steering of the subarray. Several of these patterns will be discussed in more detail later in this section.

The level of the quantization lobes could be lowered considerably if:

1. Subarray steering is made more accurate.
2. Periodicities across both the array and the subarrays are broken up.

Techniques are available for performing both of these tasks. In Section 2.4 it was shown that with diametric wiring, a subarray may steer in steps of $1/16$ BW or smaller. The roundoff rule used in this program did not take full advantage of this capability and the quantization lobes suffered. In the future, beams will be steered using a more appropriate computational rule. Of course, if diametric wiring is not used, the subarray will steer in steps finer than $1/16$ BW.

To break up the periodicities in a subarray, an additional modification to the quantizing procedure is necessary. One such modification has been employed with good results. This procedure simply uses two quantizing rules: one rule for alternate phase shifters in a subarray, and another rule for the remaining phase shifters. In Figs. 3-26 and

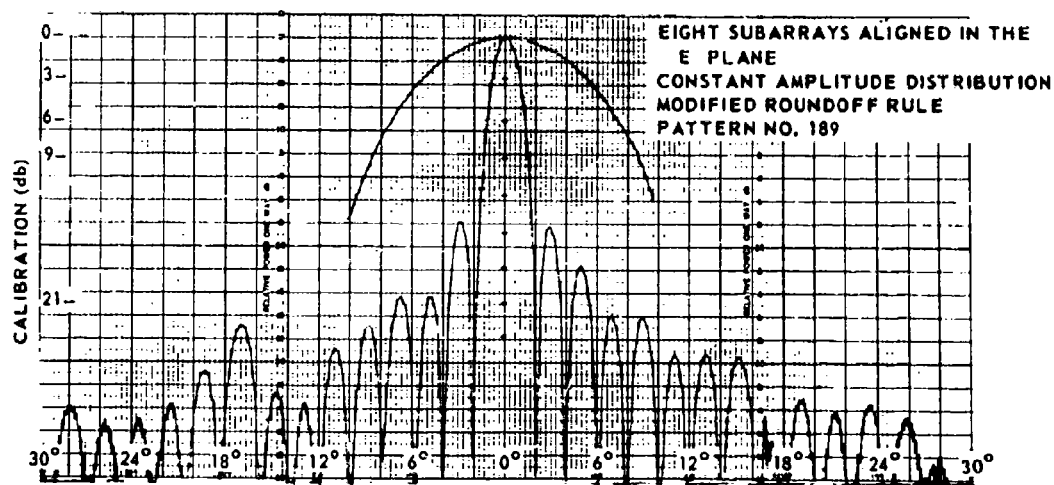
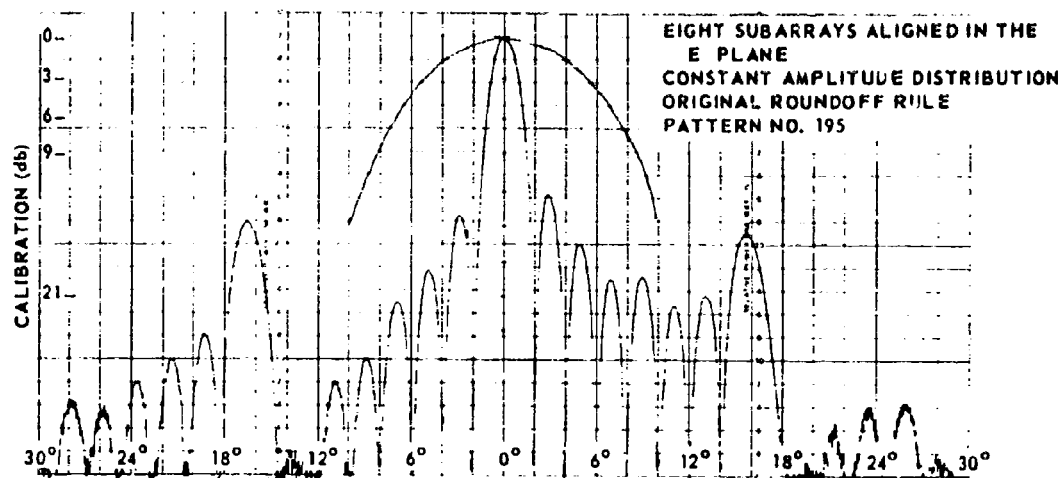


Fig. 3-26 A Comparison of Two Roundoff Rules; 0° Beam,
E Plane Pattern 5.65 Gc

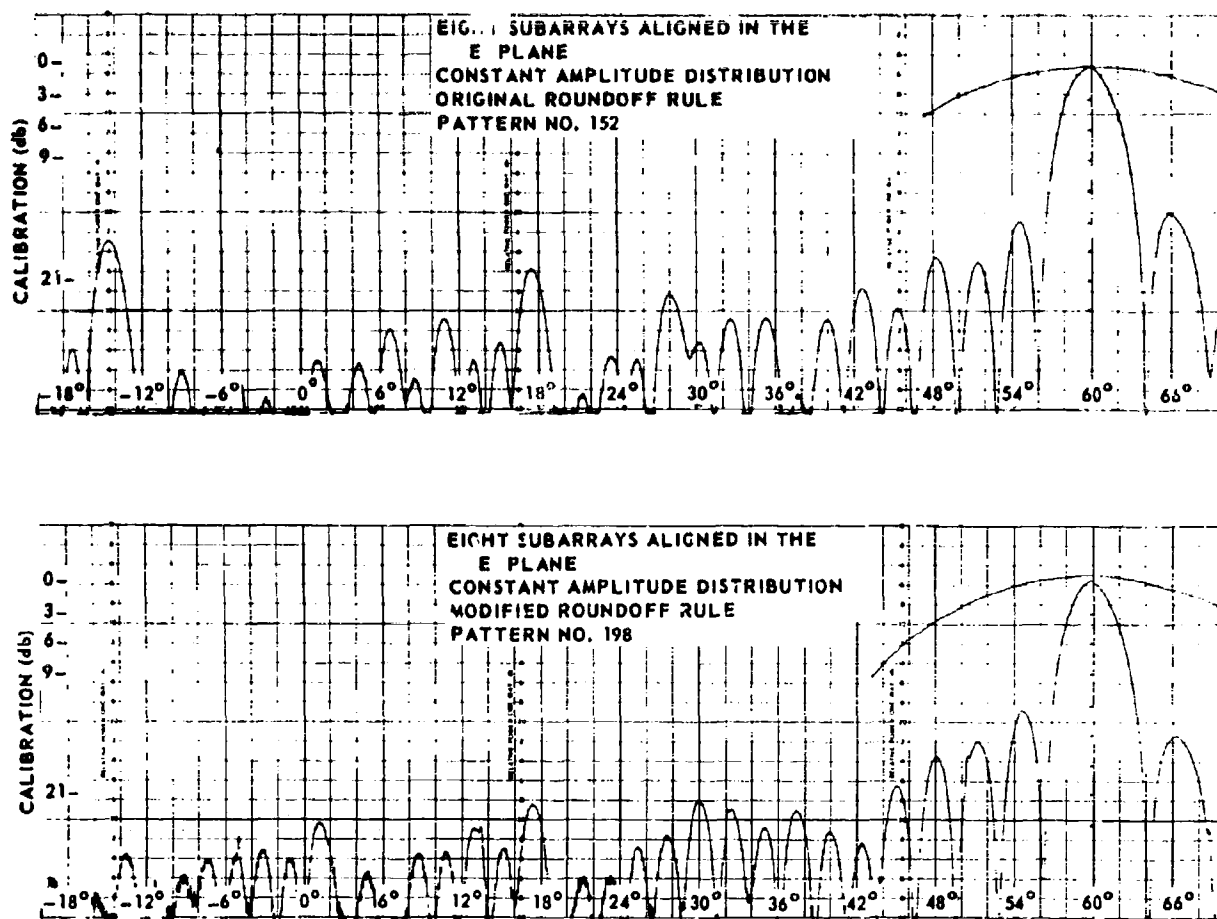


Fig. 3-27 A Comparison of Two Roundoff Rules; 60° Beam, E Plane Pattern 5.65 Gc

3-27, the patterns obtained using this procedure are compared to the patterns obtained using the original procedure as described in Section 2.2.5. Note that in the E plane at boresight (5.65 Gc) the new rule reduced the maximum quantization lobe from -15.5 db to -23 db. At 60° scan the maximum quantization lobe was reduced from -17 db to -21.5 db. Additional effort is planned for a further reduction in these lobes by similar techniques and by breaking up the periodicities from subarray to subarray.

As discussed in the previous section, a quantized amplitude distribution, produced by adjusting the RF input to each subarray, should reduce the sidelobes of the pattern but not the quantization lobes. This is demonstrated in Figs. 3-28 and 3-29. It is seen that the quantization lobes for uniform and tapered illumination are very nearly the same for all measured scan angles in both planes of scan.

Another measure of antenna performance is the level of the first sidelobe. Theoretically, a uniformly illuminated array should produce a first sidelobe of -13.2 db, and a quantized approximation of $1 + \cos \frac{\pi x}{a}$ should produce a first sidelobe level of -19.2 db. The measured patterns in both planes of scan have sidelobes which are very close to the theoretical values as demonstrated in Figs. 3-30 and 3-31. In no case does the measured sidelobe vary from theoretical by more than 1.6 db.

The remainder of this section presents a number of the antenna patterns. An amplitude calibration is provided at the left hand side of each pattern to correct for the small discrepancy between the printed markings on the chart and the actual calibration as measured prior to taking the pattern. Figures 3-32 through 3-37 are patterns taken at scan angles of 0°, 30°, 60° in both the H and E planes at 5.65 Gc. At

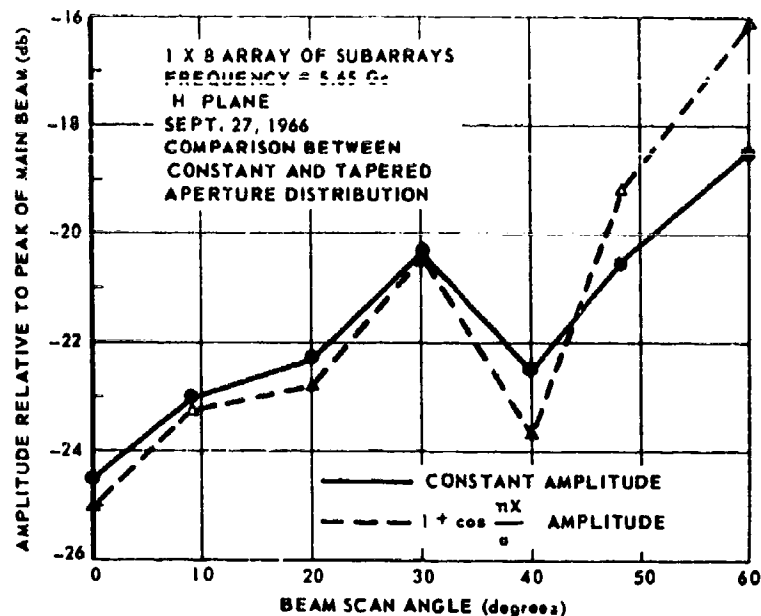


Fig. 3-28 Peak Quantization Lobe for Constant and Tapered Amplitude Distribution, H Plane Scan

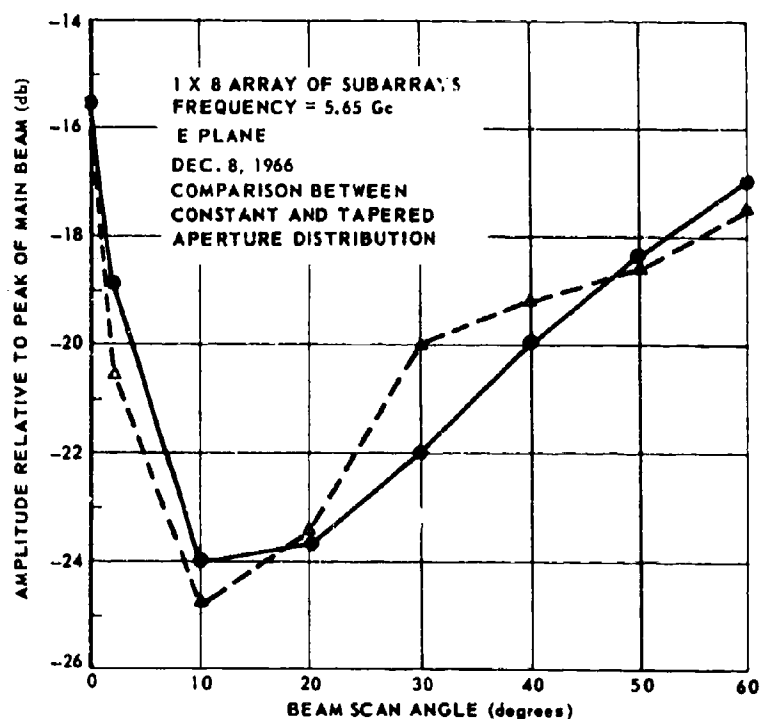


Fig. 3-29 Peak Quantization Lobe for Constant and Tapered Amplitude Distribution, E Plane Scan

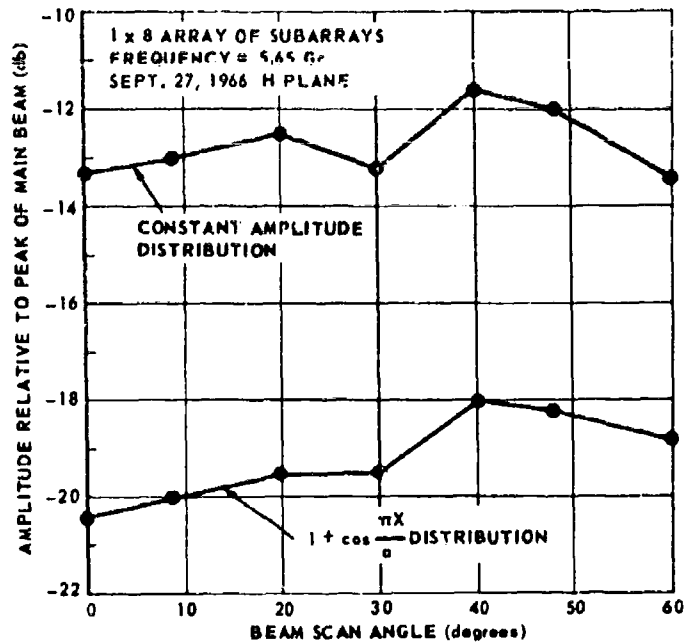


Fig. 3-30 1st Sidelobe Height vs. Scan Angle for Constant and Tapered Amplitude Distribution, H Plane

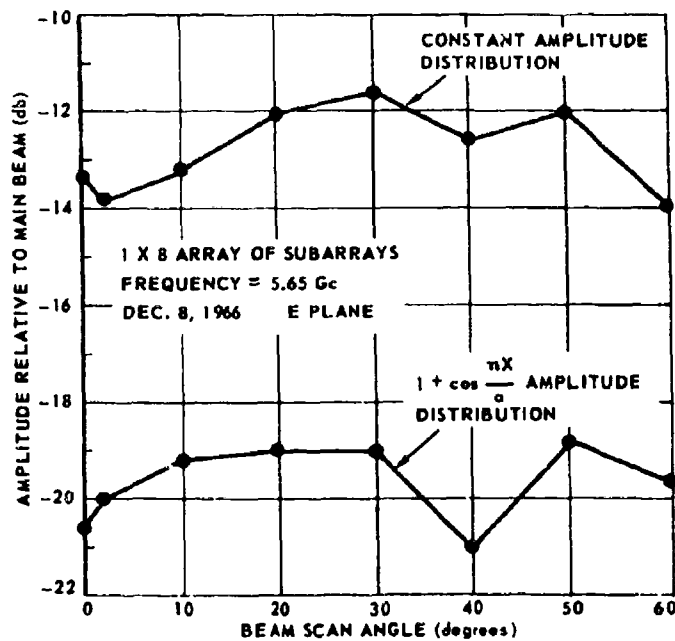


Fig. 3-31 1st Sidelobe Height vs. Scan Angle for Constant and Tapered Amplitude Distribution, E Plane

each scan angle patterns are given for three array illuminations: (a) uniformly illuminated array, (b) quantized approximation to $1 + \cos \frac{\pi x}{a}$, and (c) quantized approximation to $\sin \frac{2\pi x}{a}$ (difference pattern). It is of interest to examine the quantization lobes of some of these patterns for deviations from expected performance.

Figure 3-32 shows boresight patterns in the H plane, with a grating lobe of -24.5 db for the uniformly illuminated case. The theoretical pattern would have 7th and 8th side lobe levels of -27.4 db and -28.4 db, respectively. For this scan angle the quantized phasing produces a subarray pointing error of 1/20 BW. The measured pattern reveals that the subarray pattern is tilted by approximately 1/20 BW so that the 7th side lobe has been slightly decreased and the 8th side lobe slightly increased to form the quantization lobe of -24.5 db. As expected a lobe of approximately the same value, -25 db, is obtained with a tapered amplitude distribution.

Figure 3-33 shows the patterns of beams scanned to 30° in the H plane. For this scan angle, the quantized phasing produces a subarray pointing error of 1/16 BW. A reasonable approximation for the level of the quantization lobe is obtained by assuming it to be at the 3 db point of the array factor. This point is located 1/16 of a subarray BW from an array factor maximum, since there are eight subarrays. The quantization lobe should, therefore, be 3 db less than the value of the subarray pattern at a distance of 1/8 BW from the subarray null, which is calculated to be -21 db. The measured values for uniform and tapered distributions are -21.8 db and -21.5 db, respectively.

Figure 3-34 shows the patterns at 60° scan in the H plane. In this case, the maximum quantization lobes appear at the 3rd and 4th grating lobe position. This is caused by a distortion of the subarray

pattern at large scan angles as demonstrated in Section 2.2.1. Since the grating lobes appear near boresight while the main beam is at 60° , the grating lobes pick up an extra 3 db. This effect partially accounts for the quantization lobe increase at large scan angles. It is felt that the remainder of the increase is caused by the cyclic saw tooth phase error across the array.

Figure 3-35 shows the boresight patterns for the arrays aligned in the E plane. This pattern is especially interesting in that it demonstrates the deleterious effect of a $\pi/8$ phase split in the E plane, which results from the original computation rule. The subarray beam is tilted $1/8$ BW away from boresight. When the width of the array factor grating lobe is taken into account, the computed value of the quantization lobe is -17 db. The patterns indicate a level of -15.5 db. As shown earlier in this section, a new computation rule has reduced the quantization lobe to -23 db.

The remainder of the patterns presented were taken at 5.4 Gc and 5.9 Gc. The patterns (Figs. 3-38 through 3-41) are for beams at 0° , 30° , 60° of scan in both planes. Only the patterns for uniform illumination are shown here since they contain the essential information. Patterns for other illuminations have been taken and follow directly from the appropriate array factor. In general, these patterns are poorer than those obtained at 5.65 Gc. This is to be expected, since the subarray pattern scans as the frequency is changed. For example, consider the 5.4 Gc pattern at 30° scan in the H plane (Fig. 3-38). Due to quantized phasing, the subarray pattern was originally (5.65 Gc) steered $1/16$ BW away from the true position. As the frequency changed to 5.4 Gc, the pattern steered further from the true position by an additional $1/10$ BW. With the subarray pattern thus displaced from the array factor by approximately $1/6$ BW, the expected quantization lobe is -15 db. The observed

quantization lobe is 14.5 db. This quantization lobe can be significantly reduced by recomputing the phases required as the frequency is changed.

The poorest patterns occur at 5.4 Gc in the E plane (Fig. 3-40). Here an amplitude ripple across the E plane horn (see Section 2.3) broadens the subarray beam and further aggravates the problems caused by phase quantizing and frequency steering. It is expected that increasing the width of the E plane horn will reduce this problem considerably. With the present design, the problem is reduced by going to a frequency slightly higher than 5.4 Gc.

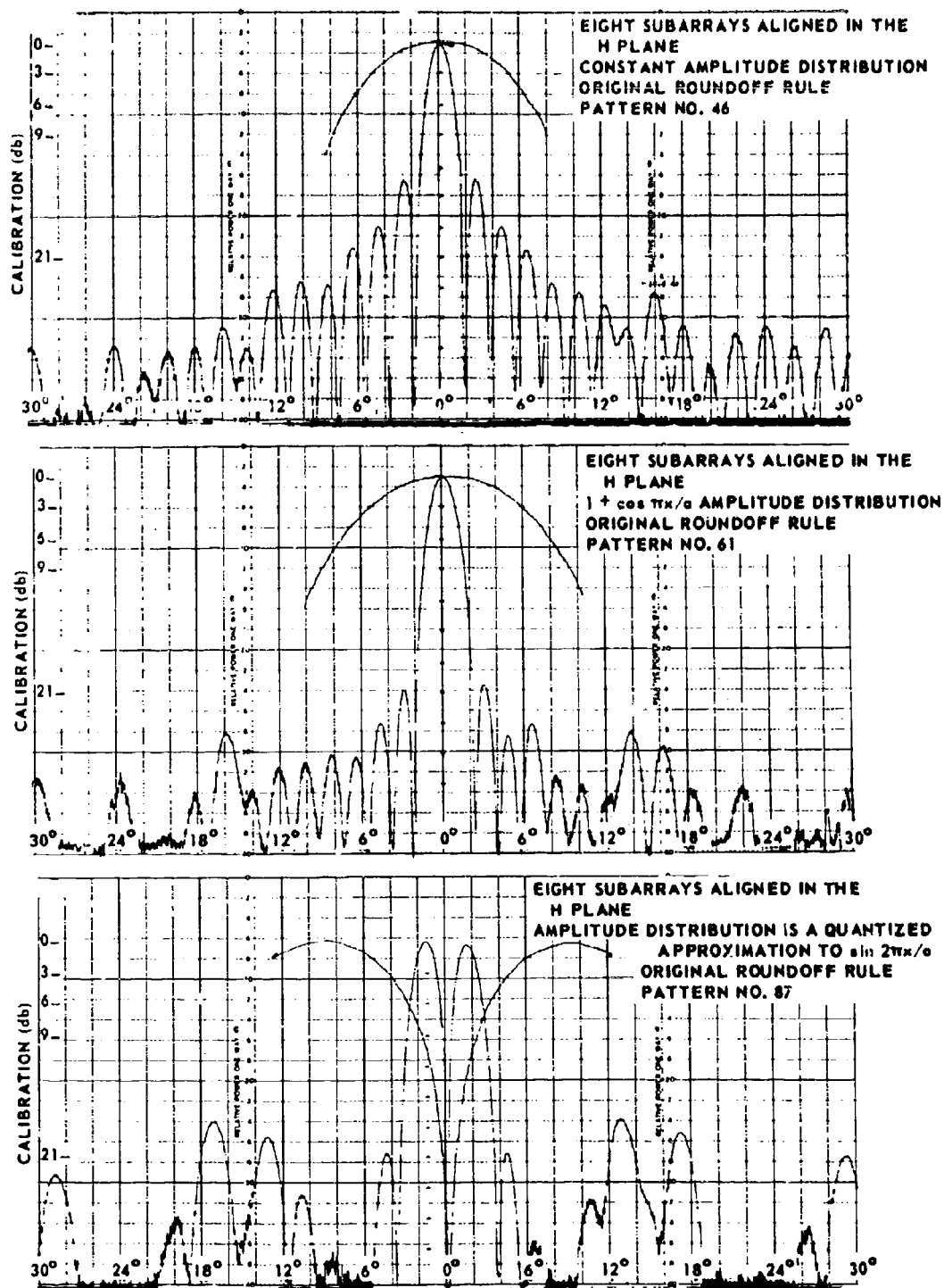


Fig. 3-32 0° Beam H Plane Patterns at 5.65 Gc

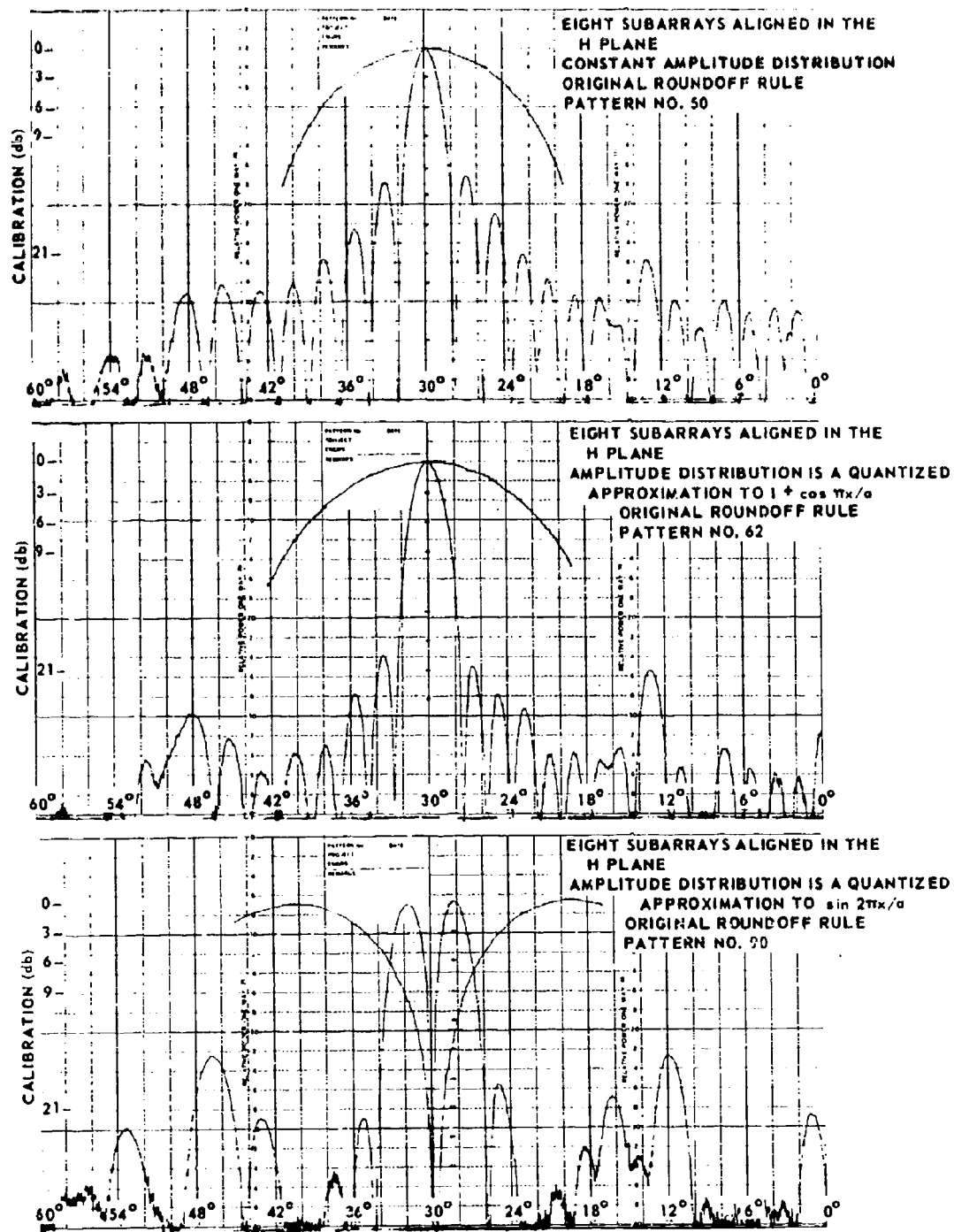


Fig. 3-33 30° Beam H Plane Patterns at 5.65 Gc

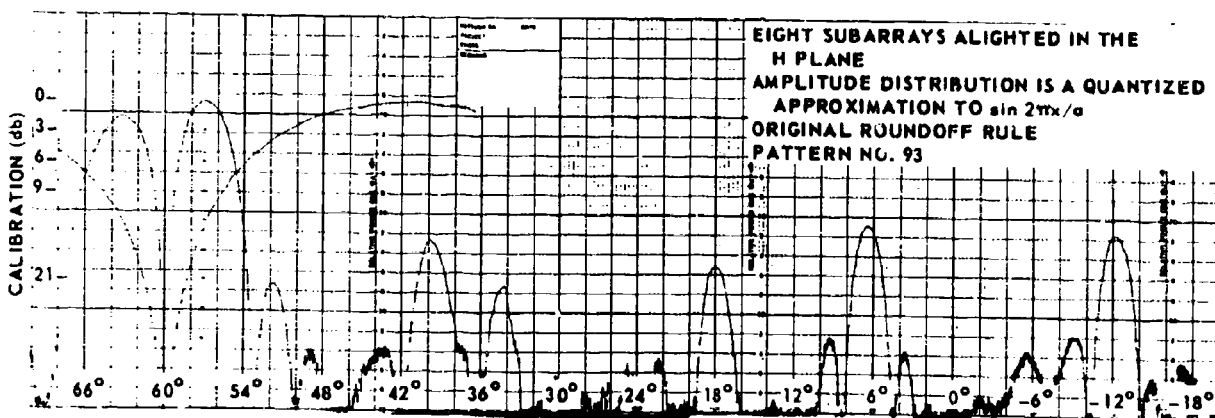
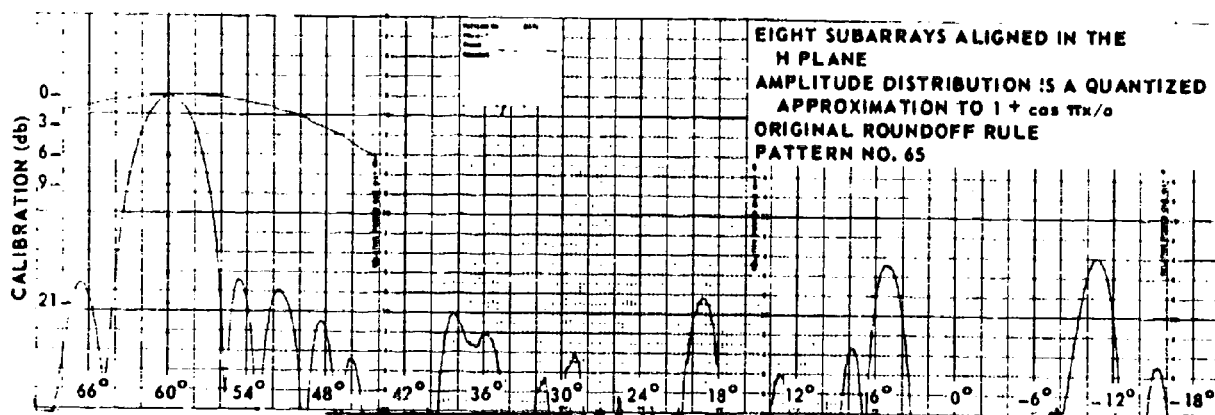
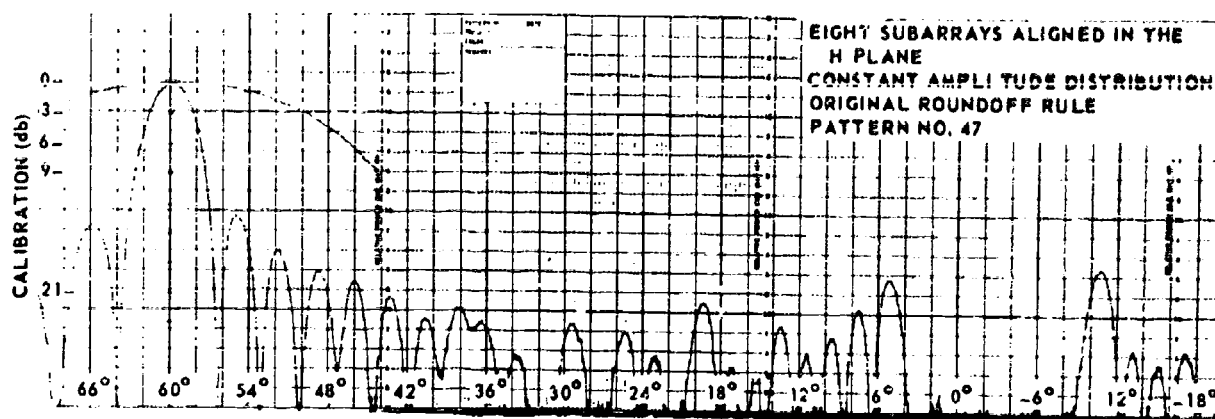


Fig. 3-34 60° Beam H Plane Patterns at 5.65 Gc

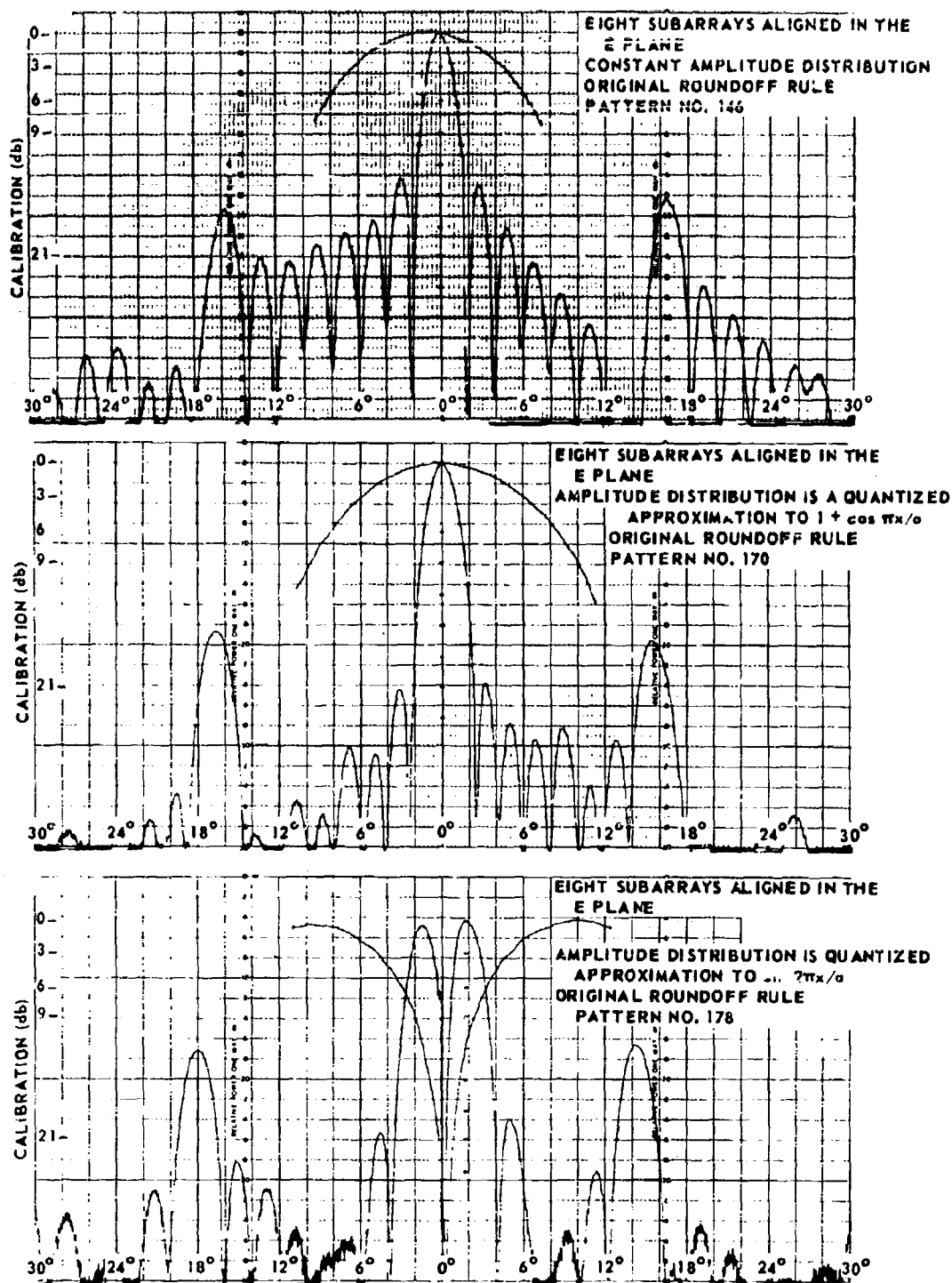


Fig. 3-35 0° Beam E Plane Patterns at 5.65 Gc

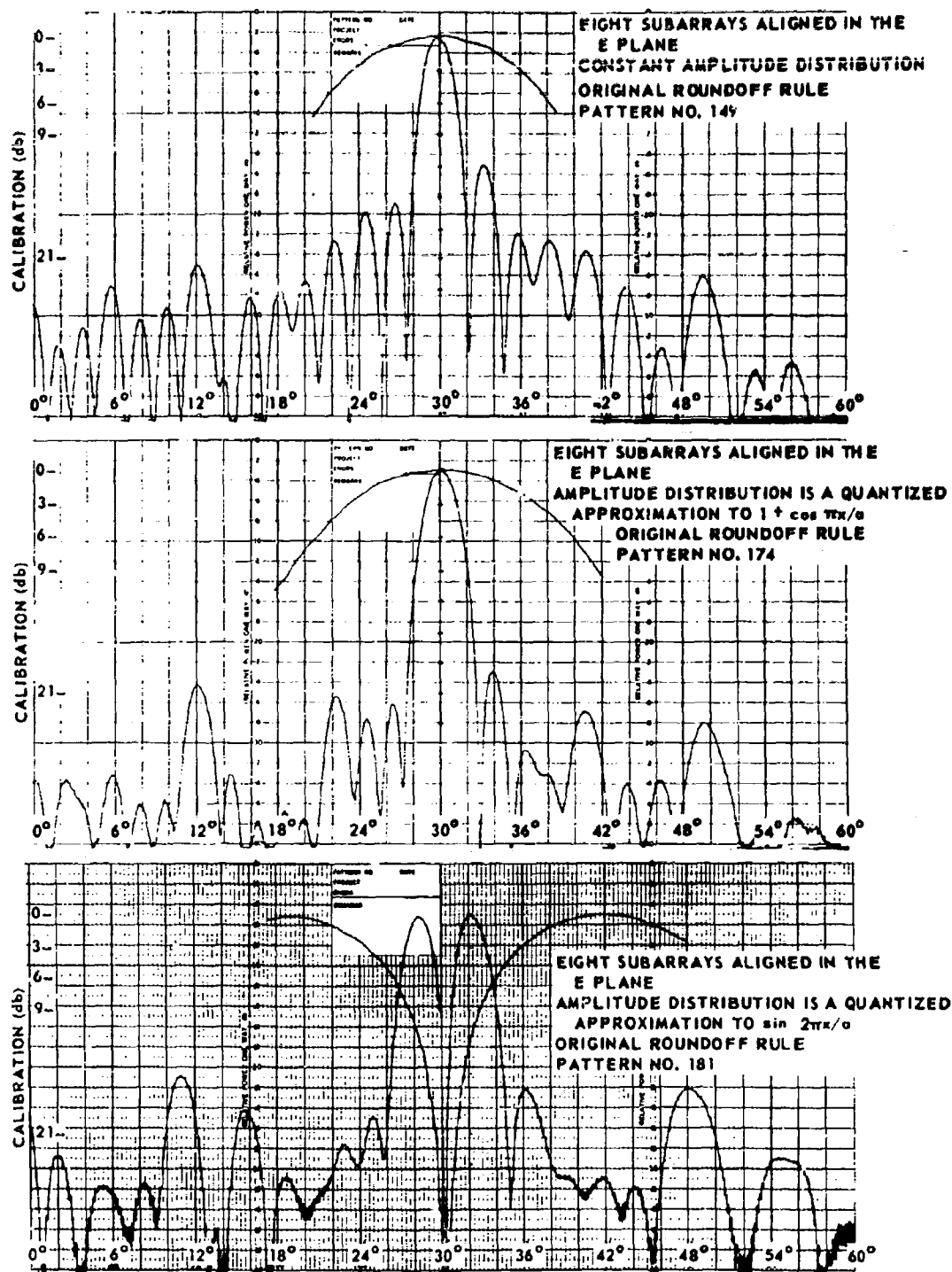


Fig. 3-36 30° Beam E Plane Patterns at 5.65 Gc

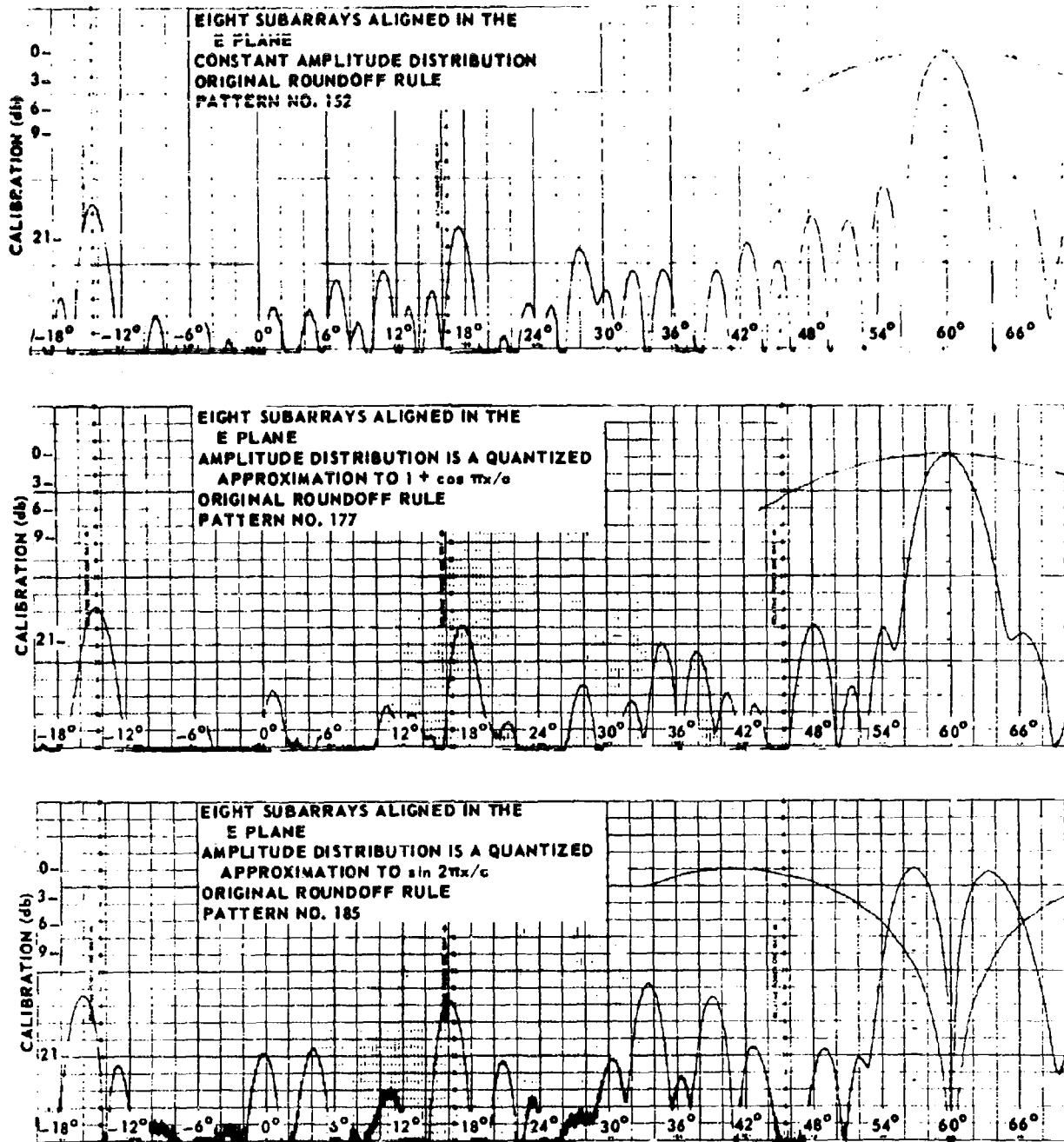


Fig. 3-37 60° Beam E Plane Patterns at 5.65 Gc

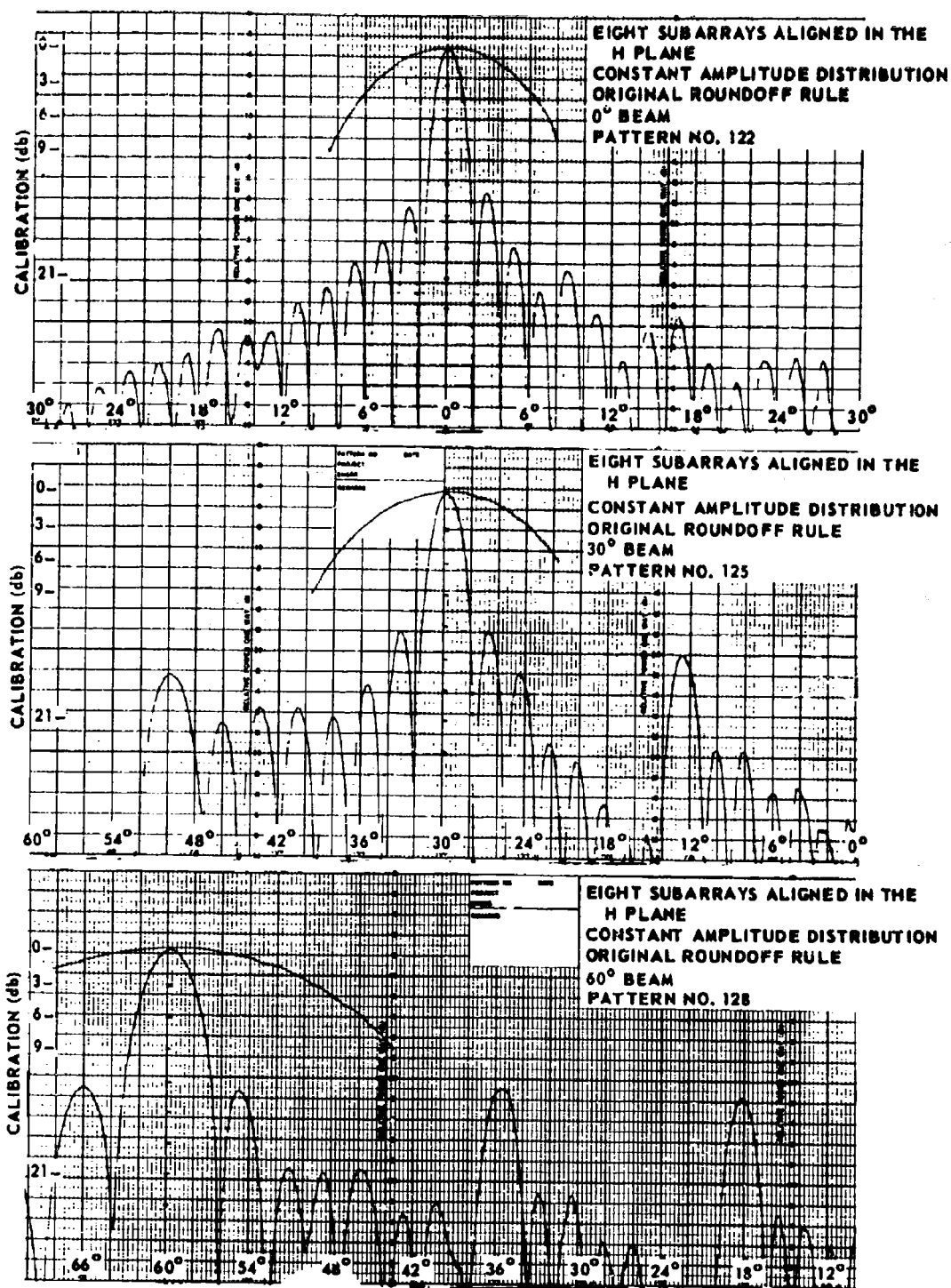


Fig. 3-38 0°, 30°, and 60° Beam H Plane Patterns at 5.40 Gc

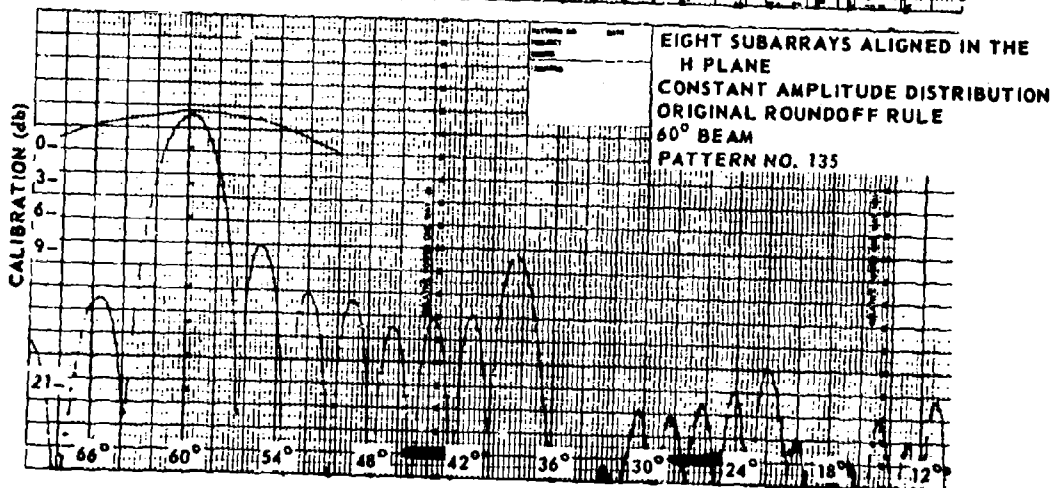
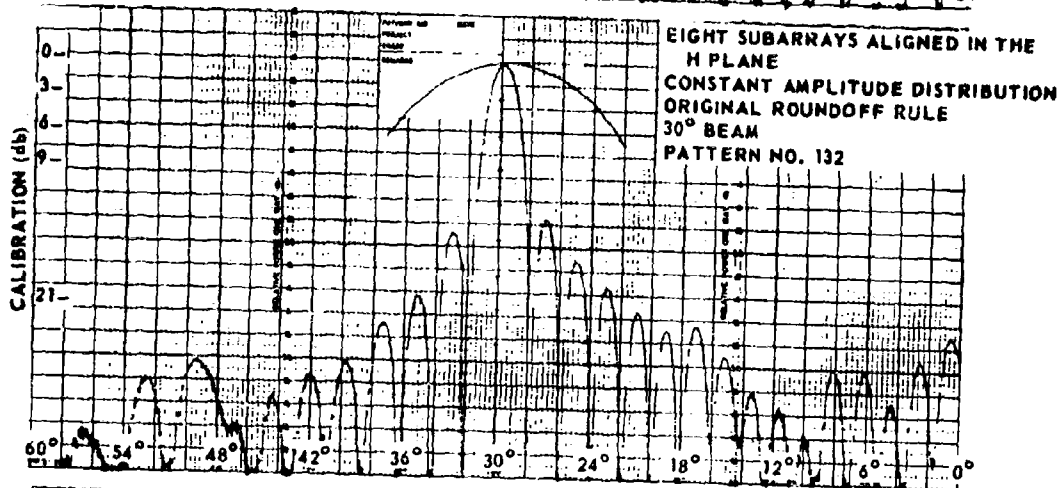
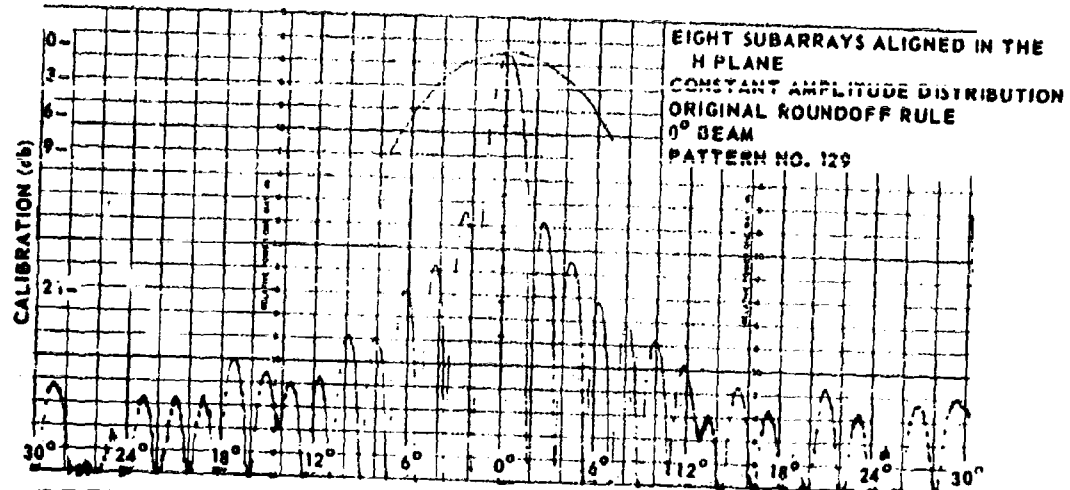


Fig. 3-39 0°, 30°, and 60° Beam H Plane Patterns at 5.90 Gc

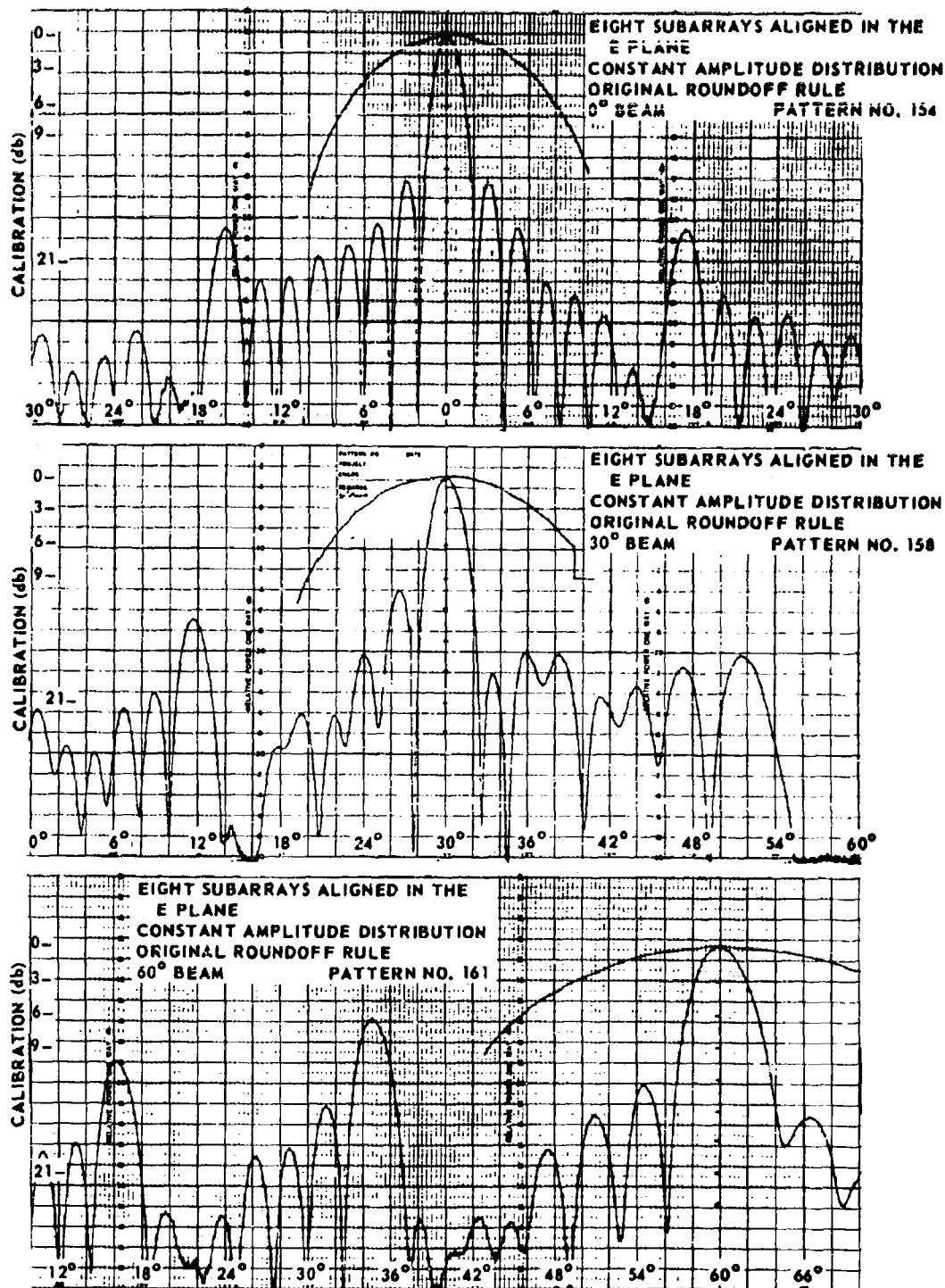


Fig. 3-40 0°, 30°, and 60° Beam E Plane Patterns at 5.40 Gc

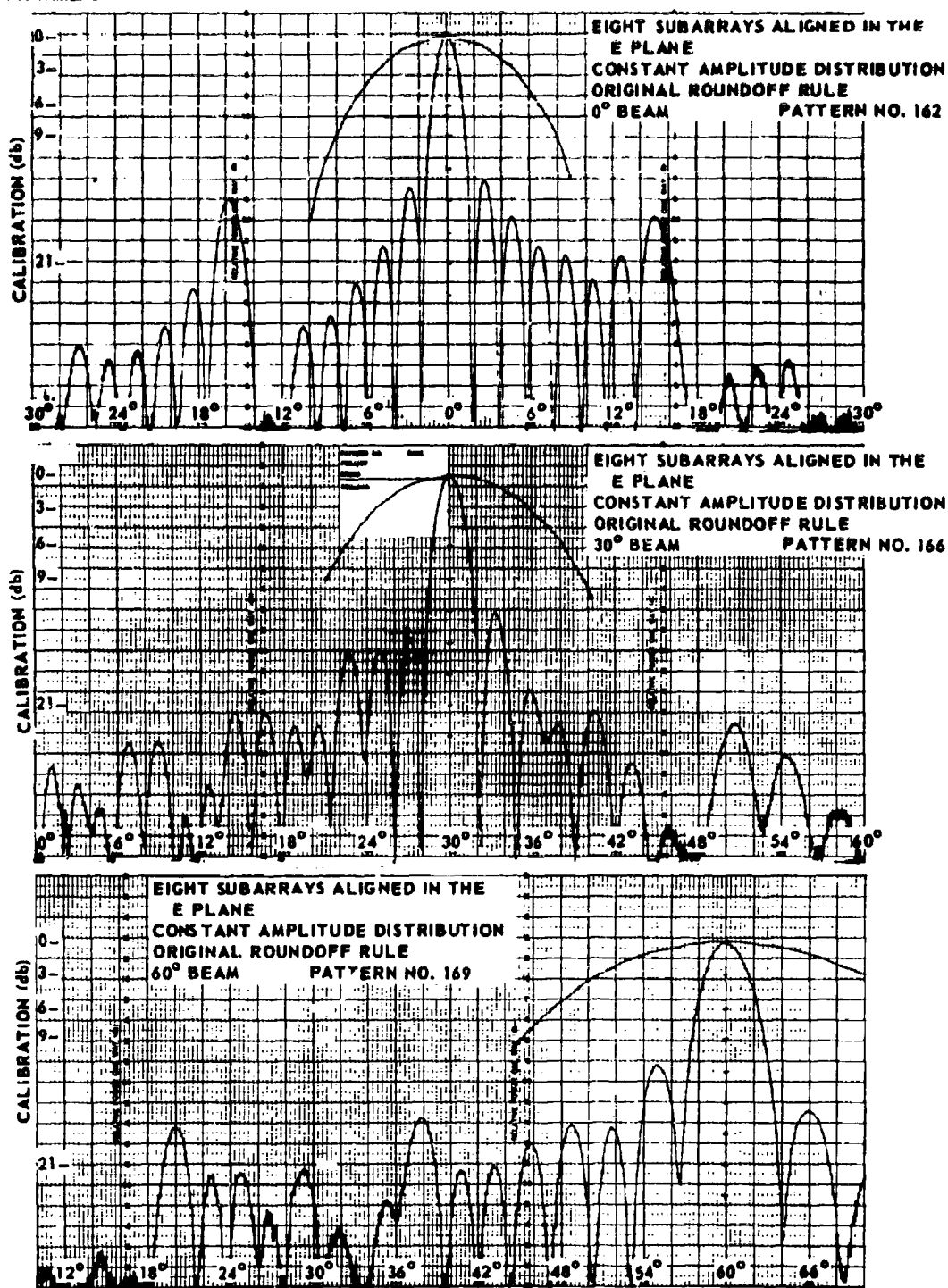


Fig. 3-41 0°, 30°, and 60° Beam E Plane Patterns at 5.90 Gc

Section 4

CONCLUSIONS AND RECOMMENDATIONS

A lightweight, inexpensive phased array antenna was constructed during a 6-month period. All components were fabricated at the Laboratory by previously untrained personnel who required only a few weeks time to acquire the necessary skills. Extensive measurements on the array indicate a high level of performance. In particular, the overall efficiency of the array at boresight was better than 70%, the maximum VSWR over a 10% band of frequencies was 2.6 at 60° scan, and the absolute rms beam steering accuracy was 1/100 beamwidth. Several array geometries were investigated and in each case, the array performance was closely related to the performance of a single subarray. It appears that a subarray of the type used here could be used to provide almost any array geometry and illumination. Throughout the measurements, attention was focused on the possibility of anomalous effects caused by mutual coupling and surface waves. None of these effects were observed.

Although the most important performance criteria were tested extensively several areas of investigation remain. In particular, it is of interest to examine:

1. Effects of gaps between subarrays on both mutual coupling and quantization lobes.
2. Effects of mutual coupling in more detail.
3. Effects of different quantization rules on the level of the quantization lobes.

4. Effects of high power and temperature on the performance of a subarray.
5. Methods for further improving the match on scanning.

There are, of course, a number of areas relating to an array of subarrays which still require development. For example, there has been almost no experimental effort to provide optimal sum and difference power combining networks. These power combining networks, together with suitable time delay devices, afford the potential capability of wide instantaneous bandwidths for a scanning array. Monitoring systems which would ensure proper operation of the antenna have also received inadequate attention.

In addition to further studies on an array of subarrays, several of the individual subarray components warrant improvement. For example, the phase shifter could be improved by replacing the pyrex matching sections with less fragile material and by strengthening the phase shifter flanges. The E plane horn could be improved by increasing the width and removing the lens. The horn would then have smaller amplitude ripples and reduced periodicities in the E plane. Removal of the lens would incur the loss of the diametric wiring capability and result in an improvement in subarray steering accuracy at the cost of increased complexity to both the computer and the array wiring. In this area, as in others, the component and system design are closely related and the particular system requirements would dictate the appropriate course of action.

Appendix A

Subarray Bandwidth Considerations

(T. C. Cheston)

The size of the subarray determines the bandwidth. Referring to Fig. A-1, an aperture 'a' generates a beam which is scanned in the direction θ_0 .

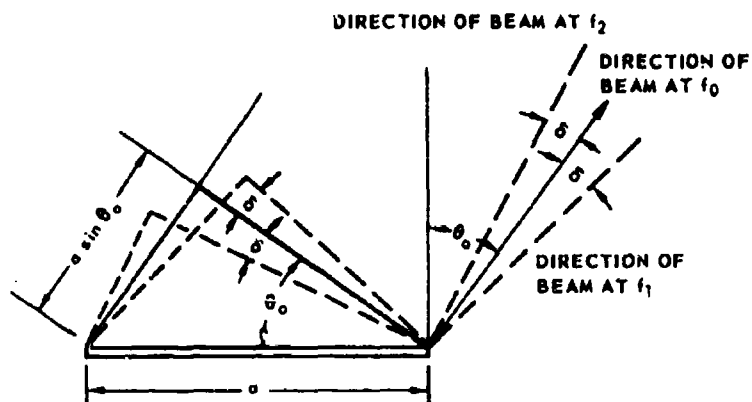


Figure A-1

The beam steering is obtained by frequency independent phase shift. The required phase shift at the edge of the aperture is

$$\varphi_0 = \frac{2\pi}{\lambda_0} a \sin \theta_0 \quad (1)$$

at frequency f_0 , wavelength λ_0 . At frequency f_1 , wavelength λ_1 ,

$$\varphi_0 = \frac{2\pi}{\lambda_1} a \sin(\theta_0 + \delta)$$

where δ = change in beam pointing direction.

$$\text{Therefore } \frac{2\pi}{\lambda_0} a \sin \theta_0 = \frac{2\pi}{\lambda_1} a \sin(\theta_0 + \delta)$$

and if δ is small then

$$\begin{aligned} \delta &= \pm \frac{1}{2} \frac{f_1 - f_2}{f_0} \tan \theta_0 \quad \text{radians} \\ &= \pm 23 \frac{f_1 - f_2}{f_0} \tan \theta_0 \quad \text{degrees} \end{aligned} \quad (2)$$

where $\frac{f_1 - f_2}{f_0}$ is the fractional bandwidth. The subarray beam is thus tilted by an amount that is a function only of bandwidth and scan angle and independent of subarray aperture size. With a maximum scan angle of 60° ,

$$\delta \approx \pm 50 \frac{f_1 - f_2}{f_0} \text{ degrees.}$$

With 10% bandwidth, for example, as well as with 60° of scan

$$\delta \approx \pm 5 \text{ degrees.}$$

If only phase shifters are used to steer the beam, then the beam will tilt with frequency as determined by Eq. (2). The bandwidth is increased if the aperture is divided into subarray apertures where the radiation of each subarray is steered by phase shifters but where the input to the subarrays is steered by time-delay. The antenna radiation pattern is then the product of the array factor multiplied by the element (i. e., subarray) factor. Figure A-2a shows these factors at the design frequency.

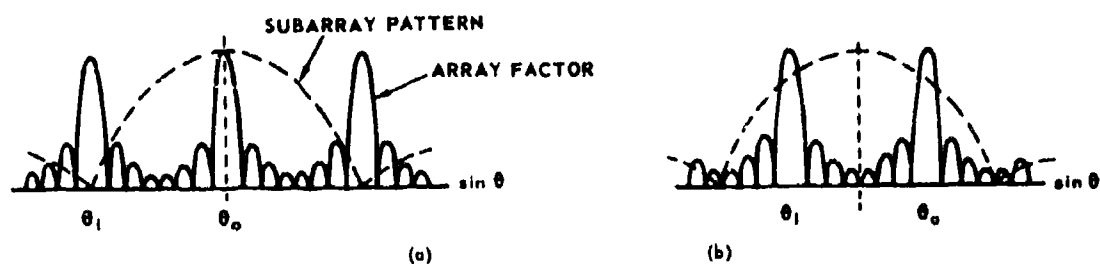


Figure A-2

As the frequency is changed, the pattern of the sub-array is tilted relative to the array factor according to Eq. (2). Figure A-2b shows that if this beam tilt is half the angular spacing of the grating lobe, then grating lobe and main beam are of equal size.

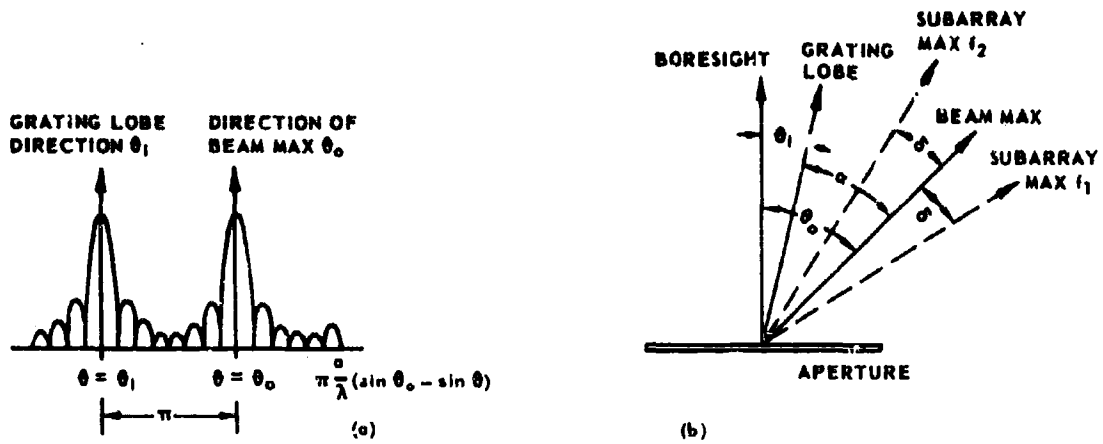


Figure A-3

Referring to Fig. A-3, the grating lobe occurs at an angle

$$\alpha = \theta_0 - \theta_1 \text{ away from the beam maximum where}$$

$$\pi \frac{a}{\lambda} (\sin \theta_0 - \sin \theta_1) = \pi$$

$$\text{hence } \frac{1}{a/\lambda} = \sin \theta_0 - \sin \theta_1$$

$$= \sin \theta_0 - \sin (\theta_0 - \alpha)$$

when α is small, this gives approximately

$$\alpha = \frac{1}{a/\lambda \cos \theta} \quad (3)$$

To avoid grating lobes and loss in forward gain, the beam tilt (δ) due to changes in frequency should be appreciably smaller than $\alpha/2$, half the grating lobe spacing. The amplitude of the grating lobe and the loss in forward gain is just a function of the ratio

$$p = \frac{\delta}{\alpha/2} \quad (4)$$

and can be determined for constant amplitude distribution apertures from $\frac{\sin x}{x}$ tables and is shown in Fig. A-4.

From Eqs. (2), (3), and (4)

$$a/\lambda = \frac{p}{\frac{f_1 - f_2}{f_0} \sin \theta_m} \quad (5)$$

where

θ_m = maximum scan angle

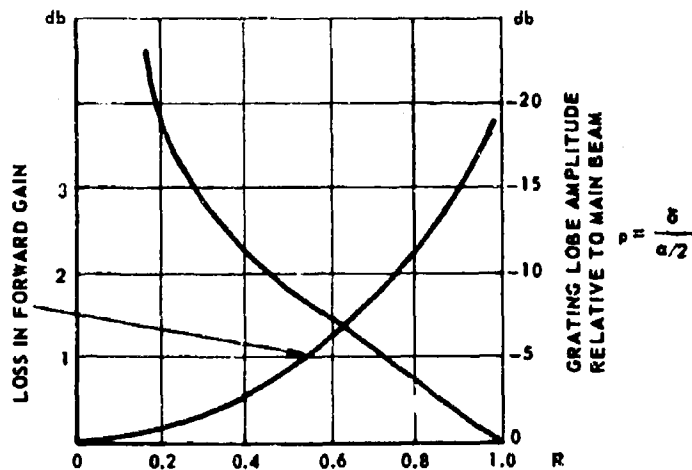


Figure A-4

Equation (5) and Fig. A-4 give the aperture size permissible for criteria involving maximal grating lobes at the maximum scan angle at the edge of the band. A value of $p = 0.5$ is perhaps permissible, remembering that this grating lobe appears in only one place, and under extreme scan and bandwidth conditions. When $p = 0.5$ then, from Fig. A-4, the worst grating lobe is about -9.5db, the greatest loss in forward gain is about 0.9db and

$$a/\lambda \geq \frac{1}{\frac{f_1 - f_2}{f_0} \sin \theta_m} \quad (6)$$

since $a/\lambda = \frac{50}{\theta_{BW}}$

where θ_{BW} = boresight beamwidth in degrees, Eq. (6) with θ_m large, may be written as

$$\text{Percent bandwidth} = \text{beamwidth (in degrees)}. \quad (7)$$

Appendix B
Quantization Lobe Analysis
(J. H. Kuck)

The following discussion presents a method of analyzing the quantization lobes which occur upon steering an array of subarrays with quantized phase commands.

For this analysis, it will be assumed that the quantization lobes appear at the maxima of the array factor, and the finite width of the array factor grating lobes will not be taken into account.

The antenna pattern is the product of the subarray pattern and an array factor which, under ideal conditions, has maxima at the nulls of the subarray pattern. Quantization lobes will occur if the subarray nulls are either poor or noncoincident with the maxima of the array factor. Consider the pattern of a linear subarray of N elements. The normalized signal received at a distant point in space from the n th element which has a small phase error, may be approximated by the sum of an ideal voltage vector and a quadrature error vector.

$$e_n \approx (1 + ja_n)e^{j\phi_n} \quad (1)$$

where ϕ_n is the phase of the received signal relative to the signal that would be received from an element at the center of the subarray and a_n is the phase error of that element in radians.

The signal is normalized in that the voltage is unity, assuming that the phase error is very small. e_n represents the relative amplitude

and phase of an rf signal $e^{j\omega t}$. For simplicity, this term is omitted, since it will be unaffected by the following manipulations.

For a uniformly illuminated linear array having an even number of elements the normalized signal can be written

$$e_s = \frac{1}{N} \sum_{-N/2}^{N/2} (1 + ja_n) e^{j\phi_n} \quad (2)$$

where N is the total number of elements. (In this and subsequent summations, it is to be understood that the $n=0$ term is omitted.) In other words:

$$e_s = \frac{1}{N} \sum_{-N/2}^{N/2} e^{j\phi_n} + j \frac{1}{N} \sum_{-N/2}^{N/2} a_n e^{j\phi_n} \quad (\text{omitting } n=0) \quad (3)$$

The first summation represents the ideal pattern of a subarray having no phase errors and the second summation is a superimposed error pattern.

Since an even number of radiating elements is assumed

$$\phi_n = \frac{n}{|n|} (2|n| - 1)\phi \quad (4)$$

where ϕ is the desired phase-slope, expressed as the phase of element $n = 1$, the nearest element to the center of the subarray in the positive direction. If α is the desired beam-pointing angle off boresight, then $\phi = (2\pi x/\lambda)\sin \alpha$, where x is the distance of the first element from the center of the array and λ is the r. f. wavelength.

For the pattern of an ideal subarray, the first summation in Eq. (3) may be expressed in the well-known form:

Ideal subarray pattern

$$A = \frac{\sin N\phi}{N \sin \phi} \quad (5)$$

The subarray error pattern, designed S, is the second summation in Eq. (3):

subarray error pattern

$$S = \frac{1}{N} \sum_{n=-N/2}^{N/2} a_n e^{j(2|n|-1)\phi} \quad (6)$$

Assuming a linear array of subarrays the array factor by which the subarray pattern is multiplied, when the total antenna pattern of the array is required, is:

array factor

$$G = \frac{\sin M N \phi}{M \sin N \phi} \quad (7)$$

where M is the number of subarrays in the array.

Grating Lobes

Grating lobes (due to a phase error that is repetitive from subarray to subarray) will occur at those points in the pattern, where $\sin N\phi = 0$ or, in other words, at:

$$\phi = p\pi / N \quad (8)$$

where p is an integer.

These are the points at which the major maxima occur in the array factor, Eq. (7), and nulls occur in the ideal subarray pattern, Eq. (5).

(If $\phi = \pi$, there would be a maximum instead of a null in the ideal subarray pattern, but with the usual half-wavelengths element spacing ϕ cannot exceed $\pi/2$.)

At those maxima where grating lobes can occur, the array factor has the value, 1, and the ideal subarray pattern is zero. Therefore, the amplitude of the grating lobe at this point is simply the value of the error pattern, Eq. (6), multiplied by 1. Relative to the signal on boresight, the grating lobe amplitude is the amplitude of g , where:

$$g = j \frac{1}{N} \sum_{-N/2}^{N/2} a_n e^{j \frac{n}{|n|} (2|n| - 1) \phi_0} \quad (9)$$

where ϕ_0 is the value of ϕ at that null. (The possibility should be recognized that the grating lobe maximum could occur slightly off the ϕ_0 point and the amplitude may, therefore, be slightly greater than the value given by Eq. (9). However, Eq. (9) is a useful lower limit and is not expected to be very much less than the true maximum.) Equation (9) will be evaluated for a few simple bad-error cases that might occur due to a computer fault or roundoff errors in an array composed of four-bit digital phase shifters controlled by a computer. A linear array of eight subarrays, each subarray having eight elements, will be assumed.

Case I: 22½° Error in One of the Eight Phase-Command to All Subarrays

(e.g. due to an open output line from computer):

$$\begin{aligned} a_n &= \pi/8 \\ g &= \frac{a_n}{8} = \pi/64 \\ &= -26 \text{ db} \end{aligned}$$

Case II: "Phase Split" (Worst-Case Roundoff Error with "Diagonal Opposite" Wiring):

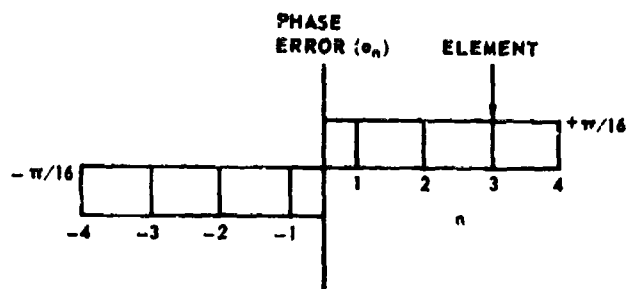


Figure B-1

Figure B-1 indicates how the roundoff errors from the desired phase front are distributed over the eight elements in each subarray. (The actual roundoff errors from the computed values will be zero in the right half of the subarray and minus $22\frac{1}{2}^\circ$ ($\pi/8$ radians) in right, but any arbitrary phase plane may be used as a reference, so the one has been chosen which gives symmetry.)

Equation (9) may be written for an eight-element subarray as:

$$g = j \frac{1}{8} \sum_{n=1}^4 a_n e^{j(2n-1)\varphi_0} + j \frac{1}{8} \sum_{n=1}^4 a_{-n} e^{-j(2n-1)\varphi_0} \quad (10)$$

where φ_0 is the value of φ at a null. This expression is a summation of sine terms:

$$g = \frac{2}{N} \sum_{n=1}^4 a_n \sin (2n-1)\varphi_0 \quad (11)$$

At the first null (i. e., at $p = 1$ in Eq. 9):

$$\phi_0 = \pi/8$$

$$|g| = \frac{a_n}{4} (\sin \pi/8 + \sin 3\pi/8 + \sin 5\pi/8 + \sin 7\pi/8) \quad (12)$$

$$a_n = \pi/16$$

$$|g| = \frac{2.6\pi}{64} = 17.9 \text{ db (grating lobe at first subarray null)}$$

It is expected that with this type of error, the grating lobes farther out will be of lower amplitude, because of the larger phase difference between the terms in Eq. (12).

Case III: Linear Phase-Error Curve from 0 to $22\frac{1}{2}^\circ$:

This is a type of roundoff error that could occur with a certain type of beam-steering and computation, i. e., if the phase-plane is rotated about one edge of the subarray and the phase-command for each phase-shifter is the next lower four-digit binary number below the accurately computed value.

(It is thought that there may be a more desirable roundoff rule that would result in smaller grating lobes. However, considerable investigation may be required to settle this point conclusively.)

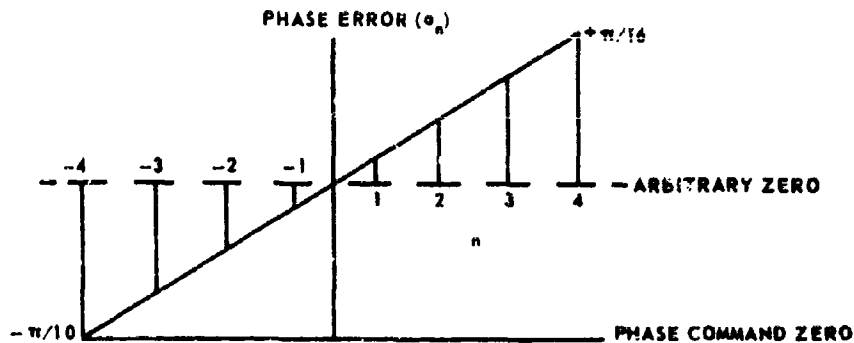


Figure B-2

As indicated by Fig. B-2, the assumed error is a linear function of n with a maximum value of plus or minus $\pi/16$. Equation (11) still applies. Substitution of the appropriate values of the a_n 's gives:

$$|g| = \frac{a_m}{4} \left(\frac{1}{7} \sin \varphi_o + \frac{3}{7} \sin 3\varphi_o + \frac{5}{7} \sin 5\varphi_o + \sin 7\varphi_o \right)$$

where a_m , the maximum error, is $\pi/16$.

At the first subarray null, where $\varphi_o = \pi/8$, this gives:

$$|g| = -22.8 \text{ db}$$

Case IV: Linear Phase-Slope, Two-Cycle Sawtooth: (Phase-plane Rotated about one Edge of the Subarray)

The phase errors relative to the computer command look like Fig. B-3.

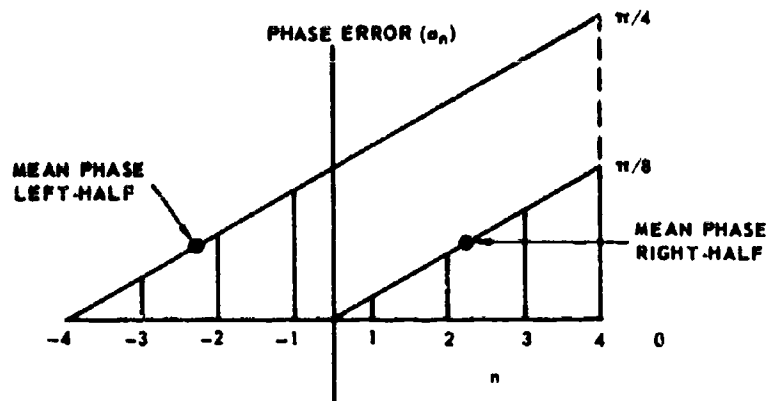


Figure B-3

Since it appears that one cannot choose any arbitrary phase reference that will be a center of symmetry for both halves of the array and, thereby, significantly reduce the amount of computation, the zero-reference has not been shifted, and Eq. (10) is evaluated by brute force, as follows:

$$a_1 = \frac{1}{7} \times \frac{\pi}{8} = .0567$$

$$a_2 = \frac{3}{7} \times \frac{\pi}{8} = .170$$

$$a_3 = \frac{5}{7} \times \frac{\pi}{8} = .284$$

$$a_4 = \frac{\pi}{8} = .397$$

$$a_{-1} = \frac{6}{7} \times \frac{\pi}{8} = .340$$

$$a_{-2} = \frac{4}{7} \times \frac{\pi}{8} = .227$$

$$a_{-3} = \frac{2}{7} \times \frac{\pi}{8} = .113$$

$$a_{-4} = 0 \quad 0$$

Equation (9) yields the following summations:

$$g = j/N \sum_{n=1}^4 \{a_n \cos(2n-1)\varphi_0 + j a_n \sin(2n-1)\varphi_0\}$$

$$+ j/N \sum_{n=1}^4 \{a_{-n} \cos(2n-1)\varphi_0 - j a_{-n} \sin(2n-1)\varphi_0\}$$

Substitution of the a_n 's and a_{-n} 's and $\varphi_0 = \pi/8$ (i. e., solving for the first null) gives:

<u>n</u>	<u>(a_n + a_{-n})</u>	<u>cos(2n - 1)φ₀</u>	<u>(a_n + a_{-n}) cos(2n - 1)φ₀</u>
1	.397	.924	.367
2	.397	.383	.152
3	.397	-.383	-.152
4	.397	-.924	-.367
Re j{Σ _n + Σ _{-n} } = 0			Total 0

<u>n</u>	<u>(a_n + a_{-n})</u>	<u>sin(2n - 1)φ₀</u>	<u>(a_n + a_{-n}) sin(2n - 1)φ₀</u>
1	-.283	.383	-.108
2	-.057	.924	-.053
3	.171	.924	.158
4	.397	.383	.152
			Total .149

THE JOHNS HOPKINS UNIVERSITY
APPLIED PHYSICS LABORATORY
SILVER SPRING, MARYLAND

$$I_m j \{ \Sigma_n + \Sigma_{-n} \} = 0.149$$

$$g = 1/8 \sqrt{(Re)^2 + (I_m)^2} = .0186$$

$$= -20 \log_{10} 53.7$$

$$= -35.6 \text{ db}$$

The above illustrate the amount of computation that would be required to obtain the amplitude of one grating lobe in the general case for an arbitrary distribution of phase errors.

REFERENCES

1. T. C. Cheston and H. M. Grady, "A Phased Array Using Sub-array Techniques," Proc. of IEEE Symposium on Antennas and Propagation, 1965, pp. 98-101.
2. L. W. Lechtrek, "Cumulative Coupling in Antenna Arrays," Proc. of IEEE Symposium on Antennas and Propagation, 1965, pp. 144-149.
3. P. W. Hannan, P. J. Meier, and M. A. Balfour, "Simulation of Phased Array Antenna Impedance in Waveguide," IEEE Trans. on Antennas and Propagation, Vol. AP-11, No. 6, November 1963, pp. 715-716.
4. E. G. Magill and H. A. Wheeler, "Wide Angle Impedance Matching of a Planar Array Antenna by a Dielectric Sheet," Proc. of IEEE Symposium on Antennas and Propagation, 1965, pp. 164-169.
5. H. M. Grady, "Evaluation of a Lightweight Horn and Lens Assembly," APL/JHU Internal Tech Note MRT-4-009, 15 December 1965.
6. J. Frank, C. A. Shipley, J. H. Kuck, "Latching Ferrite Phase Shifter for Phased Arrays," Microwave Journal, March 1967.
7. C. A. Shipley, "Phase Shifter Assembly Procedure," APL/JHU Internal Tech Note MRT-4-028, 18 July 1966.
8. J. H. Kuck, "Monitoring Circuits for the Phase Shifter Drivers in the Phased Array Antenna," APL/JHU Internal Memorandum MRT-4-050, 11 November 1966.
9. J. H. Kuck, "Record of Driver Circuit, Mod. 28B, for Use with the Eight-Subarray Antenna," APL/JHU Internal Memorandum MRT-4-032, 22 August 1966.

THE JOHNS HOPKINS UNIVERSITY
APPLIED PHYSICS LABORATORY
SILVER SPRING MARYLAND

10. L. E. Briscoe, "Wiring Techniques for the Forty-Eight Element Subarray in the Eight-Subarray Antenna," APL/JHU Internal Memorandum MRT-4-031, 12 July 1966.
11. P. W. Hannan, "The Element-Gain Paradox for a Phased Array Antenna," Trans. PTGAG, July 1964, pp. 423-433.
12. R. C. Hansen, "Microwave Scanning Antennas." Vol. II, 1966.
13. P. W. Hannan, D. S. Lerner, G. H. Knittel, "Impedance Matching a Phased Array Antenna over Wide Scan Angles by Connecting Circuits," IEEE PTAP, AP-13, January 1965, pp. 28-34.
14. J. L. Allen, "Phased Array Radar Studies," 1960-61, Lincoln Laboratories Technical Report No. 236.
15. L. A. Rondinelli, "Effects of Random Errors on the Performance of Antenna Arrays of Many Elements," 1959, IRE National Convention Rec., Part I, pp. 174-189.

UNCLASSIFIED
Security Classification

DOCUMENT CONTROL DATA - R&D		
<i>(Security classification of title, body of abstract and indexing annotation must be entered when the overall report is classified)</i>		
1. ORIGINATING ACTIVITY (Corporate author) The Johns Hopkins University, Applied Physics Lab 8621 Georgia Avenue Silver Spring, Maryland		2a. REPORT SECURITY CLASSIFICATION Unclassified
3. REPORT TITLE Phased Array Antenna Development		2b. GROUP
4. DESCRIPTIVE NOTES (Type of report and inclusive dates)		
5. AUTHOR(S) (Last name, first name, initial) Frank, J.		
6. REPORT DATE March 1967	7a. TOTAL NO. OF PAGES 164	7b. NO. OF REFS 15
8a. CONTRACT OR GRANT NO. NOw 62-0604-c	8a. ORIGINATOR'S REPORT NUMBER(S) TG-882	
b. PROJECT NO. Task Q08	8b. OTHER REPORT NO(S) (Any other numbers that may be assigned this report)	
c.		
10. AVAILABILITY/LIMITATION NOTICES Distribution of this document is unlimited.		
11. SUPPLEMENTARY NOTES	12. SPONSORING MILITARY ACTIVITY Advanced Research Projects Agency	
13. ABSTRACT The ability to rapidly scan a highly directive antenna beam has been made possible by recent advances in the art of microwave phase shifting. This report describes an experimental C-band phased array antenna developed at the Applied Physics Laboratory. The antenna is composed of eight subarrays which may be arranged in several configurations to investigate the effects of a full array. Each subarray contains a reactive power divider, 48 ferrite phase shifters and their electronic drivers, and a radiating structure. The radiating structure has been designed to provide some compensation for impedance variation with scanning. The design and fabrication of the components are discussed in detail, and test results of the array are presented and analyzed.		

DD FORM 1473
1 JAN 64

UNCLASSIFIED
Security Classification

UNCLASSIFIED
Security Classification

14.

KEY WORDS

Array Antenna

Phased Array Antenna

Antenna Array

Phase Shifter

Ferrite Phase Shifter

Latching Ferrite Phase Shifter

Power Divider

Reactive Power Divider

Parallel Feed

Subarray

Array of Subarrays

UNCLASSIFIED
Security Classification